

MEASUREMENT OF HADRONICALLY
PRODUCED 3P_0 -STATE CHARMONIUM AT
 $\sqrt{S} = 23.7$ GeV

by

Richard J. Tesarek

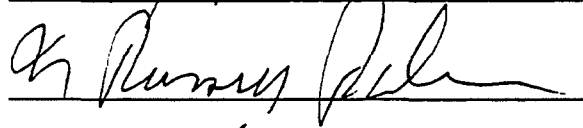
Department of Physics
Duke University

Date: 3/25/93

Approved:


Lloyd R. Fortney, Supervisor





Daniel Hawthorn

Dissertation submitted in partial fulfillment of
the requirements for the degree of Doctor
of Philosophy in the Department of
Physics in the Graduate School
of Duke University

1993

FERMILAB
LIBRARY

ABSTRACT

(Elementary Particle Physics)

MEASUREMENT OF HADRONICALLY
PRODUCED 3P -STATE CHARMONIUM AT
 $\sqrt{S} = 23.7$ GeV

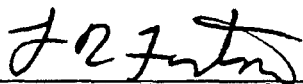
by

Richard J. Tesarek

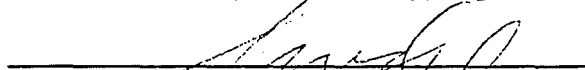
Department of Physics
Duke University

Date: 3/25/93

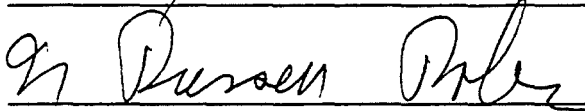
Approved:



Lloyd R. Fortney, Supervisor









An abstract of a dissertation submitted in partial
fulfillment of the requirements for the degree
of Doctor of Philosophy in the Department of
Physics in the Graduate School of
Duke University

1993

Abstract

Fermilab experiment E705 measured the inclusive production ratio for the two higher mass 1^3P_1 charmonium states, $\sigma_{\chi_1}/\sigma_{\chi_2}$, for 300 GeV/c proton and π^\pm beams interacting with a lithium target. Our measured ratios of $0.08^{+0.25}_{-0.15}$ and $0.52^{+0.52}_{-0.28}$ for proton and pion induced reactions, respectively, show good agreement with previous experiments. The production ratio for proton data is consistent with a gluon fusion model for p-wave charmonium, while the pion ratio could be represented by a strict color evaporation model or an admixture of different mechanisms.

Total production cross sections were measured for the individual chi states using both beam types. Differential cross sections in transverse momentum and Feynman x were also measured for the combined $\chi_1 + \chi_2$ signal. The differential cross sections are qualitatively similar to those for the J/psi and show a transverse momentum dependence of $e^{\alpha p_T}$ with a sharper fall off for proton beam, $\alpha = -1.47 \pm 0.25$ (GeV/c) $^{-1}$, compared with that for pion beams, $\alpha = -1.39 \pm 0.14$ (GeV/c) $^{-1}$.

Angular distributions of the decay photon and positive muon were also measured for reactions induced by all beam types but are consistent with the predictions of all production mechanism hypotheses.

Acknowledgements

There were many people who helped either directly or indirectly and deserve some credit for the preparation of this dissertation. First and foremost my gratitude is extended to my advisor and mentor, Lloyd Fortney. He was always available with an intuitive explanation whenever I had a question. He was also instrumental in keeping this work to a single volume.

There are also the many people who shared the “E705 challenge” and helped to make the experiment an unforgettable experience and keeping a perspective amid the chaos of alarms, exploding targets and heated group meetings. Steve Delchamps, Ting Yang Chen, and Marzia Rosati helped me in various aspects of the analysis and provided a testbed for some of my ideas. The other members of the Duke contingent, Shen Qifeng and Tim Turkington are included here for thier contributions to the analysis code.

Much of my mental stability I owe to my fellow graduate students and the faculty and staff in the high energy physics group: Tom Carter, Jay Cook, Susi Hauger, Dan Hennessy, Alfred Lee, Cal Loomis, Grace Mendez, Chiho Wang and Malie Yin. Pat Hoyt deserves special recognition for taking care of my daily business here at Duke when I was stationed at Fermilab.

ACKNOWLEDGEMENTS

iii

I would also like to thank the late night crowd in the physics department, Jochen Rau and Roxanne Springer, for the many stimulating discussions and sharing tea with me at 1:00 AM when I was trying to finish this work.

Last but not least, I include the people who kept me sane during my tenure as a graduate student, Mary Russell, Dan and Carla Suson, Sheryl Libman and Joe Simpkins. Their patience, insight and support have allowed me to continue in the face of much of the adversity I encountered over the past several years. I include my mother, Marie Tesarek, in this list although she has had to put up with me considerably longer and therefore, really belongs in a class by herself.

Contents

Abstract	i
Acknowledgements	ii
List of Figures	vii
List of Tables	ix
1 Introduction	1
1.1 Quantum Chromodynamics (QCD)	3
1.2 Charmonium System	6
1.3 Previous Experiments	9
2 Experiment Apparatus	16
2.1 Accelerator	16
2.2 Beam/Beam Line	17
2.2.1 Beam Stations	21
2.2.2 Čerenkov Counters	22
2.3 Spectrometer	22
2.3.1 Target	24
2.3.2 Proportional Chambers (PCs and PCBs)	26
2.3.3 Drift Chambers	27
2.3.4 Analysis Magnet (Rosie)	28
2.3.5 Electromagnetic Calorimeter	28
2.3.6 Scintillation Hodoscopes	37
2.4 Triggers	42
2.4.1 Minimum Bias (CF Strobe)	45
2.4.2 Photon Triggers	46
2.4.3 Dimuon	46
2.4.4 Two-Vee	48
2.4.5 LED	49
2.5 Data Acquisition and Control	49

3	Calibration and Monitoring	53
3.1	Beam Line	53
3.1.1	Cerenkov Counters	54
3.1.2	Beam Chambers	54
3.2	Magnetic Spectrometer	56
3.2.1	Analysis Magnet (Rosie)	57
3.2.2	Drift and Proportional Chambers	57
4	Event Reconstruction	77
4.1	Track Reconstruction	77
4.1.1	Beam Tracking	78
4.1.2	Upstream Tracking	78
4.1.3	Interaction Vertex Determination	80
4.1.4	Downstream Tracking	81
4.1.5	Momentum Determination	82
4.1.6	Momentum Resolution and Efficiency	84
4.2	Electromagnetic Reconstruction	85
4.2.1	Device Decoding	87
4.2.2	Pattern Recognition	89
4.2.3	Shower Fitting	91
4.2.4	Position Determination	102
4.2.5	Active Plane Energy	105
4.2.6	Cluster/Shower Removal	108
4.2.7	Energy Corrections	109
4.3	Particle Identification	110
4.3.1	Hadron Rejection	111
4.3.2	Electron/Positron Reconstruction	114
4.3.3	Pizero Reconstruction	127
5	Analysis	130
5.1	Data Reduction	130
5.1.1	Dimuon Filtering (Pass I)	130
5.1.2	J/psi Reconstruction (Pass II)	132
5.2	Electromagnetic Showers	134
5.3	J/psi-Photon Mass Spectrum	139
5.3.1	Backgrounds	143
5.3.2	Incoherent Background (Cross Paired Events)	146
5.3.3	Coherent Backgrounds	147
6	Results and Conclusions	157
6.1	Chi Monte Carlo	157
6.1.1	Photon Acceptance and Reconstruction Efficiency	160
6.1.2	Chi Resolution Functions	162
6.2	Fitting for the Chi Signals	166
6.2.1	Fit Procedure	166
6.2.2	N_{x_1} , N_{x_2} Parameterization of the Chi Signal	168

6 Results and Conclusions	157
6.1 Chi Monte Carlo	157
6.1.1 Photon Acceptance and Reconstruction Efficiency	160
6.1.2 Chi Resolution Functions	162
6.2 Fitting for the Chi Signals	166
6.2.1 Fit Procedure	166
6.2.2 N_{χ_1}, N_{χ_2} Parameterization of the Chi Signal	168
6.2.3 T, R_{12} Parameterization of the Chi Signal	171
6.3 Chi Cross Sections	174
6.3.1 Total Chi Cross Sections	174
6.3.2 Differential $\chi_1 + \chi_2$ Cross Sections	177
6.3.3 Angular Distributions	179
6.4 Summary and Conclusions	186
A Shower COMMON Block	187
B Deconvolution Method	193
C Mass versus Mass Difference Uncertainties	196
References	199
Biography	203

List of Figures

1.1	Generic hadron-hadron interaction	4
1.2	Charmonium level diagram	6
1.3	Lowest order Feynman diagrams for charmonium production	8
1.4	Definition of chi decay angles	9
1.5	Experiment layout for the Chicago Cyclotron Magnet facility.	11
1.6	$J/\psi\gamma$ invariant mass distribution for π^- Be reactions	11
1.7	J/ψ -photon invariant mass distribution	14
1.8	The WA11 spectrometer	15
1.9	$J/\psi e^+e^-$ invariant mass spectrum	15
2.1	Fermilab accelerators and beam lines	18
2.2	Schematic diagram of the E705 beam line	19
2.3	The E705 Spectrometer	23
2.4	E705 electromagnetic calorimeter	29
2.5	Cross section of a portion of the Lead Gas Calorimeter	31
2.6	Cross section of a portion of the Gas Tube Hodoscope	33
2.7	Schematic of the calorimeter, glass electronics	36
2.8	Muon detector and beam dump	40
2.9	MU1 paddle arrangement	41
2.10	Beam definition logic	44
2.11	Triple coincidence logic	47
2.12	Schematic diagram of the E705 data acquisition system	50
3.1	Čerenkov counter efficiencies	55
3.2	Calibration reconstructed energy distributions	65
3.3	Calorimeter energy resolution by region	67
3.4	Energy fraction from the dynamic pedestal and correlated width	70
3.5	Main Array glass position residuals	71
3.6	Hodoscopes position residuals	73
3.7	Timing for block 147	74
4.1	Electromagnetic reconstruction program flow diagram	86
4.2	Main Array block pattern definitions	90
4.3	Energy partition of a virtual large block	100
4.4	Comparison of 6.6 GeV, normal incident electrons and pions	112

4.5	E/p spectrum for track-electromagnetic shower matches . . .	113
4.6	Typical E/p spectra for various momentum ranges	115
4.7	September negative E/p momentum dependence by region . .	116
4.8	November positive E/p momentum dependence by region . .	117
4.9	January negative E/p momentum dependence by region . . .	118
4.10	January positive E/p momentum dependence by region . . .	119
4.11	Energy resolution compared between data and calibration . .	121
4.12	Position resolution comparison between data and calibration	123
4.13	Opposite sign track pair invariant mass (assuming electrons)	124
4.14	Electron reconstruction efficiency for the four detector regions	126
4.15	Photon-photon invariant mass	128
5.1	Opposite sign dimuon mass spectrum	132
5.2	E/p for J/psi candidates and photon triggers	136
5.3	Momentum distributions for J/psi candidate and photon trigger electrons	137
5.4	J/psi-electromagnetic shower mass difference, shower multiplicity and shower energy spectra	140
5.5	Photon cuts imposed on J/ ψ - γ mass spectrum	142
5.6	J/psi-photon mass difference, photon multiplicity and photon energy spectra	144
5.7	Background generated from cross-paired events	145
5.8	Fit to miss-paired background	147
5.9	Photon multiplicity, energy and $\psi\gamma$ mass difference spectra for $\psi' \rightarrow \psi\pi^0\pi^0$ decays.	152
5.10	Photon multiplicity, energy and $\psi\gamma$ mass difference spectra for $\psi' \rightarrow \psi\eta$ decays.	153
5.11	$\psi\gamma$ mass difference spectrum with overlaid backgrounds . . .	155
6.1	J/psi acceptance times reconstruction efficiency for pion and proton beams	159
6.2	Chi photon acceptance for pion and proton beams	161
6.3	Chi photon reconstruction efficiency for pion and proton beams	163
6.4	χ_1 and χ_2 resolution functions	164
6.5	Chi mass shift versus photon fractional change in the photon energy scale	165
6.6	Mass difference spectra for π^+ and π^- data	169
6.7	Mass difference spectra for π^\pm and proton data	170
6.8	R_{12} compared with other experiments for pion and proton beams	173
6.9	Raw chi transverse momentum distributions by beam type . .	175
6.10	Raw chi Feynman x distributions by beam type	176
6.11	Combined chi differential cross section $d\sigma/dp_T$ by beam type	180
6.12	Combined chi differential cross section $d\sigma/dx_F$ by beam type	181
6.13	Raw chi photon angular distributions by beam type	182
6.14	Raw chi positive muon angular distributions by beam type . .	183
6.15	Corrected angular distributions for chi photons by beam type	184

LIST OF FIGURES

6.16 Corrected angular distributions for the μ^+ from chi decay by beam type	185
B.1 Frequency filter effects for 30 GeV/c electrons in the GTH .	195

List of Tables

1.1	Elementary fermions and their properties	2
1.2	Predicted chi production ratios and angular distribution parameters	10
2.1	Beam Chamber Parameters	22
2.2	Proportional Chamber Parameters	25
2.3	Drift Chamber Parameters	27
2.4	Electromagnetic Calorimeter Glass Properties	34
2.5	Trigger Percentages and Prescale Values	43
3.1	Average beam chamber resolutions and efficiencies	56
3.2	Proportional and drift chamber efficiencies	59
3.3	Measured energy resolutions from calibration	66
3.4	Calibration resolution fit parameters by calorimeter region.	66
3.5	Time resolution of the Main Array glass	75
4.1	R_z upper limits for the z depth index in the EGS tables	94
4.2	Energy correction constants for negative beam.	110
4.3	Energy correction constants for positive beam.	110
4.4	Energy resolution parameters from tagged electrons	120
4.5	Position resolution from tagged electrons	122
5.1	Number of reconstructed J/psis and psiprimes by beam type	134
5.2	Means and widths of E/p in our dimuon sample and photon trigger samples	135
5.3	Kolmogorov comparisons of J/psi candidate and photon trigger samples of E/p	138
5.4	Psiprime cascade decays producing a J/psi and photons	149
6.1	J/psi kinematic distribution parameters	158
6.2	Chi fit results; χ_1, χ_2 parameterization	171
6.3	Chi fit results; T, R_{12} parameterization	172
6.4	E705 ratios of chi production cross sections by beam type	174
6.5	J/psi total, forward, inclusive cross sections	177
6.6	Chi forward, inclusive cross sections by beam type	177

LIST OF TABLES

xi

6.7	Fit parameters for chi p_T and x_F distributions	178
6.8	Angular distribution fit parameters by beam type	179

Chapter 1

Introduction

The currently accepted set of theories for the most fundamental description of matter, the Standard Model, relates the four known forces, the strong, weak, electromagnetic and gravitational, experienced by the constituent particles of matter through the exchange of other, gauge, particles. The fundamental constituents of all matter consist of fermions classified into two categories of point-like particles called leptons and quarks depending on which forces are experienced by them. Each category or class is further subdivided into three families or generations of particle pairs.

Every lepton family consists of an electrically charged, massive particle and an electrically neutral, massless partner called a neutrino. The three lepton families are named after their charged member, the electron, muon and tau, in order of increasing mass. All leptons experience the weak force, while charged leptons also experience the electromagnetic and gravitational forces. Quark families consist of pairs of electrically charged particles which are effected by all four forces. Each quark is denoted by a *flavor* quantum number given the somewhat whimsical names of up, down, charm, strange, top or truth (which has yet to be discovered), and bottom or beauty. An additional, internal quantum number called color is associated with each

Table 1.1: Elementary fermions and their properties.

	Flavor	Charge (Q/e)	Baryon #	Lepton #
Leptons	e μ τ	-1	0	1
	ν_e ν_μ ν_τ	0	0	1
Quarks	u c (t)	$\frac{2}{3}$	$\frac{1}{3}$	0
	d s b	$-\frac{1}{3}$	$\frac{1}{3}$	0

quark. The color quantum number was invoked to explain the spectroscopy of hadrons. A list of the lepton and quark families is given in table 1.1 along with a few of their properties.

Within the Standard Model, the three strongest of the four forces are explained in terms of the exchange of a virtual, gauge boson between the interacting fermions. These gauge particles are the quantized fields of the three forces and are associated with a symmetry group. The strong force is represented by the group $SU(3)$ and has eight generators or field quanta called gluons. The $U(1)$ group represents the electromagnetic interaction and is described by a single generator, the photon, while the weak force is described by the $SU(2)$ symmetry group having three field quanta called intermediate vector bosons (W^+ , W^- , Z^0). The Standard Model is often described in terms of a product of these symmetry groups, $SU(3) \times SU(2) \times U(1)$.

1.1 Quantum Chromodynamics (QCD)

The theory of quantum chromodynamics is used to explain the dynamics of the strong force and is similar in structure to quantum electrodynamics with appropriate changes to the coupling constants at the vertices of the Feynman diagrams. However, due to the non-abelian nature of the SU(3) symmetry group, gluons may couple to other gluons. This self-coupling implies that the gluons carry a similar “color charge” as the quarks and gives rise to an additional three gluon vertex in the possible Feynman diagrams. The analog of the three gluon vertex does not exist in quantum electrodynamics because the photon is electrically neutral.

The self-coupling of the gluon field keeps the lines of force between two quarks from diverging when they are separated. Further separation narrows the field flux tube between the quarks until the energy density is sufficient to produce a quark-antiquark pair. Thus the theory effectively predicts the confinement of quarks to hadrons in agreement with the non-observation of charged particles with a fraction of the electron charge. Moreover, the coupling constant at each vertex, α_s , then depends on the distance scale, or momentum transfer, Q^2 , probed. The Q^2 dependence of the coupling constant is given by the equation [1]:

$$\alpha_s(Q^2) = \frac{12\pi}{(33 - 2n_f) \log(Q^2/\Lambda^2)}, \quad (1.1)$$

where n_f is the number of quark flavors, and Λ is an arbitrary cutoff parameter used to avoid divergence. Typical values for Λ measured in experiments

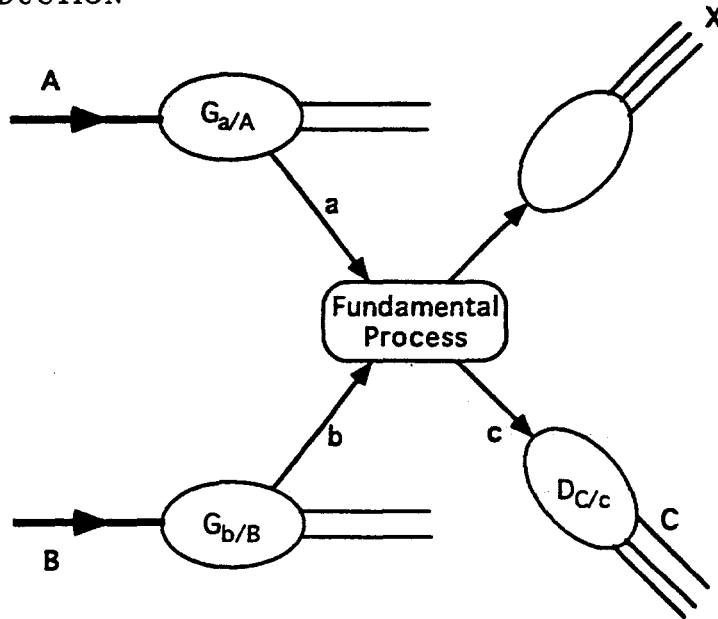


Figure 1.1: Generic hadron-hadron interaction.

vary from 100–500 MeV.

The picture for hadron scattering becomes complicated (refer to figure 1.1). Hadrons have a structure provided by their constituents known generically, as partons. This structure is described by a *structure function*, denoted $G_{a/A}(x_a)$, which gives the probability that the parton, a , carries the fraction, x_a , of the original momentum of the hadron, A . From high energy lepton-hadron, or deep inelastic scattering, we know that roughly half of momentum of a hadron is carried by the charged quarks [1]. This indicates that the other half of the hadron's momentum is in particles which are electrically neutral. One infers that this momentum is carried by the gluon field.

Because quarks and gluons are confined to hadrons, the products of fundamental parton-parton scattering process must be dressed up to form observable hadrons. The hadronization or fragmentation process is described in terms of probability distributions like the structure functions. A fragmentation function, $D_{C/c}(z_c)$ gives the probability that parton c hadronizes into C with momentum fraction z_c . Therefore, the invariant cross section for a typical inclusive hadronic reaction $A + B \rightarrow C + X$, where X may be any final state consistent with energy and momentum conservation, is given by

$$E_C \frac{d^3\sigma}{dp_C^3}(AB \rightarrow C + X) = \sum_{abcd} \int G_{a/A}(x_a, Q^2) G_{b/B}(x_b, Q^2) \frac{\hat{s}}{\pi z_c^2} \frac{d\sigma_{ab \rightarrow cd}}{d\hat{t}} \times \delta(\hat{s} + \hat{t} + \hat{u}) D_{C/c}(z_c, Q^2) dx_a dx_b dz_c. \quad (1.2)$$

The terms \hat{s} , \hat{t} and \hat{u} , are the usual Mandelstam variables for the parton scattering process while the delta function ensures energy and momentum conservation at the parton level.

Hadronization confuses much of the information from the parton level processes, and original hadron structure. Therefore, to disentangle hadronic interactions, one would like a probe that is independent of the hadronization process. Colliding beam experiments ignore the hadronization process altogether by observing the jet structure (hadronic spray) of an event to probe the parton processes and hadron structure. Other methods using prompt photons or the production of bound states of a heavy flavor quark-antiquark pair also eliminate the hadronization process. The complications of using the last two methods to determine structure functions come about by not

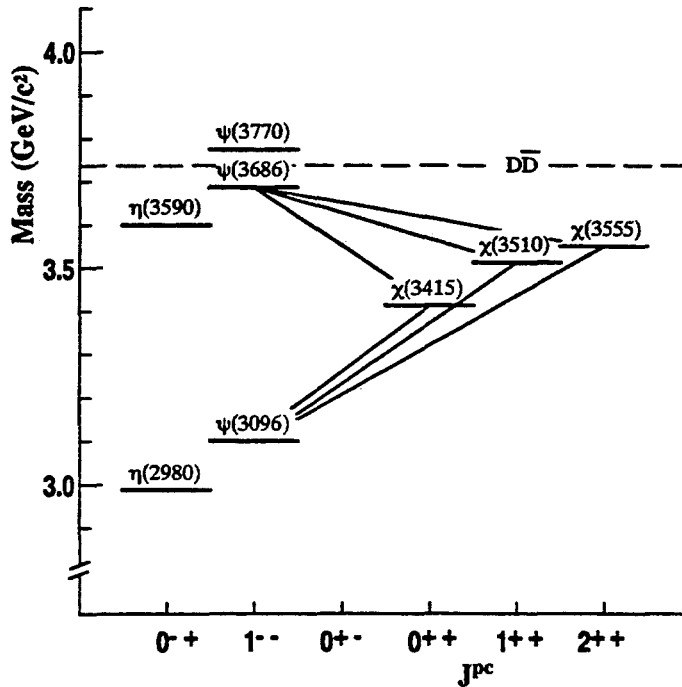


Figure 1.2: Charmonium level diagram.

knowing which fundamental, parton level, process is involved in the production of the final state. This dissertation addresses the later problem for the production of the charmonium triplet P states.

1.2 Charmonium System

Charmonium is a set of bound states of a charm quark with its antiparticle. The level diagram for this system has similar features as that for positro-

nium [2] (bound electron positron) and is shown in figure 1.2. The level splittings between different orbital angular momentum states and the splittings between different total angular momentum states with a given orbital angular momentum quantum number are given by the usual spin-orbit and spin-spin interactions between the quark and antiquark*. The allowed levels and the selection rules for charmonium are only slightly modified from positronium due to the added color degree of freedom. Hence, simple E1 electromagnetic transitions describe the decays of the 1^3P_1 or chi states into the 1^3S_1 or J/psi state. The standard spectroscopic notation of $n^{2S+1}L_S$ is used, where n is the radial quantum number, S is the total spin of the system and L is a symbol which denotes the orbital angular momentum.

The branching ratios for the triplet P (chi) radiative decays has been measured and is quite large for the J=1 and J=2 states (0.66 ± 0.18 %, 27.3 ± 1.6 % and 13.5 ± 1.1 % J=0,1,2, respectively [36]). The triplet S state (J/psi) decays into oppositely charged muons 5.97 ± 0.25 % of the time [36]. The muon decay mode forms a particularly simple experimental signature. It has also been determined that 40 ± 4 % of the measured J/psis from pion nucleon reactions and 30 ± 0.04 % come from proton nucleon reactions come from chi decays [3].

There are four diagrams up to order α_s^4 thought to be responsible for the production of the chi states. These diagrams are presented in figure 1.4 and are often referred to by the names *gluon fusion* (figure 1.3 a), *light*

*The relativistic correction term in charmonium is small due to the large rest mass of the charm quark ($\approx 1.5 \text{ GeV}/c^2$).

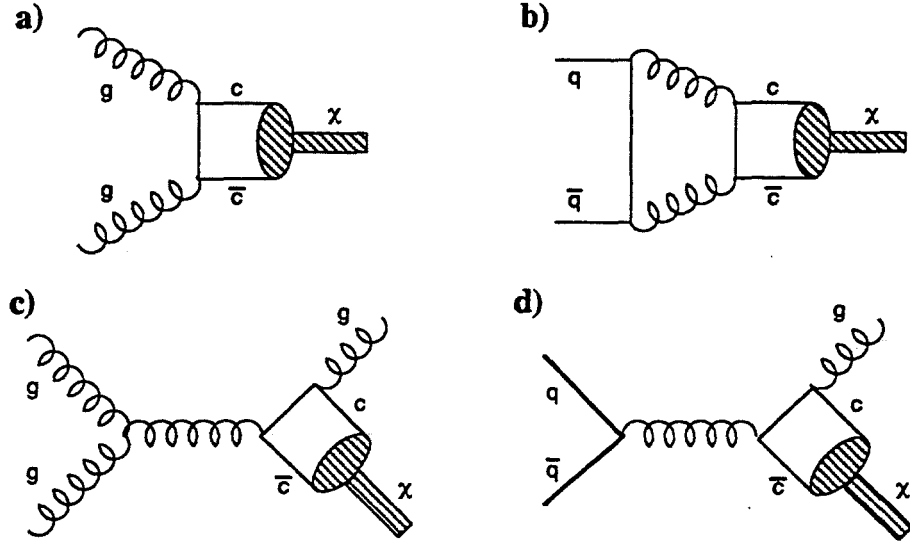


Figure 1.3: Lowest order Feynman diagrams for charmonium production: a) gluon fusion, b) quark-antiquark fusion, c) and d) color evaporation.

quark fusion (figure 1.3 b) and color evaporation (figure 1.3 c-d). The gluon and light quark fusion mechanisms produce charmonium directly in a color singlet, whereas the color evaporation model “evaporates” a soft gluon in order to conserve color. The mechanisms in figures 1.3 a,b,d have been shown [4, 5, 6, 7] to give definite predictions for the relative abundances of the three separate chi states and the angular distributions of their decay products. The relevant angles for the decay products are defined in the chi rest frame and presented in figure 1.4. The angular distributions follow the form:

$$\frac{dN}{d \cos \theta_\gamma} = 1 + \alpha \cos^2 \theta_\gamma \quad (1.3)$$

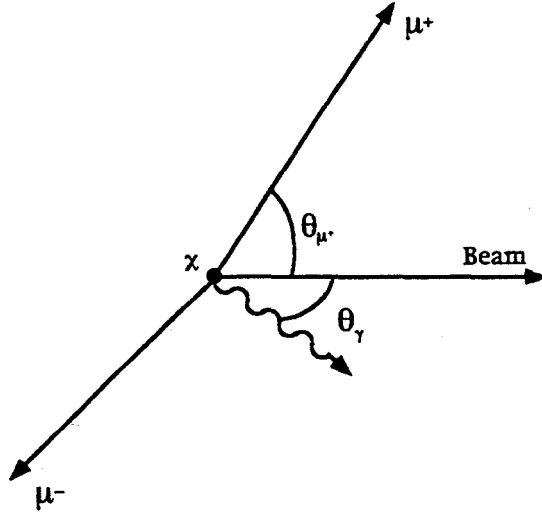


Figure 1.4: Definition of chi decay angles.

$$\frac{dN}{d \cos \theta_{\mu^+}} = 1 + \beta \cos^2 \theta_{\mu^+}, \quad (1.4)$$

where the constants α and β depend on the chi state produced and the production mechanism. For the production mechanisms considered in figure 1.3 these constants are equal ($\alpha = \beta$) for the photon and muon distributions of a single spin state. The predictions of the various production mechanisms are given in table 1.2.

1.3 Previous Experiments

Previous measurements of the hadroproduction of charmonium and the subsequent measurement of structure functions have concentrated on the J/psi and psi prime ($\psi(1S)$ and $\psi(2S)$, respectively). These early experiments,

Table 1.2: Predicted chi production ratios and angular distribution parameters.

Mechanism	$\sigma_{\chi_0} : \sigma_{\chi_1} : \sigma_{\chi_2}$	α_{χ_1}	α_{χ_2}
gluon fusion	3:0:4	0	1
light quark fusion	0:4:1	-1/3	-1/3
color evaporation ($q\bar{q}$ only)	1:3:5	1/5	21/73

particularly those with closed geometry (only detecting specific particles), ignored the contributions to the number of J/psis from the decays of more massive charmonium states [†]. More recently, open geometry experiments have tried to rectify this situation by detecting the radiative photon from chi decay or the pions from psi prime decay ($\psi' \rightarrow J/\psi 2\pi$). The results of these experiments indicate a substantial part, 30–50% depending on beam type of the J/psi cross section comes from the decay of these particles [8, 10, 12, 13, 3, 14]. However, only a three experiments observe sufficient numbers of chis and have good enough resolution to do even a statistical separation of the two states.

Three publications concerning P-wave charmonium came from the groups using the Chicago Cyclotron Magnet facility at Fermilab. The experimental setup of these experiments is shown in figure 1.5 with ≈ 200 GeV negative pion and proton beams incident on a beryllium target. The trigger for these experiments were a massive opposite sign dimuon with the photon being re-

[†]A good review of J/psi and psi prime production may be found in reference [41]

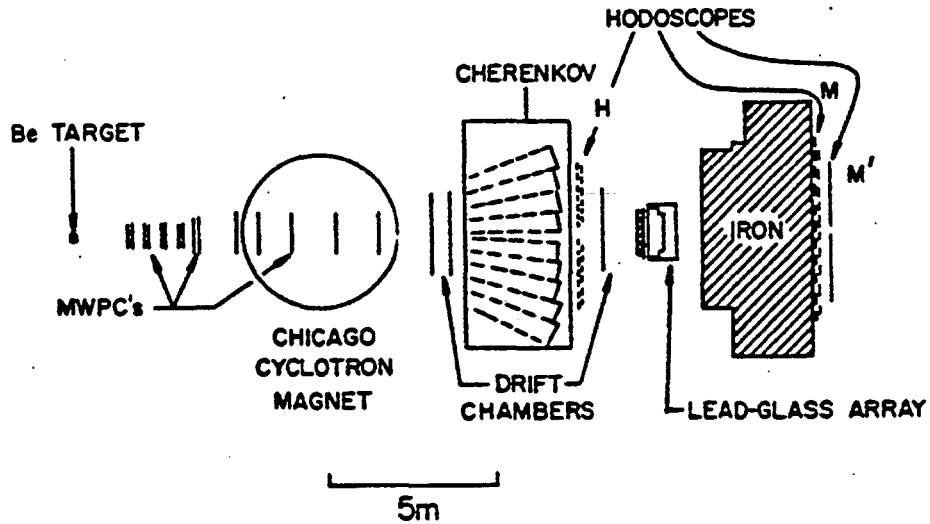


Figure 1.5: Experiment layout for the Chicago Cyclotron Magnet facility [10, 13].

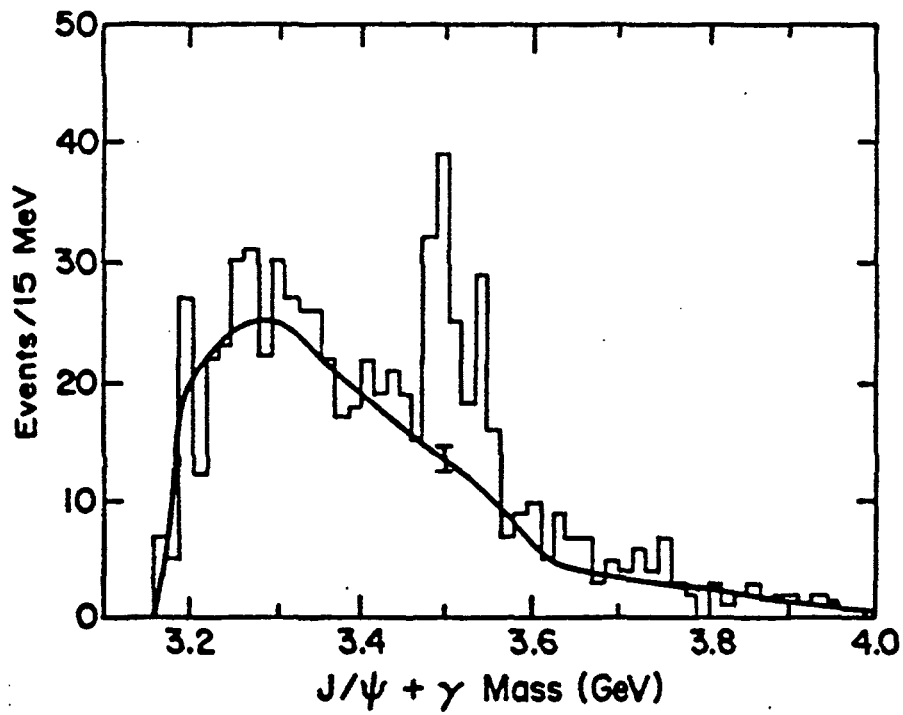


Figure 1.6: $J/\psi\gamma$ invariant mass distribution for π^- Be reactions. The data is from reference [13].

constructed in a small lead glass electromagnetic calorimeter covering only the central region of the spectrometer. The earliest experiment [9] makes no prediction on the relative abundances of the produced chi states due to their poor mass resolution ($\approx 60 \text{ MeV}/c^2$). An improved electromagnetic calorimeter reduced the mass resolution to $15 \text{ MeV}/c^2$ for the two subsequent papers [13, 10]. The J/psi-photon invariant mass distributions from the second and third papers are shown in figures 1.6 and 1.7. The measured production ratio from their pion beam data are consistent with the color evaporation model using a quark-antiquark annihilation process or an admixture of several processes. Little can be determined from the proton data since their entire signal is in a single bin peak and is statistics limited. However, the data seem to indicate a predominance of the J=2 chi state.

The spectrometer setup used by the WA11 experiment at CERN is shown in figure 1.8. This experiment used a 185 GeV negative pion beam incident on a beryllium target. Again, the trigger was on massive dimuons. The chi decay photon was detected using two methods. The first was to reconstruct a photon in their calorimeter in which the mass resolution was such that the two states could not be resolved [11]. The second method looked for photon conversions in one of the beryllium foils. The mass resolution for the chi states was significantly improved with the invariant mass distribution for the reconstructed J/psi- e^+e^- final state shown in figure 1.9. The production ratio of the two higher mass chi states indicates a color evaporation or admixture of production mechanisms. Although, this experiment has well separated

chis the uncertainty is limited by the number of chis reconstructed.

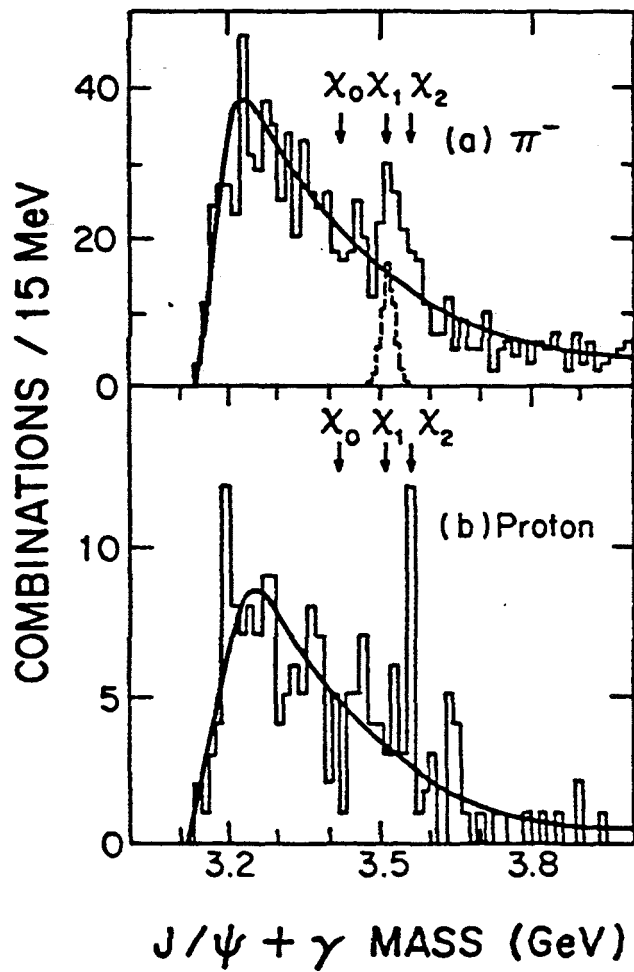


Figure 1.7: J/ψ -photon invariant mass for (a) π^- beam and (b) proton beam. The data is from reference [10].

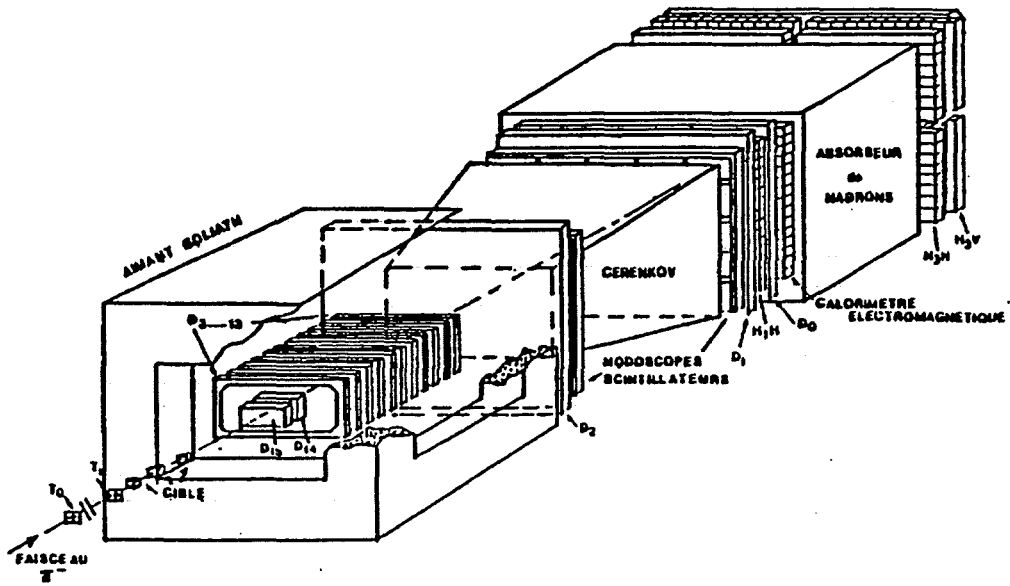


Figure 1.8: The WA11 spectrometer at the CERN SPS.

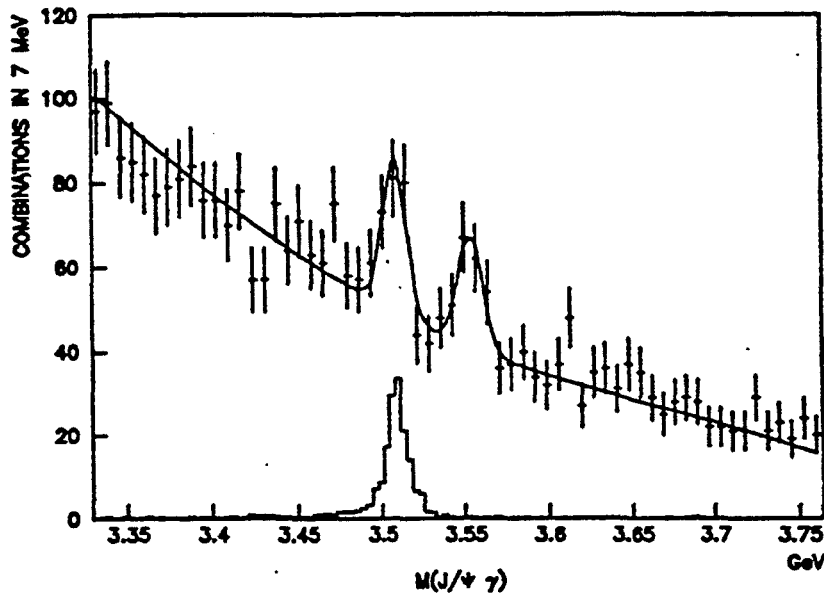


Figure 1.9: $J/\psi e^+e^-$ invariant mass spectrum. The data is from reference [12].

Chapter 2

Experiment Apparatus

Experiment 705 took place in the High Intensity Laboratory (HIL) facility at the Fermi National Accelerator Laboratory in Batavia, Illinois, USA. The experiment ran as part of the fixed target program at Fermilab for a nine month period beginning in June of 1987 and ending in February of 1988.

As a prelude to the description of the apparatus it is beneficial to introduce the coordinate system used in the experiment. Nearly all of the descriptions that follow will use the system defined here. The z axis is defined as the direction of the beam, and the y axis was up, away from the earth; the x axis is then fixed by requiring a right handed coordinate system. The origin is taken to be the center of the experiment's main analysis magnet, PW8AN2, or "Rosie", which is discussed further in the spectrometer section of this chapter.

2.1 Accelerator

Protons were accelerated up to their final extracted energy of 800 GeV in several stages by a series of successively more powerful accelerators. The process began with H^- ions being accelerated first to 8 keV and then to 200 MeV by a Cockroft-Walton electrostatic accelerator and a linear acceler-

ator, respectively. The electrons were then stripped off and the bare protons injected into three sequentially more powerful synchrotrons. The first two synchrotrons, the Low Energy Booster and the Main Ring, used conventional magnets to contain the beam. The Low Energy Booster raised the proton beam energy to 8 GeV while the Main Ring boosted it to 150 GeV. The final stage of acceleration occurred in the Tevatron and brought the energy up to 800 GeV and held it there during the extraction process. The Tevatron occupied the same tunnel as the Main Ring but used the higher magnetic fields of superconducting magnets to keep the beam in its circular orbit. During normal running conditions, the whole acceleration process took 31 seconds with the 800 GeV beam being extracted from the Tevatron over a 23 second "spill".

Once the beam was extracted it was split and directed to the three principle experiment areas, Proton, Neutrino, and Meson. Each of these primary beam lines was further split to deliver beam to the individual experiments within each area. For example the proton beam was split three ways into the Proton East, Proton Center and Proton West beam lines. Experiment 705 was located in the High Intensity Laboratory at the end of the Proton West beam line.

2.2 Beam/Beam Line

The 300 GeV pion and proton beam used in the experiment was produced by operating the beam line (figure 2.2) in one of two modes, called charged

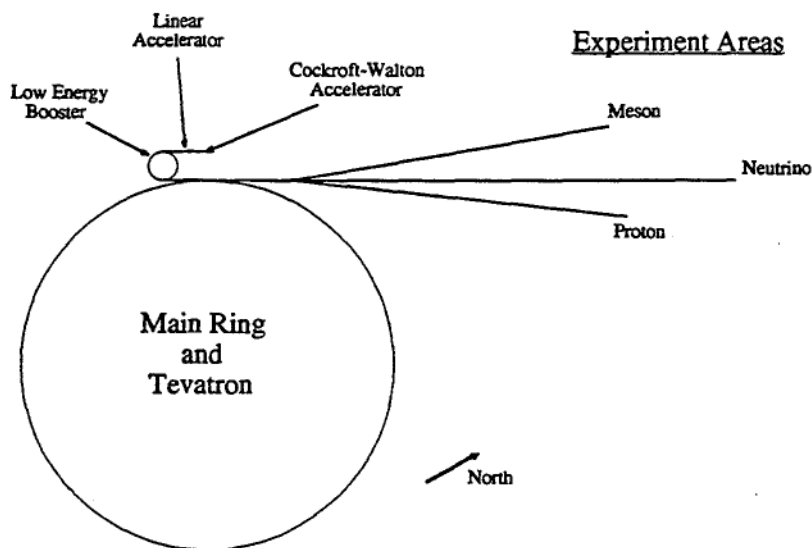


Figure 2.1: Schematic diagram of the Fermilab accelerators and principle beam lines.

and neutral. In the charged mode, the primary proton beam was directed into a Be target and the interaction products, protons and pions were bent away from the primary beam axis. The majority of the interaction products, protons and pions, formed the secondary beam. The momentum and charge sign of the secondary particles was selected by tuning the value and polarity of the magnetic field of PW6W3 and the controlling the apertures of the collimators PW6MS1-2 (momentum slit) and PW6CH2. A Pb foil, EKILLER, was inserted in the beam to remove any stray electrons produced in the primary interaction.

The beam composition in the positive charged mode was determined to be 53% protons, 42% pions and 4.6% kaons, while in the negative charged

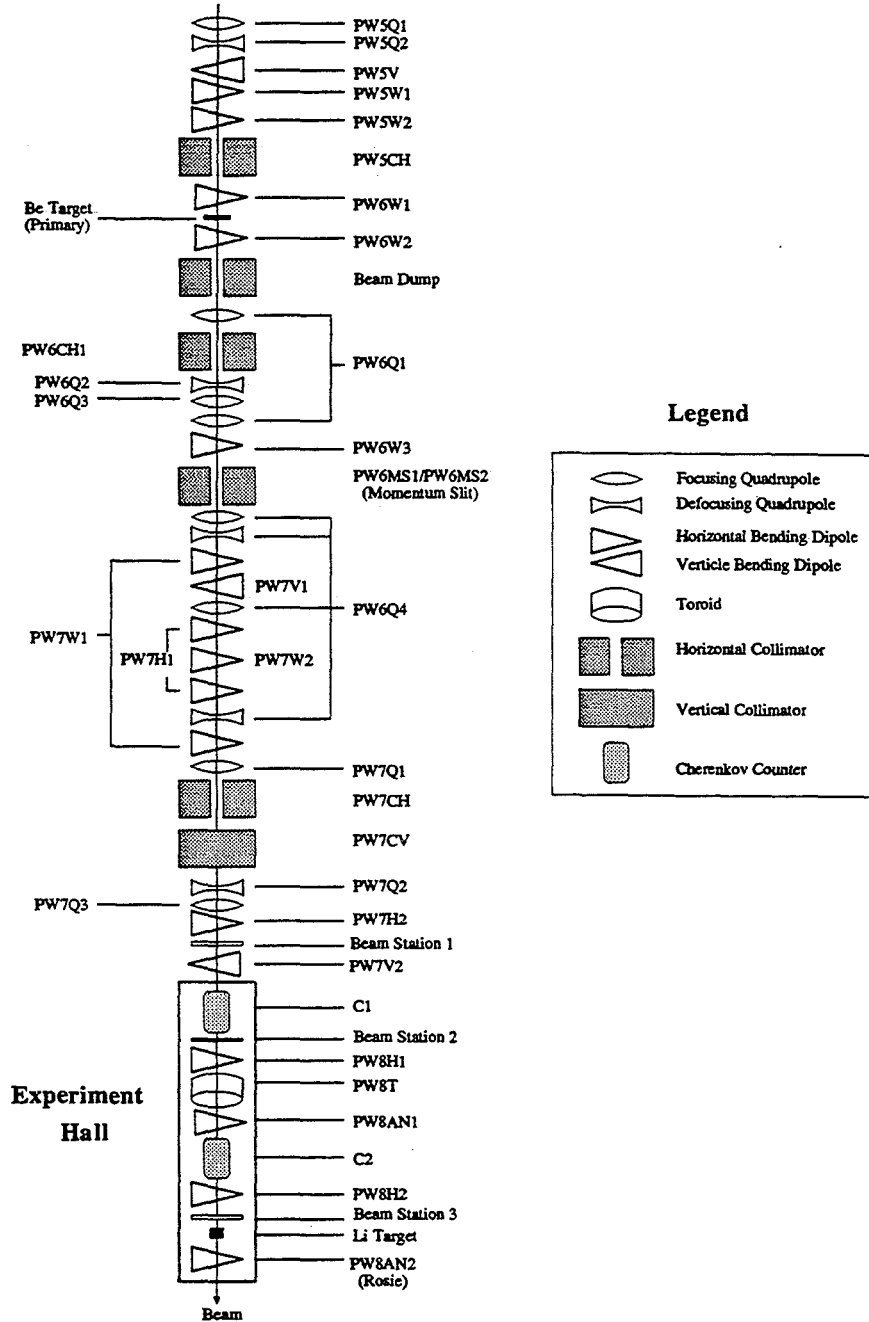


Figure 2.2: Schematic diagram of the E705 beam line. Focusing/defocusing quadrupoles focus/defocus in the horizontal plane and defocus/focus in the vertical plane.

mode we had 1.1%, 93%, and 6% protons, pions and kaons, respectively.

In the neutral mode, the primary proton beam hit the target at zero degrees and PW6W2 was operated at full power. The magnet, PW6W2, was used to sweep all charged particles, including the non-interacting primary beam, into the beam dump collimator leaving a secondary beam of only neutral particles. The decay of Λ^0 , $\bar{\Lambda}^0$, K^0 , and \bar{K}^0 particles produced a tertiary beam of protons, antiprotons, π^+ , and π^- particles. Again, the momentum of the beam was determined by adjusting the magnets/collimators as previously described. Although the beam yield was down when operating in the neutral mode (5×10^{-6} particles/primary proton vs 3×10^{-4} particles/primary proton in the charged mode), the ratio \bar{p}/π^- was enhanced to 8% with no charged kaon contamination (\bar{p}/π^- yield was 1.2% in the negative charged mode).

Our positive beam data was taken in the charged mode since the relative amount of protons and pions were nearly equal. However, to optimize our antiproton and total beam yields we took our negative beam data in a hybrid mode (admixture of charged and neutral modes). Our antiproton content in this hybrid mode was measured to be 4%.

In the neutral mode, photons also accompanied the other neutral particles previously described and by placing a thin Pb foil, EMAKER, in the beam and removing EKILLER, the photons could be converted into e^+/e^- pairs, thereby producing an electron/positron beam. By adjusting the magnets and collimators, the momentum of the beam could be varied between

2–100 GeV/c and was used to calibrate the electromagnetic calorimeter.

2.2.1 Beam Stations

The beam trajectory into the secondary (experiment) target was determined using three beam stations. Each station consisted of eight scintillation counters parallel to the x axis (BY counters) and three planes of proportional wire chambers referred to as beam chambers (BC). The BY counters were positioned with their long sides parallel to the x axis of the experiment and gradually increased in width from the center of the beam toward the edges to equalize the particle rate through each counter. Each set of counters covered an area 13 cm^2 and were used as part of the trigger to veto events with more than one beam particle. The BY counters were located 67.5, 42.4, and 10.1 m upstream of our analysis magnet.

The beam chambers each consisted of three planes of proportional chambers giving y , u , and v views. In the v and u views the wires were rotated through an angle θ_{yx} relative to the y view. With θ_{yx} chosen to be -60° and $+60^\circ$ for the u and v views, respectively, the uncertainty in the measurement of the x position of the beam was the same as that for the y measurement.

The signals from the beam chambers were recorded with a custom electronic amplifier and latch system. Physical parameters for these chambers are summarized in table 2.1.

Table 2.1: Physical parameters for the beam chambers.

Chamber	Plane	# Wires	z (cm)	Pitch (cm)	Length (cm)	θ_{yx} (rad.)
BC1	y	128	-6715.0	0.100	12.700	0.0000
	u	128	-6730.0	0.100	12.700	-1.0472
	v	128	-6722.0	0.100	12.700	1.0472
BC2	y	128	-4260.0	0.100	12.700	0.0000
	u	128	-4253.0	0.100	12.700	-1.0472
	v	128	-4245.0	0.100	12.700	1.0472
BC3	y	128	-1030.0	0.100	12.700	0.0000
	u	128	-1022.0	0.100	12.700	-1.0472
	v	128	-1014.0	0.100	12.700	1.0472

2.2.2 Čerenkov Counters

Beam particles were identified by two threshold Čerenkov counters. Both counters were filled with He, which, under normal running conditions, were at a pressure of 1.8 psi. At 300 GeV this pressure setting gave signals for pions, but not protons. During the electron calibration of the electromagnetic calorimeter the pressure in the chambers was adjusted to distinguish between electrons and pions at the beam energy.

2.3 Spectrometer

The E705 spectrometer (figure 2.3) consisted of several multiwire proportional and drift chambers, a large aperture analysis magnet, an electromagnetic calorimeter and muon identification hodoscopes.

The wire chambers were used to reconstruct the line segments of charged particle paths between the target and Rosie (upstream tracking) and between Rosie and the calorimeter (downstream tracking). By measuring the

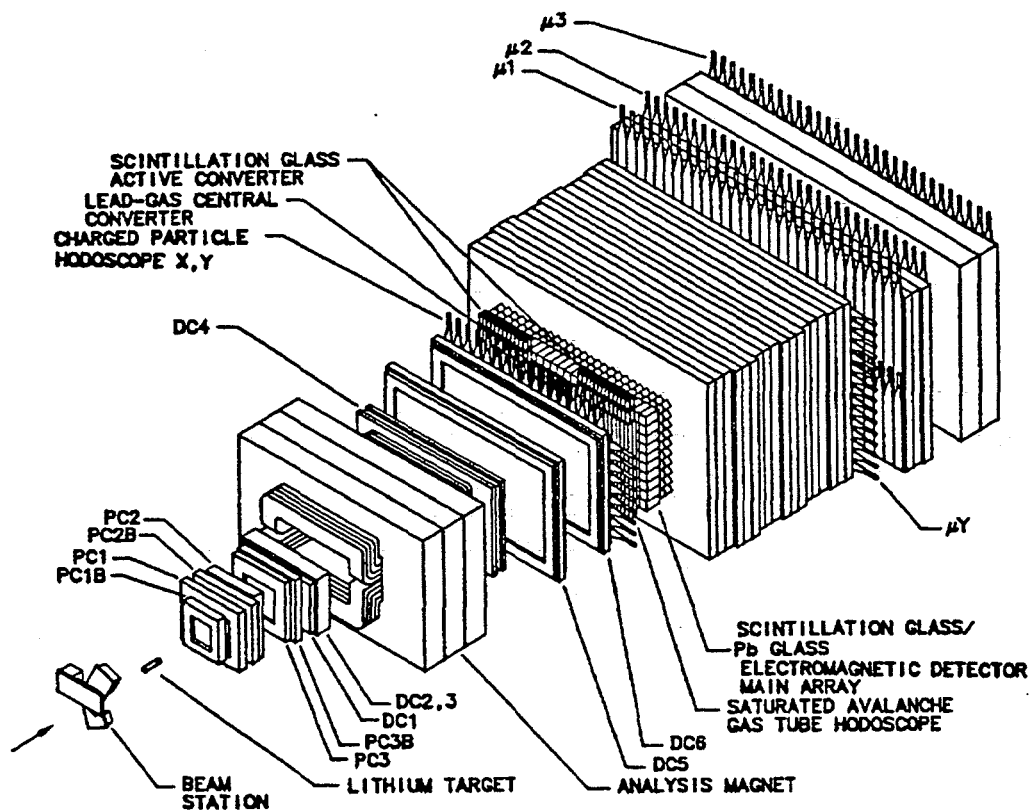


Figure 2.3: The E705 spectrometer.

deflection between an upstream and a downstream line segment and knowing the magnetic field from the magnet one gets the momentum of the charged particle traversing this path. Nineteen planes of proportional chambers and nine planes of drift chambers constituted the upstream tracking, while the downstream tracking was made up of twelve planes of drift chambers.

Downstream of the last drift chamber was the electromagnetic calorimeter system which was used to measure the position and energy of photons and electrons. This system also provided some degree of particle identification

(identifying electrons from other charged particles). The calorimeter was composed of four separate devices, a lead gas calorimeter (LGC), the Active Converter (AC), the Gas Tube Hodoscope (GTH) and the Main Array (MA).

Nine different scintillation hodoscopes, located throughout the spectrometer, provided the fast information needed to decide whether an interaction took place and if it was interesting enough for further study (trigger). Upstream of the target, timing and beam halo information were given by the T1 and VETO (VX, VY) hodoscopes, respectively. The charged particle hodoscopes (CPX, CPY) gave multiplicity and coarse position information for charged particles between the last drift chamber and the electromagnetic calorimeter. Past the electromagnetic calorimeter, behind three shields of copper and steel, steel, and concrete were the four muon hodoscopes. As the name implies, these were used to identify and crudely track muons.

2.3.1 Target

The target used in this experiment was a cylinder of ${}^7\text{Li}$ 10 cm in diameter and 33 cm long. It was located 533 cm upstream of the center of the main analysis magnet. This target was chosen because it satisfied the following criteria:

- ${}^7\text{Li}$ has nearly isotopic spin zero (nearly the same number of protons and neutrons). This makes the interactions induced by π^+ and π^- beam particles similar.

Table 2.2: Physical parameters for the proportional chambers.

Chamber	Plane	# Wires	z (cm)	Pitch (cm)	Length (cm)	θ_{yx} (rad.)
PC1B	v	176	-427.797	0.0750	30.00	-0.4899
	x	176	-427.198	0.0750	30.00	0.0000
	u	176	-426.596	0.0750	30.00	0.4899
PC1	x'	352	-406.425	0.1514	29.00	0.0000
	v	348	-405.155	0.1514	29.00	-0.2915
	x	352	-403.885	0.1514	29.00	0.0000
	u	349	-402.615	0.1514	29.00	0.2915
PC2B	v	176	-380.543	0.0750	40.00	-0.4899
	x	176	-379.943	0.0750	40.00	0.0000
	u	176	-379.341	0.0750	40.00	0.4899
PC2	u	480	-334.960	0.1507	39.40	0.2915
	x	480	-333.690	0.1507	39.40	0.0000
	v	480	-332.420	0.1507	39.40	-0.2915
PC3B	v	160	-244.940	0.1000	50.00	-0.4899
	x	160	-244.340	0.1000	50.00	0.0000
	u	160	-243.738	0.1000	50.00	0.4899
PC3	v	512	-266.799	0.2000	50.00	-0.2915
	x	512	-265.580	0.2000	50.00	0.0000
	u	512	-264.361	0.2000	50.00	0.2915

- Small atomic number simplifies the calculation of nuclear effects, such as secondary interactions within a nucleus.
- ${}^7\text{Li}$ has a favorable ratio of interaction to radiation lengths. A large ratio increases the probability of an interaction while allowing photons to escape the target. The interaction length, Λ_T , for ${}^7\text{Li}$ is 197 cm for 300 GeV pions with a radiation length, X_0 , of 155 cm. This gives an interaction probability of 15.4% and a maximum photon conversion probability of 15.2%.
- Lithium is solid at room temperature, making it relatively easy to handle.

2.3.2 Proportional Chambers (PCs and PCBs)

Proportional chambers were used to record points on the trajectories (tracks) of charged particles passing through them, upstream of the main analysis magnet. The chambers located upstream of the target were referred to as beam chambers (BCs), which were discussed above. The proportional chambers between the target and the main analysis magnet were designated PCs or PCBs depending on the size of the active region of the chamber; the PCBs active area covered only a small region near the beam axis. All of the chambers were operated with “magic gas,” which was a mixture of 70% argon, 29.6% isobutane and 0.4% freon. Table 2.2 contains the physical parameters for the proportional chambers.

The PCs consisted of three planes (four for PC1) of wires in x , u , and v views with the wires at an angle, θ_{xy} , relative to the y axis in the xy plane. The wires were made of gold plated tungsten with a diameter of 12, 20, and 20 μm for PC1, PC2, and PC3, respectively.

Every plane of the PCs had a circular region in the center of each plane desensitized to reduce the single wire hit occupancy near the beam axis. This deadening was accomplished by electroplating CuS onto the wires to double their thickness in the appropriate place. The radius of these dead regions was 5.08 cm for PC1 and PC2 and 6.35 cm for PC3. Each wire had its signal amplified and latched with Nanometric Company’s N-277D amplifier, and N-278 latch.

The desensitized regions of the PCs were covered by the PCBs [16] which

Table 2.3: Physical parameters for the drift chambers.

Chamber	Plane	# Wires	z (cm)	Pitch (cm)	Length (cm)	θ_{yx} (rad.)
DC1	u	192	-216.352	0.600	50.80	0.2915
	x	192	-215.717	0.600	50.80	0.0000
	v	192	-215.082	0.600	50.80	-0.2915
DC2	v	92	-194.831	1.270	49.80	-0.2915
	x	93	-193.561	1.270	49.80	0.0000
	u	93	-192.291	1.270	49.80	0.2915
DC3	u	93	-180.861	1.270	50.80	0.2915
	x	92	-179.591	1.270	50.80	0.0000
	v	92	-178.321	1.270	50.80	-0.2915
DC4	v	124	171.991	1.905	99.06	-0.2915
	x	124	173.896	1.905	99.06	0.0000
	u	123	175.801	1.905	99.06	0.2915
	x'	123	177.706	1.905	99.06	0.0000
DC5	x'	176	273.881	1.905	167.64	0.0000
	v	192	275.786	1.905	167.64	-0.2915
	x	176	277.691	1.905	167.64	0.0000
	u	192	279.596	1.905	167.64	0.2915
DC6	x'	176	378.590	1.905	167.64	0.0000
	v	192	380.495	1.905	167.64	-0.2915
	x	176	382.400	1.905	167.64	0.0000
	u	192	384.305	1.905	167.64	0.2915

had a much finer wire spacing. The signals from these wires were amplified and recorded using the same system as the beam chambers.

2.3.3 Drift Chambers

A total of six drift chambers (DCs) were used for the larger areas of the upstream tracking system (DC1–3), closest to the magnet, and for the entire downstream tracking system (DC4–6). These chambers consisted of three or four planes of alternating anode/sense and cathode/field shaping wires. These wires were sandwiched between cathode planes of either aluminized mylar for chambers 2-4, or finely spaced wires for chambers 1, 5, and 6. Once again, the wire rotation angle, θ_{xy} , lies in the xy plane and is measured

relative to the y axis. The signals on the sense wires were amplified and converted to differential ECL signals by the LeCroy 7790 amplifier and sent to the LeCroy 4290 TDC system, operating in common stop mode, which recorded the drift times. All the chambers were operated with a 50/50 mixture of argon and ethane gases.

The central regions of each plane of the drift chambers were deadened similar to the PCs. The dead regions in the upstream chambers corresponded to a circle of radius 6.35 cm while the downstream chambers had a deadened rectangle 30.48×15.24 cm². Table 2.3 lists some of the useful, physical parameters for the drift chambers.

2.3.4 Analysis Magnet (Rosie)

The analysis magnet for the experiment, affectionately known as Rosie, was a large aperture (185.5×91.4 cm²) dipole 152.4 cm in z . The magnet was typically run with a current of 2070 amperes producing a field of 13 kG which corresponded to a transverse momentum “kick” of 0.766 GeV/ c .

A steel “mirror” plate 22 cm thick with a hole 197×113 cm² was placed on the downstream side of Rosie to reduce the fringe field near the electromagnetic calorimeter.

2.3.5 Electromagnetic Calorimeter

A top view of the electromagnetic calorimeter is found in figure 2.4. As previously mentioned, the calorimeter consisted of four separate devices, providing three different functions. The photon converter, hereafter referred

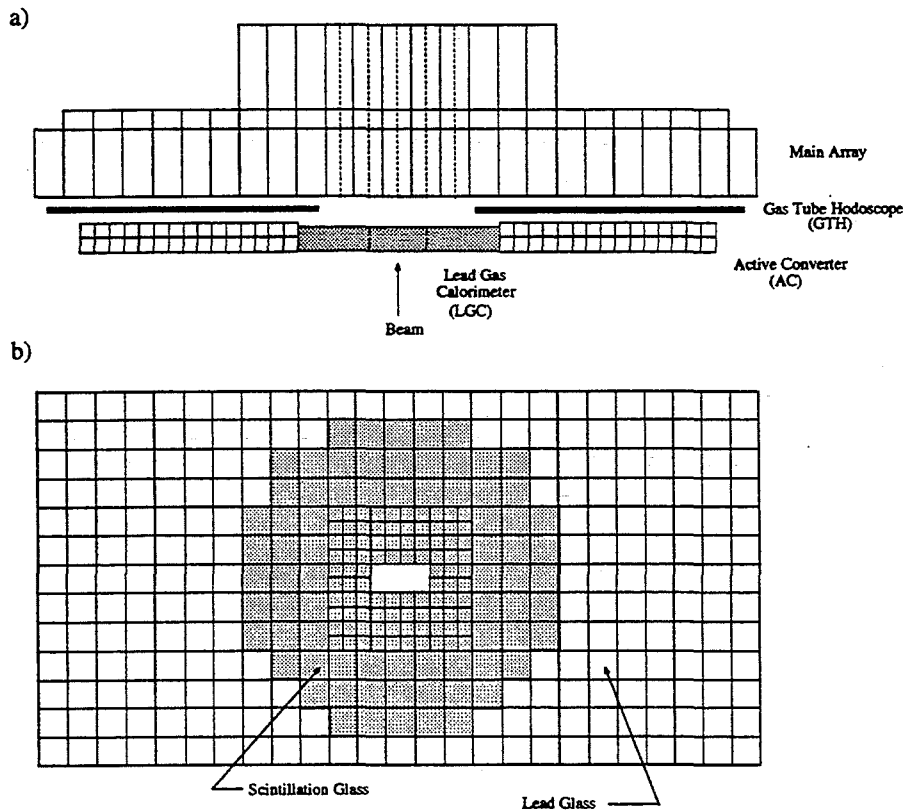


Figure 2.4: E705 electromagnetic calorimeter. a) top view b) Main Array front view.

to as the Active Plane, was designed to convert photons into e^+/e^- pairs beginning an electromagnetic cascade or shower and make an initial sampling of the energy in the shower. Two devices made up the Active Plane, the lead gas calorimeter and the Active Converter. The lead gas calorimeter and the Gas Tube Hodoscope both measured the position of the shower, while the bulk of the energy was measured in the Main Array.

The entire calorimeter was enclosed in its own temperature-controlled house. This house was suspended on a cart capable of positioning any detector element into the path of an undeflected electron beam of known energy for calibration.

Lead Gas Calorimeter (LGC)

The lead gas calorimeter [17] provided both the initial conversion/energy measurement and a position measurement for an electromagnetic shower in the central $103 \times 180 \text{ cm}^2$ section of the calorimeter. A $30 \times 15 \text{ cm}^2$ hole was left in the center of the device to exclude non-interacting beam particles. The LGC was constructed as an eight layer sandwich; each layer consisted of a lead foil, 1 cm proportional tubes, and 0.75 cm copper strips (1.25 cm pitch) clad on fiberglass G-10 material. The proportional tubes ran the height of the detector but were split, electronically, in the middle to provide top and bottom x views. These tubes were operated with a 50/50 argon ethane gas mixture. The tubes in different layers corresponding to the same x position were ganged together to form a single electronic channel. The copper strips were at 90° relative to the proportional tubes and were ganged in a similar manner. Each channel was amplified and the pulse height was digitized by a LeCroy 2280 ADC system.

The LGC provided 4.2 radiation lengths of material for photon conversion including a 1.3 cm thick steel plate which served the dual purpose of a return flux path for Rosie's fringe field and added material for converting photons

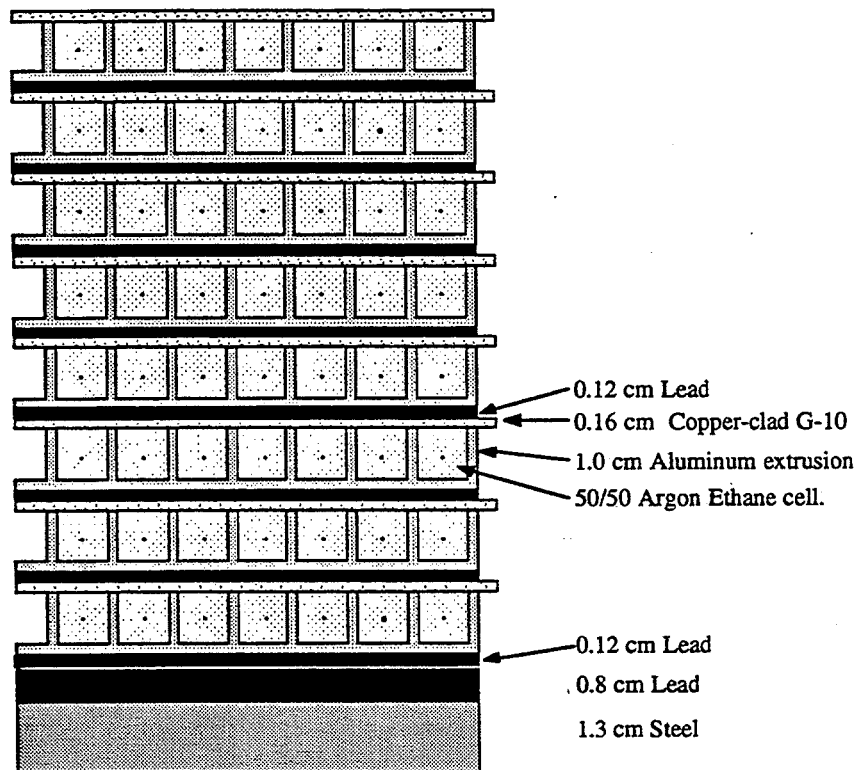


Figure 2.5: Cross section of a portion of the LGC.

immediately upstream of the active part of the device.

Active Converter

The Active Converter provided the initial photon conversion and energy measurement in both of the outer $113 \times 197 \text{ cm}^2$ wings of the calorimeter. This device consisted of 120 blocks of SCG1-C scintillation glass, measuring $7.5^2 \times 97.5 \text{ cm}^3$, in two layers, front (upstream) and back (downstream). Both layers of glass blocks and a 1.3 cm steel plate, immediately upstream,

provided 4.3 radiation lengths of material to start and sample a shower.

The top and bottom blocks of each layer were oriented with their long side parallel to the y axis. Each block was wrapped with aluminized mylar and black vinyl tape to isolate its optical signal. An RCA 6342A photomultiplier tube and its base was attached to one end of a block by a spring mechanism. Optical grease (Dow Corning 92-3067) was used to couple the light signal to the photomultiplier. The high voltage necessary to power the this device was provided by a LeCroy 1440, 256 channel high voltage power supply while the signals were digitized in custom designed precision ADC [18] “charge cards”. An optical fiber from an LED pulser system, described in a subsequent section, was attached to each block to provide gain monitoring throughout the run.

Gas Tube Hodoscope (GTH)

The Gas Tube Hodoscope [23] provided position measurement of an electromagnetic shower in the two outer $136.3 \times 189.8 \text{ cm}^2$ regions of the calorimeter, between the Active Converter and the Main Array. The GTH consisted of two layers of $0.73 \times 1.64 \text{ cm}^2$ polystyrene tubes and 0.8 cm copper strips (1.76 cm pitch) clad on G-10 fiberglass. The tubes were oriented parallel to the y axis and were electronically split in the middle for top and bottom x views. The strips were at 90° relative to the tubes and gave two y views. The two layers of tubes and the two layers of strips were ganged together in a manner similar to that of the LGC tubes and strips. The outermost tubes

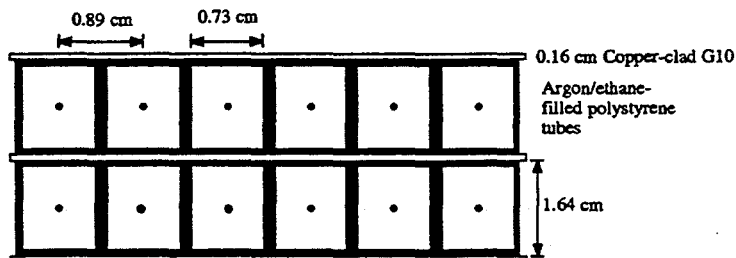


Figure 2.6: Cross section of a portion of the GTH.

($|x| > 85$ cm) were paired side by side to reduce to total number of channels. The signals from each channel were amplified by a circuit similar to that of the LGC and digitized with a LeCroy 2280 ADC system.

Main Array

The Main Array measured the bulk of the electromagnetic shower's energy. It consisted of 392 SCG1-C scintillation glass [20, 19] and SF5 lead glass blocks of four different sizes arranged according to the pattern in figure 2.4b. The two sizes of scintillation glass were $7.52^2 \times 89.2$ cm³, and $15.12^2 \times 89.2$ cm³ ($21.0 X_0$) and occupied the central part of the device. The rest of the Main Array was made of the $15.12^2 \times 45.00$ cm³, SF5 blocks ($18.2 X_0$) with smaller, $14.72^2 \times 35.00$ cm³, blocks ($14.2 X_0$) occupying the sides and top. Properties of each kind of glass are listed in table 2.4. Each block was optically isolated and coupled to its photomultiplier in a similar manner as the Active Converters. Five inch, EMI 9791 photomultipliers were attached to the large SCG1-C and SF5 blocks, while three inch RCA 6342A tubes

Table 2.4: Properties of the different glasses used in the electromagnetic calorimeter.

Composition (by weight)	SCG1-C scintillation glass		SF5 lead glass	
		BaO	43.4%	PbO
	SiO ₂	42.5%	SiO ₂	38%
	Li ₂ O	4.0%	K ₂ O	5%
	MgO	3.3%	Na ₂ O ₃	2%
	Ce ₂ O ₃	1.5%		
Density	3.36 g/cm ³		4.08 g/cm ³	
Radiation Length	4.25 cm		2.47 cm	
Absorption Length (for 30–200 GeV π 's)	45.60 cm		42.00 cm	

were attached to the small SCG1-C blocks. Power and digitization for the Main Array was the same as that for the Active Converter.

The digitization of the Active Converter and Main Array signals occurred in custom designed charge amplification/ADC cards. Each of these “charge cards” contained sixteen channels and were designed to accurately cover the large dynamic range and operate at the high rates demanded by the experiment. The photomultiplier signals for each channel were first integrated, shaped and the resultant signal was split. One signal was sent to a variable delay circuit which could produce several copies of its input signal with various delays. A signal delayed by 160 ns was extracted from this circuit and was subtracted from the undelayed signal giving a roughly square analog output signal with its pulse height proportional to the photomultiplier output charge. A 400 ns delayed version of the integrated/shaped photomultiplier signal awaited a trigger. When an event was triggered it produced

two pulses, BEFORE and AFTER, delayed 250 ns relative to each other. The BEFORE and AFTER pulses opened JFET switches to two sample-and-hold capacitors, C1 and C2, storing the state of the integrator/shaper just preceding and during the interaction, respectively. The "before" level on C1 was subtracted from "after" level on C2 by a differential amplifier. The level on C1 was later digitized to three bit accuracy. If the subtracted signal was less than an eighth full scale then it was amplified by eight and a multiplication level was set. A single, multiplexed twelve bit ADC was used to digitize all of the sixteen channels on each card with the ADC output stored in a first-in-first-out (FIFO) register. Each sixteen bit ADC word contained the twelve raw ADC bits, three "before bits" and a multiplication bit. This word gave information about what happened before the interaction and provided effective fifteen bit resolution. The "charge card" was then read out with standard CAMAC commands.

For each Main Array channel there were two copies of the analog output signal from the "charge cards". One copy was sent to the Cluster Finder P_T trigger (described in section 3.4). Except for the channels connected to the blocks on the outer edge of the Main Array, the copy was sent to amplifier/discriminator circuit in a "pick off" module which converted the analog signal to differential ECL. The ECL signal formed the START signal for a LeCroy 4290 TDC system; the common STOP signal for the TDCs was provided by delaying the charge card's BEFORE signal. The pick off module also split the initial shaped charge signal to the energy sum portion

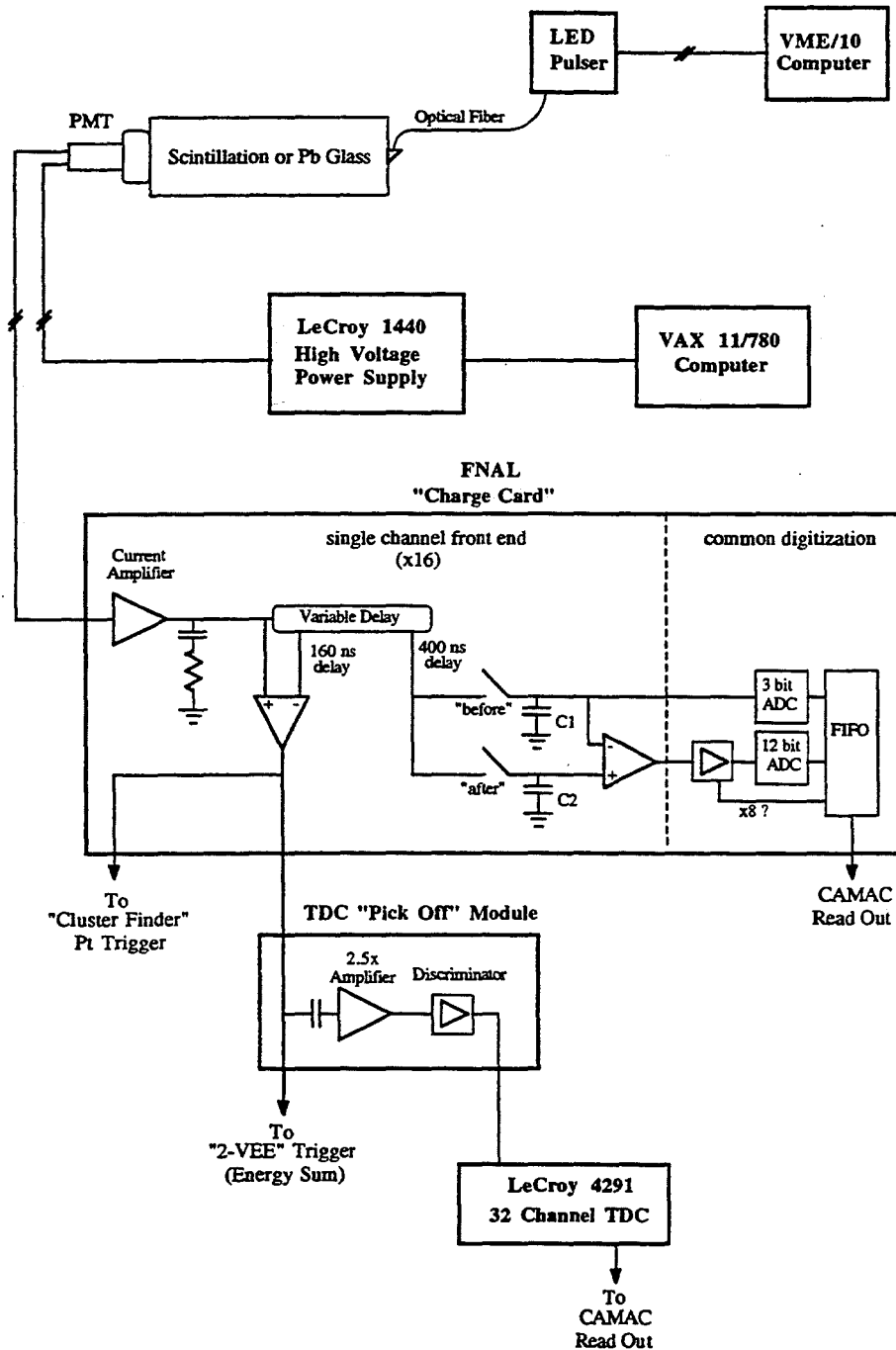


Figure 2.7: Simplified schematic of the calorimeter, glass electronics. The Active Converter blocks used only the ADCs while the outer Main Array blocks were connected to the cluster finder but not to the TDC electronics.

of the 2-VEE trigger (described in section 3.4). Figure 2.7 contains a block diagram of the electronics used for the Main Array.

LED Pulser

Photomultiplier gain and timing of the calorimeter was monitored by an optical pulser system [21, 22]. Light pulses were produced by sending a short 10A pulse through each of a set of LEDs. The light from this pulse was gathered and passed through one of a set of neutral density filters ranging from 0-100% transmission. After the light was filtered it was sent to each of the Main Array and Active Converter blocks via optical fibers. PIN diodes were used to monitor the stability of the light intensity output.

2.3.6 Scintillation Hodoscopes

There were several scintillation hodoscopes employed throughout the experiment to provide fast information used to form a trigger. Each hodoscope consisted of several "paddles" of 1 cm thick scintillation plastic with a Lucite "light pipe" and photomultiplier glued to one end. The entire assembly for each paddle was wrapped in aluminum foil and black plastic. High voltage was supplied to the photomultipliers by a LeCroy 1440 system with the base of each photomultiplier transistorized to help eliminate sag in its gain when operating at high particle counting rates. Signals from the photomultipliers were discriminated and fanned out to be latched or used in subsequent trigger logic. The discriminator level was set just below the minimum ionizing

threshold and the width typically set to 10 ns. The naming convention used for the hodoscopes gives their spatial orientation. The “X” counters have their long side parallel to the vertical axis while the “Y” counters are parallel to the horizontal. The different hodoscopes are described below in more detail.

Experiment Timing (T1)

The timing for the experiment was determined by a hodoscope consisting of a single paddle located just upstream of the target ($z = -671$ cm) referred to as T1. The paddle measured 20.3×10.2 cm² with an Amperex 56AVP photomultiplier collecting the light. The phototube base was transistorized and used two voltage sources, a high voltage source ($V \approx -1700$ volts) for the early dynode stages, and a lower voltage ($V \approx -250$ volts) booster supply to help eliminate gain sagging at high particle counting rates. The width of the discriminated T1 signal was set to 7 ns so that its signal fell within the 10 ns width of the other logic signals, guaranteeing T1 to set the experiment timing.

VETO

The VETO hodoscopes identified events where a halo particle (typically a muon) accompanied the beam. They were located just upstream of the target and were composed of two planes of paddles, VX and VY, located at -636 and -655 cm in z , respectively. Amperex 2212B photomultiplier tubes were

used for these paddles. The 22 VX counters covered an area of $408 \times 147 \text{ cm}^2$ with a beam hole of $25.4 \times 8.8 \text{ cm}^2$, while the VY counters covered an area of $306 \times 153 \text{ cm}^2$ with a hole $8.8 \times 25.4 \text{ cm}^2$ left for the noninteracting beam.

Charged Particle Hodoscopes (CPH)

The charged particle hodoscopes were located between DC6 and the electromagnetic calorimeter and gave a quick charged particle multiplicity measurement used to determine an interaction and provide some position information for the downstream tracking. CPH consisted of two planes of counters, CPY and CPX located in z at 417 cm and 423 cm, respectively.

CPX contained 184 paddles each measuring $3.8 \times 199.4 \text{ cm}^2$ which were split into 92 each top and bottom paddles. This covered a total area of $350 \times 400 \text{ cm}^2$ with a beam hole $32 \times 32 \text{ cm}^2$. Each CPX paddle was glued to an EMI 9807B photomultiplier tube. The top and bottom paddles, corresponding to the same x location, had their signals summed making a single counter.

The 48 CPY paddles each measured $198.4 \times 7.5 \text{ cm}^2$ and were also split into 24 East (negative x) and 24 West counters but were not summed pairwise as with the CPX paddles. Amperex 56AVP photomultipliers were used to collect the light output of the CPY paddles. The total CPY coverage was $400 \times 180 \text{ cm}^2$ with the same size beam hole as CPX.

Muon Hodoscopes

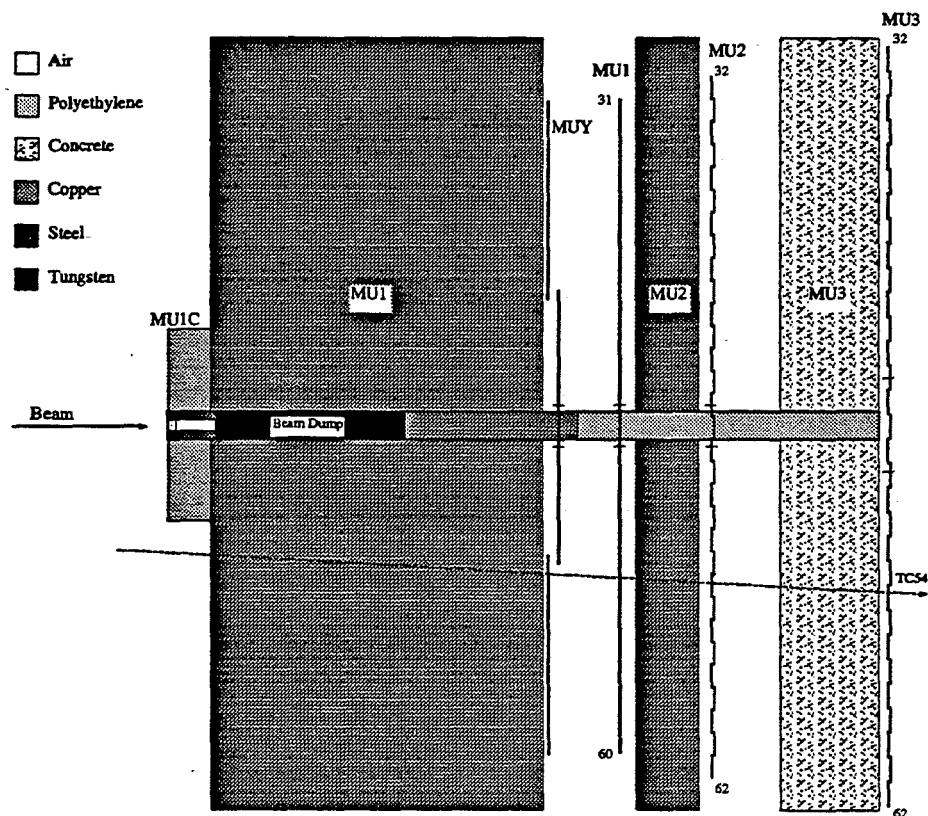


Figure 2.8: Muon detectors, shields, and beam dump. T-54 labels a typical triple coincidence.

Downstream of the electromagnetic calorimeter were four absorber walls, and lurking amongst these absorbers were the four muon hodoscopes, MUY, MU1-3 (figure 2.8). The first absorber (MU1C), with its front face at $z = 739$ cm, was a 40.6 cm thick copper slab covering the central 182×366 cm². A larger (732×366 cm²) steel wall, 309 cm thick, stood immediately behind the copper wall. The third and fourth absorbers (MU2 and MU3) were made of another 61 cm thick steel wall centered in z at 1197 cm, and a 91 cm thick

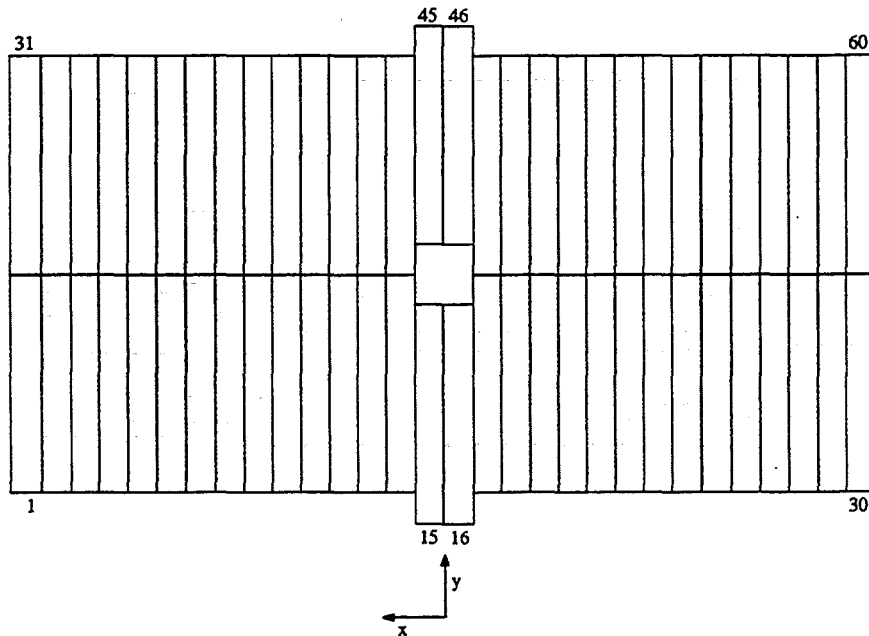


Figure 2.9: MU1 paddle arrangement, beam into page.

concrete wall centered at $z = 1336$ cm. Both of the last two walls covered the same transverse area as the MU1 absorber. A rectangular steel pipe 25.4×15.2 cm², 670 cm long, pierced the center of three muon absorbers. This pipe, filled with polystyrene, steel, and copper, acted as a beam dump for the experiment and helped to eliminate accidental muon counting in the central detectors. The MUY and MU1 hodoscopes occupied the space between the MU1 and MU2 absorbers, while the MU2 and MU3 hodoscopes were immediately downstream of the absorber with the same name. This configuration of absorbers was designed to stop all particles but muons with momentum greater than 6 GeV/c.

The MUY hodoscope was attached to the downstream face of the MU1 shield at $z = 1116$ cm. This hodoscope consisted of 96 paddles in four columns of 24 covering an area 620×285 cm². The paddles of the two inner columns measured 129×13 cm² with a central hole of 40.6×40.6 cm². The slightly larger paddles in the outer two columns measured 187×13 cm².

Attached to the upstream face of the MU2 shield was the MU1 hodoscope ($z = 1181$ cm) made up of 60 paddles in two rows of 30, one above the other. The paddles measured 20.3×185 cm² and covered a transverse area of 618×290 cm². The center four paddles were retracted to leave a hole 40.6×40.6 cm².

The MU2 and MU3 hodoscopes used the downstream face of the corresponding shield for support which located them in z at 1272 and 1436 cm. Both hodoscopes contained 62 paddles in two rows arranged similar to MU1. Each MU2 paddle measured 22.9×157 cm² while the MU3 paddles were 26.7×176 cm². Each paddle in the MU2 and MU3 hodoscopes overlapped its neighbors by 1.3 and 3.5 cm to give transverse coverages of 671×315 cm² and 723×352 cm², respectively. The central hole for MU2 was 40.6×40.6 cm² and 87.6×40.6 cm²), respectively.

2.4 Triggers

Only a small portion of the beam-lithium interactions were of any interest to the experiment. In order to select only the interesting events and keep their number reasonable for subsequent analysis, special logic circuits (triggers)

Table 2.5: Proportion of triggers written to tape and typical prescale values.

Trigger	% to Tape	Prescale Factor
Min. Bias (CF Strobe)	0.6	524288
Two-Vee	0.6	256
PT2 (single photon)	2.2	512
PT3 (single photon)	4.4	8
PT4 (single photon)	4.0	1
Diphoton	10.2	8
Dimuon	78.0	1

were set up to make fast decisions based on the topology of the event in the spectrometer. E705 used eight different triggers: minimum bias (CF strobe), three photon transverse energy thresholds, diphoton, dimuon, Two-Vee, and LED. The minimum bias trigger required only that an interaction took place and was used to monitor detector performance. The other triggers, except the LED, made additional demands on the event topology. For instance, the three photon threshold triggers (PT2, PT3, and PT4) each required a large transverse energy deposition in the Main Array, while the diphoton and dimuon triggers required massive photon and muon pairs, respectively. The Two-Vee trigger looked for two “Vee” decays in the upstream section of the spectrometer. The LED trigger helped to monitor the photomultiplier gain and darkening of the glass in the electromagnetic calorimeter between calibrations and was typically run out of spill.

Each of these triggers occurred with different frequencies with the PT4

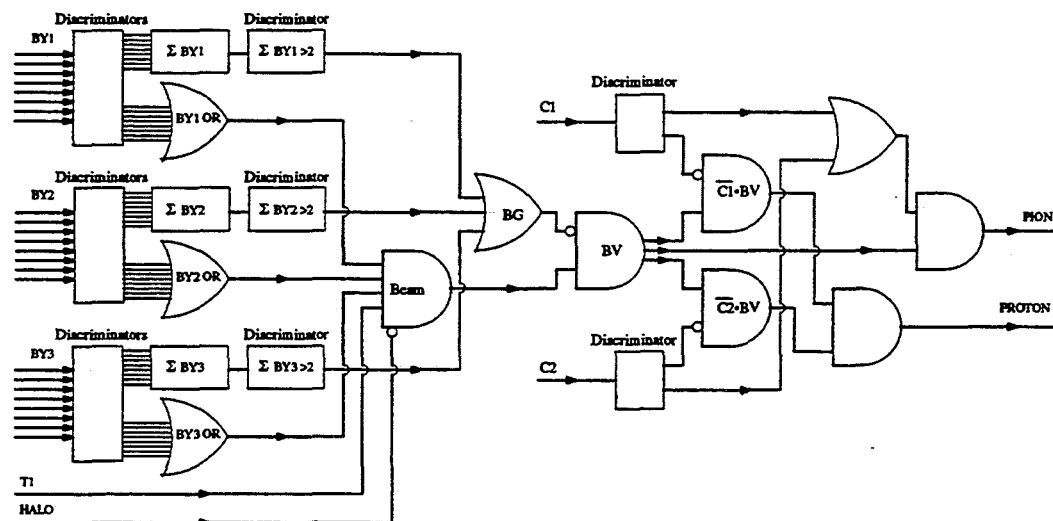


Figure 2.10: Beam definition logic.

and dimuon triggers the rarest and most interesting. When only these two triggers were accepted, during typical beam rates of 6×10^6 particles/s, the data acquisition system was dead reading out the detectors only 5% of the time (dead time). This left room open to accept portions of the other types of triggered events before the maximum acceptable dead time of 20% was reached. The prescale factor for each trigger, defined as the inverse of the fraction of the events accepted satisfying the trigger, was varied depending on the beam conditions to keep the data acquisition dead time near 20%. The percentage of the total events accepted and typical prescale factors are broken down by trigger in table 2.5.

2.4.1 Minimum Bias (CF Strobe)

The lowest requirement for any of the physics triggers was that an interaction took place in the spectrometer. Our interaction definition required a single, tagged beam particle pointing into the target, no accompanying halo particle, and a CPH multiplicity of four. The coincident logic:

$$BV = \overline{(\sum BY1 > 2) + (\sum BY2 > 2) + (\sum BY3 > 2)} \cdot BEAM \quad (2.1)$$

defined a single, halo-less beam particle (figure 2.10), where

$$BEAM = BY1 \cdot BY2 \cdot BY3 \cdot T1 \cdot \overline{HALO}, \quad (2.2)$$

with

$$HALO = (\sum VX > 0) + (\sum VY > 0). \quad (2.3)$$

The summed signals above were, in fact, the analog sum of the appropriate counters discriminated above the indicated single counter level. The discriminated T1 signal set the timing. We used the following for our definitions of a proton and a pion:

$$PION = BV \cdot (C1 + C2) \quad (2.4)$$

$$PROTON = (BV \cdot \overline{C1}) \cdot (BV \cdot \overline{C2}) \quad (2.5)$$

The interaction definition was then:

$$INTERACTION = (PION + PROTON) \cdot (\sum CPX > 2) \cdot (\sum CPY > 2). \quad (2.6)$$

Because the photon triggers took the longest to form and return a decision the experiment used the “strobe” (delayed interaction) signal returning from this trigger as minimum bias. For historical reasons, this was called CF strobe.

2.4.2 Photon Triggers

One of the primary physics goals of E705 was the study of the production of photons at high transverse momentum. To this end, Fermilab designed special trigger electronics called a “cluster finder” [24] which used the pulse height information from the differentiator of each Main Array block (figure 2.7) to perform a fast pattern recognition and locate a potential shower (cluster). The transverse energy of the cluster was estimated and compared with four programmable thresholds, PT1–4. Only the PT2–4 were accepted as single photon triggers while requiring two PT1 triggers in diagonally opposite quadrants formed a diphoton trigger.

2.4.3 Dimuon

A dimuon trigger was formed at two levels. The first level was a fast (10 ns decision time) set of pipeline logic which looked for two well defined muons in different quadrants of the muon detector. The second level trigger actually calculated the invariant mass using the first level triggering muons. A triple coincidence between corresponding counters in the three separate muon hodoscopes identified a good quality muon. A triple coincidence was

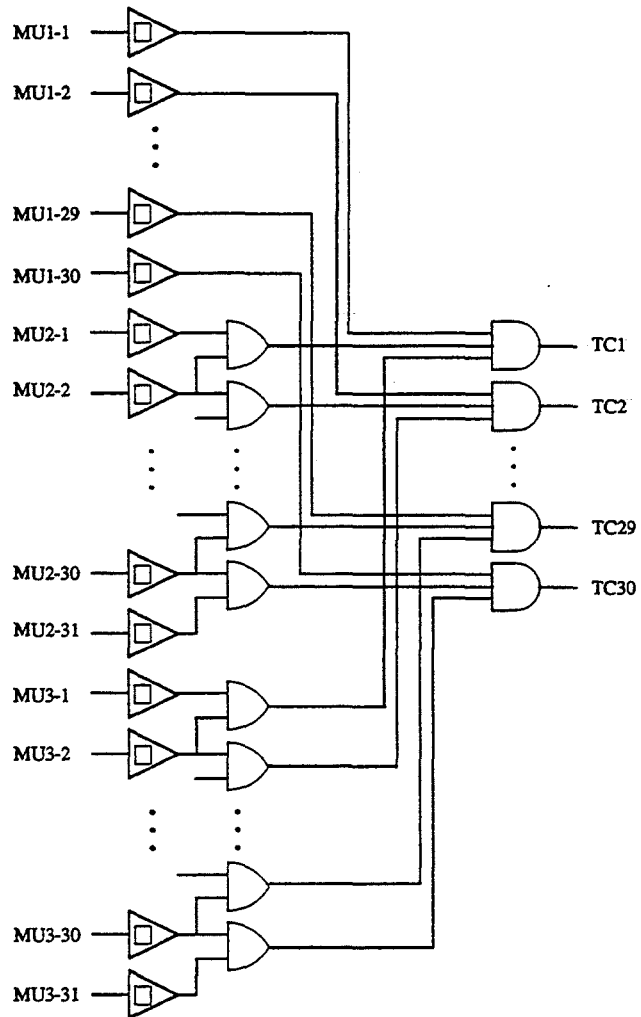


Figure 2.11: Triple coincidence logic diagram. Triple coincidences TC31-TC60 use similar logic.

defined according to the logic:

$$TC_i = MU1_i \cdot (MU2_i + MU2_{i+1}) \cdot (MU3_i + MU3_{i+1}), \quad (2.7)$$

where the subscripts denote the counter number in that plane. The different quadrants were defined as the logical OR of TC1–15, TC16–30, TC31–45 and TC46–60 for quadrants 1–4, respectively. The fast dimuon trigger required two or more triple coincidences in two different quadrants in coincidence with INTERACTION.

When the fast dimuon trigger was satisfied a second level, trigger processor [25], took over to stiffen the selection criteria for the dimuon event. The trigger processor used the information from the triple coincidences to define a “road” in which to look for hits in the x and x' views of the downstream drift chambers. This hit information was used to form crude downstream xz track segments. Upstream segments were constructed by connecting each downstream track in the center of the analysis magnet with the center of the target; the angular difference between the two track segments gave a momentum measurement. Mass combinations were then formed from the tracks pointing at the triggering triple coincidences. Events which satisfied the minimum mass requirement of $2.4 \text{ GeV}/c^2$ were accepted. If the trigger processor took longer than $200 \mu\text{s}$ to decide the event was also accepted.

2.4.4 Two-Vee

The two-vee trigger [26] was designed to enhance our charm sample by looking for the multiplicity change between PC2 and PC3 due to the decay of

strange particles. To this end, the multiplicities in the x and v views of PC2 had to agree ± 1 wire hit as did the same views for PC3. The maximum multiplicity of the two views in PC2 subtracted from the same quantity for PC3 was required to be larger than 2. There was also a Main Array energy deposition requirement ($22.5 < E_{MA} < 37.5$ GeV).

2.4.5 LED

The LED trigger was a special non-physics trigger used exclusively to monitor the gains, pedestals and timing of the photomultipliers in the calorimeter. TTL pulses from a 60 Hz clock were prescaled and sent to the LED pulser [21, 22] and delayed to form a special trigger whose events contained information from only the glass in the calorimeter. We typically ran this out of spill at a rate of 1.875 Hz. However, a small portion of these triggers were also taken in spill to check for rate effects in the calorimeter.

2.5 Data Acquisition and Control

At the lowest level, the data from an event was read out of the detector electronics with a CAMAC (IEEE standard 583) based system. However, several modifications were made on the typical CAMAC system to spend as little time as possible in the readout process during which the spectrometer was unable to accept events. These modifications included:

- Smart Crate Controllers (SCCs) [27] replaced the usual computer mastered controller thus saving command transmission time from the mas-

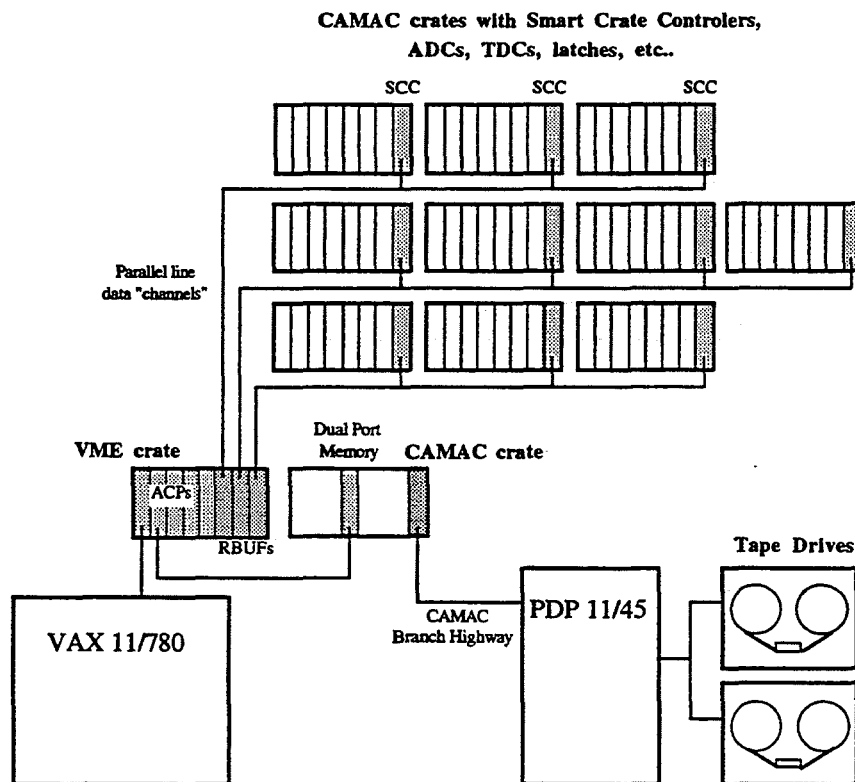


Figure 2.12: Schematic diagram of the E705 data acquisition system. Only three data channels shown for clarity.

ter computer.

- Several CAMAC crates were ganged together in a single data acquisition (DA) channel with all the channels read out simultaneously.
- Buffering events in the ACP (Fermilab Advanced Computer Program) modules allowed data acquisition rates to exceed tape writing rates.

The whole system allowed us to read out an event in ≈ 1.4 ms.

Once a trigger was generated, signals were sent to the first SCC in each DA channel. The SCC read out the data from the devices in its own crate into a special, first in first out buffer (RBUFFs) before passing control on to the next SCC in the channel. Ten ACP units alternately assembled and internally stored the data from each of the channels, contained in the six RBUFFs. At this point a VAX 11/780 could copy events buffered in the ACP modules into pools which were used by various analysis programs to monitor detector performance. The ACPs also downloaded their buffered contents into one of two dual port memories which were read by a PDP 11/45 using standard CAMAC commands. The PDP 11/45 then alternately wrote the data to 6250 bpi data tapes on one of two tape drives. Figure 2.12 is a schematic of the data acquisition system. For more specific information the reader is referred to reference [22].

During a typical run the DA could acquire data during 23 seconds which the experiment received beam, but write data throughout the entire 53 second accelerator cycle. This acquisition rate allowed the experiment to write one 2400 foot, 6250 bpi tape every 10–12 minutes.

Two computers were responsible for the control and monitoring of the experiment. A VAX 11/780, previously mentioned, was primarily responsible for control of the data acquisition system during a run and for testing various electronic components during setup. Secondary responsibilities included online monitoring and diagnostics. A second, VME/10, computer controlled and monitored various pieces of hardware in the experiment. This hardware

included the pressures for the Čerenkov counters, positions of the target and the calorimeter.

Chapter 3

Calibration and Monitoring

During the course of the run we periodically accepted data under special conditions which we used to calibrate and monitor the various aspects of the experiment. Subsequent analysis of these data sets not only yielded calibration parameters, but gave insight into the performance of the various detectors. In the following sections, the methods used to calibrate and monitor the different detectors in the beam line, magnetic spectrometer, and electromagnetic calorimeter are discussed and performance parameters are presented.

3.1 Beam Line

Only two aspects of our beam line were sufficiently important to worry about their precise calibration: the Čerenkov counters, and the beam stations. The Čerenkov counters were used to identify individual beam particles incident to our spectrometer and therefore had to operate at a high efficiency. We used the beam stations, in particular the beam chambers, to track the beam particles into the spectrometer, and to help locate the primary interaction vertex within our target.

3.1.1 Čerenkov Counters

We determined the pressure settings for the Čerenkov counters by first evacuating the gas chamber, then bleeding helium into the chamber until the counting rate for a given amount of beam reached a plateau. This plateau corresponded to radiation emitted from pions at 300 GeV/c and electrons at the other beam momenta used in this experiment(2, 4, 6, 30, 60, and 100 GeV/c). Under normal data taking conditions (300 GeV/c beam) the pressures were set to 1.8 psi in each gas chamber.

The Čerenkov counter pressures were observed to be stable over periods of several days, nevertheless the pressures were routinely recorded and adjusted, if necessary, every eight hours.

The performance of the Čerenkov counters was determined and monitored by examining the efficiency of each counter. The Čerenkov counter efficiency is defined

$$\epsilon_{C1} = \frac{C1 \cdot C2 \cdot BEAMV}{C2 \cdot BEAMV}, \quad \epsilon_{C2} = \frac{C1 \cdot C2 \cdot BEAMV}{C1 \cdot BEAMV}, \quad (3.1)$$

where C1, C2, and BEAMV are scaled quantities from the beam logic defined in the previous chapter. Figure 3.1 shows the Čerenkov counter efficiencies during the run.

3.1.2 Beam Chambers

The data for the beam alignment consisted of BEAMV triggers taken with the target out of the beam. Tracks were reconstructed with the algorithm outlined in chapter 4. Offsets were calculated to center the peak of the

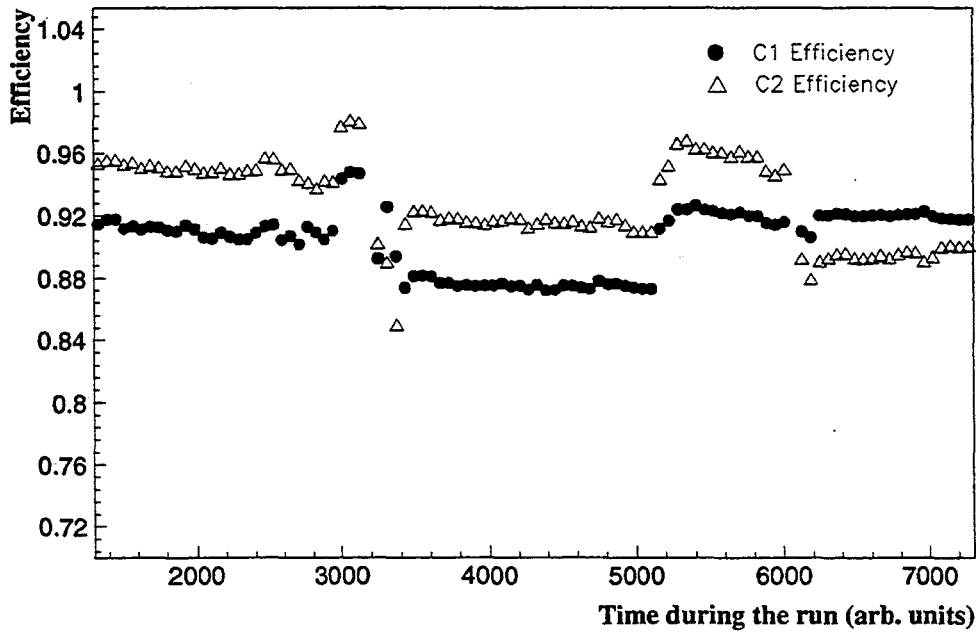


Figure 3.1: Čerenkov counter efficiencies for the E705 running period.

position residual distribution for each plane (ie. $x_{hit} - x_{track}$) of the beam chambers and BY counters. This process was repeated until the offsets converged. The PCBs were also included in this procedure, but were at positions fixed by the spectrometer alignment. The width of the residual distributions from the final iteration of the alignment gave the position resolution for each plane of the BCs.

Two methods were used to monitor and document the performance of the beam chambers. The first method used events collected from the online event pools to produce wire hit profiles and plane multiplicity distributions. This method was used to diagnose immediate problems with the electronics

Table 3.1: Average beam chamber resolutions and efficiencies.

Chamber	Avg. Resolution (μm)	Average Efficiency		
		y	u	v
BC1	230 ± 10	0.88	0.84	0.93
BC2	280 ± 10	0.89	0.87	0.93
BC3	220 ± 10	0.93	0.92	0.90

or in the chambers. The second method calculated the efficiencies of the individual chamber planes at various points in the run and was used to determine the final performance of the chambers.

The BC plane efficiencies were calculated as the fraction of registered hits for the tracks found passing through a particular plane. A summary of the BC resolutions and efficiencies is found in table 3.1. The reader is referred to reference [28] for details on the beam alignment procedure, resolutions and efficiencies.

3.2 Magnetic Spectrometer

Unlike the beam line, several aspects of the magnetic spectrometer had to be precisely calibrated and aligned to achieve optimum performance from the detectors. The various devices calibrated included the analysis magnet, Rosie, the drift and proportional chambers, and selected scintillation hodoscopes used for tracking and muon identification.

3.2.1 Analysis Magnet (Rosie)

The calibration of Rosie consisted of measuring all three components of its magnetic field at operating current (2100 A) using three mutually perpendicular Hall effect probes. These measurements were conducted over a quadrant of the magnetic aperture at approximately 1 cm intervals. Symmetry properties were used to deduce the magnetic field in the other three quadrants.

A single Hall effect probe measured the field in the center of the magnet aperture and was recorded every eight hours.

3.2.2 Drift and Proportional Chambers

Drift Chamber Calibration

The calibration of the drift chambers had to account for two effects: the individual time offsets imposed by the electronics, delay lines, etc. and the nonuniform drift velocity due to the $1/r$ nature of the electric potential near the sense wire. Time offsets were determined from the cut off points in histograms of the time distributions for every wire in each drift chamber. A drift distance function was determined by fitting the drift time distribution for each plane to a fifth order polynomial and assuming that the real drift distance distribution was flat over the half width of the drift cell. The final drift distance for a single wire takes on the form:

$$d = \frac{W}{2} \frac{F_p(t_0 - t_1)}{F_p(t_0 - t_{full})}, \quad (3.2)$$

where d is the drift distance, $W/2$ the half cell width, t_0 , t_1 , and t_{full} are the time offset, measured drift time, the full scale drift time, respectively, and F_p the fifth order polynomial in drift time $(t_0 - t)$ for drift chamber plane p . More details of the drift chamber calibration may be found in reference [30].

Chamber Alignment and Performance

All the wire chambers were aligned at the same time from data sets which consisted of INTERACTION triggers taken with a tungsten target and Rosie turned off. This setup guaranteed straight line tracks through the spectrometer and simplified the alignment procedure.

The alignment program[31] reconstructed tracks first in the individual x , u , and v views and combined the two-dimensional projection into three-dimensional lines. Then the hits for a single chamber were removed, the line was refit and residuals were recalculated from the hits near where the refit line passed through the chamber. From these residuals x , u , v , and z offsets and a rotation angle about the beam axis were calculated for that chamber. Once the new position and orientation for all the chambers was determined, the program was rerun. To ensure the convergence of the offsets and rotation, DC2X was assumed to be in its nominal position and orientation. This view was chosen because DC2 was never removed once it was surveyed in place.

The performance of the chambers was determined and monitored using similar methods as that used for the beam chambers. A summary of the average wire chamber resolutions and efficiencies is found in table 3.2.

Table 3.2: Proportional and drift chamber efficiencies.

Chamber	Avg. Resolution (μm)	Average Efficiency			
		x	x'	u	v
PC1	660 ± 50	0.84	0.69	0.73	0.79
PC2	670 ± 40	0.82	–	0.81	0.91
PC3	740 ± 40	0.87	–	0.80	0.77
DC1	420 ± 40	0.90	–	0.87	0.89
DC2	390 ± 10	0.93	–	0.89	0.89
DC3	360 ± 20	0.93	–	0.93	0.91
DC4	660 ± 40	0.89	0.88	0.85	0.85
DC5	480 ± 70	0.93	0.91	0.87	0.90
DC6	660 ± 80	0.90	0.85	0.85	0.85

3.2.3 Scintillation Hodoscopes

The scintillation hodoscopes were aligned using tracks reconstructed in normal, data triggers. Once again, x and y offsets were determined which centered the position residual distributions.

The monitoring procedures for the CPH and muon hodoscopes was similar to that of the beam chambers. Hit profiles and multiplicities were routinely recorded online, while counter efficiencies were determined by subsequent offline programs. The data in the efficiency determination came from normal running conditions. Tracks were reconstructed and the efficiency of a hodoscope plane was found as the fraction of hodoscope hits for each track pointing at a hodoscope element within tolerances. The tolerances were adjusted in the muon hodoscopes to account for multiple scattering in the muon shields. Trigger biases were avoided by using only photon triggers for the

muon counter efficiencies. Details concerning the CPH and muon hodoscope efficiencies may be found in references [32] and [28], respectively.

3.3 Calorimeter

The electromagnetic calorimeter also needed to be calibrated and aligned, but this device consisted many different detectors, namely the LGC, Active Converter, GTH and Main Array. Although each device was aligned separately, because of their interdependence, we calibrated the calorimeter as a whole. The methods used in the calibration and subsequent alignment are outlined below.

3.3.1 Online Gain Setting

The first step in the calorimeter calibration process was the setting of the Main Array block gains. Each main array block was centered in a normally incident, 30 GeV electron beam. The high voltage of each block was then set to give 10%, 12.5% and 25% of the full scale ADC value for the target small-SCG1-C, large-SCG1-C, and SF5 blocks, respectively. These settings corresponded to 250, 200, and 100 GeV full scale block depositions and were based on studies using EGS simulations of electromagnetic showers in the calorimeter. Since Rosie was turned off during calibration, the LED pulser was used to adjust the photomultiplier high voltages to maintain their gains during normal, Rosie on, data taking.

3.3.2 Offline Energy Calibration and Resolution

The beams used for the offline calibration consisted of normally incident monoenergetic electrons at nominal energies of 2, 6, 10, 30, 60 and 100 GeV. To ensure a clean sample of electrons we triggered on "PION" in the beam definition logic at typical rates of 2–3 kHz. For the 100 GeV beams the Čerenkov pressures were lowered to trigger on electrons only. The beam energy was determined immediately before and after a calibration run by directing the beam into the live regions of the proportional chambers, using PW8H1 and PW8H2, and measuring the particle's deflection in Rosie.

The calibration data sets consisted of at least a thousand electron showers in each main array block. We positioned the table to center even or odd numbered active converter blocks into the beam depending on whether the main array block behind it was in an even or odd numbered row. Outside the active converter region the table was positioned to center on a main array block. A calibration data set then was made up of eight 6250 bpi tapes and was subsequently reduced to a more manageable size for the calibration program.

Calibration Method

The energy calibration program [33] used an iterative procedure in which, if E_{Beam} denotes the beam (calibration) energy and E_T is the total recon-

structed shower energy, the width of the energy residual,

$$R_M^2 = \sum_n^{\text{events}} (E_{\text{beam}} - E_{T,n})^2. \quad (3.3)$$

was minimized for each targeted main array block. The sum in the previous equation is over events, n , in which main array block M was placed in the beam.

The reconstructed energy, $E_{T,n}$, has contributions from both the Main Array and Active Plane and includes a z shower depth correction due to the attenuation of light in the Main Array blocks. The total shower energy is initially parameterized as

$$E_{T,n} = E_{A,n} + (1 + \zeta_M/z_n)E_{M,n}, \quad (3.4)$$

where $E_{A,n}$ and $E_{M,n}$ are the measured Active Plane and Main Array shower energies, respectively. However, the only measurement of the longitudinal development of the shower is in the ratio of the measured Active Plane and Main Array energies ($E_{A,n}/E_{M,n}$). Using this measurement to approximate the $1/z$ depth dependence of the shower maximum and collecting terms one gets

$$E_{T,n} = f_M E_{A,n} + E_{M,n}. \quad (3.5)$$

Electromagnetic showers, in the energy range of interest to this experiment, are not contained in a single detector element in either the Active Plane or Main Array. Therefore, the Main Array contribution to the recon-

structured shower energy is given by

$$E_{M,n} = G_M P_{M,n} + \sum_i^{MA} (E_{i,n}), \quad (3.6)$$

where G_M and $P_{M,n}$ are the gain and pulse height of the target block. The sum is over the main array blocks surrounding the target block, typically the eight neighbors in a nine (3×3) block pattern, and gains used to arrive at the $E_{i,n}$ were those from the previous iteration in the calibration program. The Active Plane contribution to the energy in equation 3.5 has two possibilities depending on which device was in the beam. When the LGC is in the beam, we have

$$E_{A,n} = G_{M,q} \sum_{j=1}^{9-tubes} (P_{j,n}), \quad (3.7)$$

where $G_{M,q}$ is the gain in quadrant q of the LGC x tubes and the sum is over the pulse heights of the peak tube and four neighbors on each side corrected for tube-to-tube variation. The tube-to-tube gain variation was determined by fitting a spline curve to the pulse height distribution in normal data and normalizing the measured tube pulse heights to this curve. When an active converter block was in the beam, the Active Plane contribution to the energy is given by:

$$E_{A,n} = G'_{M,a} P_{a,n} + \sum_j^{AC} (E_{a,j,n}) + G'_{M,b} P_{b,n} + \sum_k^{BC} (E_{b,j,n}) \quad (3.8)$$

with $G'_{M,a}$, $G'_{M,b}$, $P_{a,n}$ and $P_{b,n}$ are the effective gains and pulse heights of the front (a) and back (b) converters, respectively. The sums combine the energies of the active converter blocks touching those in the beam and is

typically two (one block each side of the block in the beam) except for the $y = 0$ row of main array blocks in which case the sum was over four blocks (in this case two blocks were centered in the beam, one top, one bottom and each had two neighbors). The gains that give rise to the energies in the sums in equation 3.8 were from the previous iteration in the program.

The active converter blocks also manifested light attenuation along their length [20]. This attenuation is parameterized in terms of the previously determined gains as

$$G'_{M,a} = G_a(y_M + 10)^{c_a}, \quad (3.9)$$

where y_M is the distance from the shower center to the phototube, G_a and c_a are gain and attenuation exponent parameters for each active converter block.

Determining both the z correction factor and the active plane gains required additional information. Therefore, the average active plane energy depositions in each device were set to averages from predictions based on an EGS simulation of calibration electron showers.

For the 30 GeV calibration, all gains and attenuation parameters were determined for each main array and active converter block and for each LGC quadrant. At energies away from 30 GeV, typically 6, 10, and, 60 GeV, only the gains for each element were determined and any variation of the gains was attributed to an energy dependence in the average z position of the shower maximum energy deposition and was parameterized as

$$E_T = \alpha E_M + \beta f_M E_A. \quad (3.10)$$

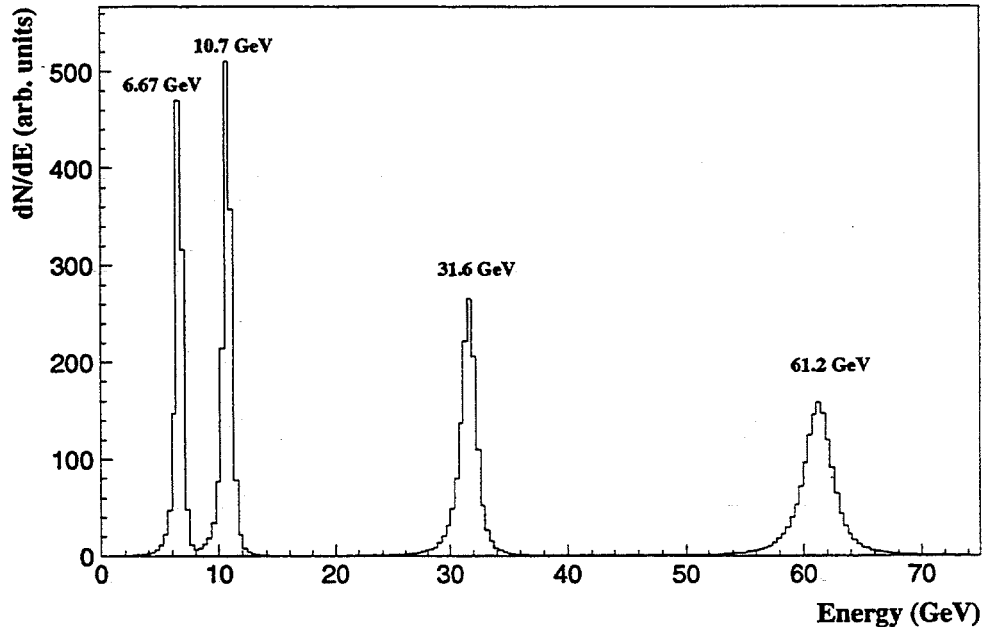


Figure 3.2: Calibration reconstructed energy distributions.

At higher energies electromagnetic showers tend to penetrate farther into the glass and hence give a larger average z depth for the shower maximum. The parameters α and β are unity for 30 GeV showers and are slow functions of energy.

Energy Resolution

The energy resolutions for each of the beam energies was determined using the reconstruction algorithm presented in chapter 4. Figure 3.3 shows the reconstructed energy distributions for the nominal 6, 10, 30, and 60 GeV electron beams, with the results of Gaussian fits to these distributions pre-

Table 3.3: Measured energy resolutions from calibration.

Region	Resolution (GeV)			
	6.67 GeV	10.8 GeV	31.7 GeV	61.4 GeV
S-SCG	0.442 ± 0.007	0.542 ± 0.010	1.161 ± 0.020	2.100 ± 0.044
L-SCG(LGC)	0.399 ± 0.010	0.498 ± 0.010	0.879 ± 0.016	1.512 ± 0.027
L-SCG(AC)	0.188 ± 0.004	0.253 ± 0.005	0.549 ± 0.011	1.028 ± 0.027
SF5	0.198 ± 0.002	0.255 ± 0.001	0.433 ± 0.004	0.775 ± 0.007

Table 3.4: Calibration resolution fit parameters by calorimeter region.

Region	a (%)	b (% GeV ^{1/2})
S-SCG	1.71 ± 0.10	11.83 ± 0.43
L-SCG(LGC)	0.700 ± 0.082	12.83 ± 0.43
L-SCG(AC)	0.990 ± 0.056	4.58 ± 0.22
SF5	0.331 ± 0.018	6.648 ± 0.075

sented in table 3.3.

Because of the statistical nature of electromagnetic showers, the energy resolution for an electromagnetic calorimeter is usually parameterized in the form

$$\frac{\sigma}{E} = a + \frac{b}{\sqrt{E}}. \quad (3.11)$$

The parameters a and b were determined by fitting the data in table 3.3 to a straight line in $1/\sqrt{E}$ and are summarized in table 3.4 and shown graphically in figure 3.3 for four separate regions of our calorimeter.

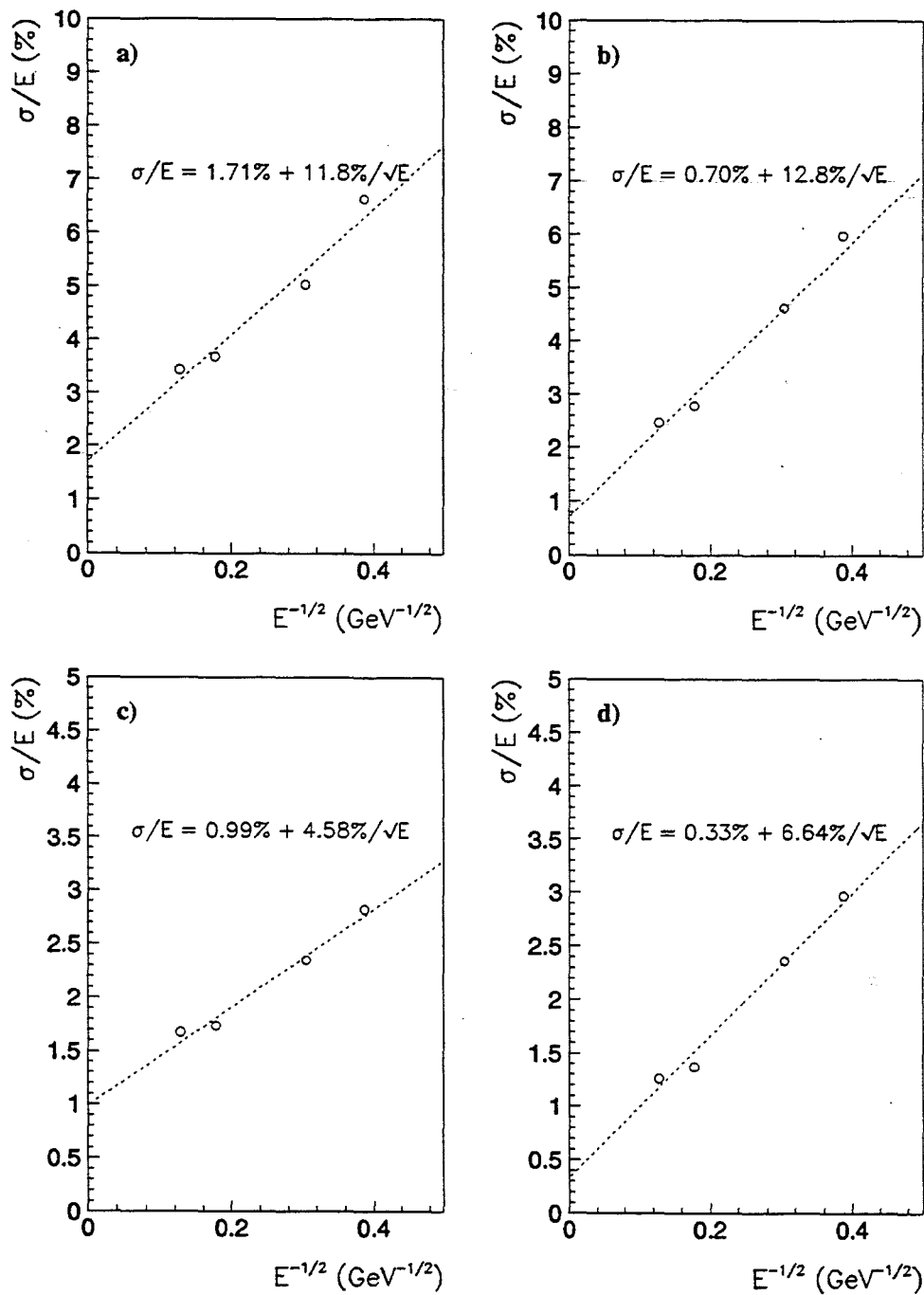


Figure 3.3: Calorimeter energy resolution in the four detector regions: a) small SCG, b) large SCG(LGC), c) large SCG(AC), d) SF5.

3.3.3 Gain and Pedestal Monitoring

The pedestals and gains for the calorimeter glass were monitored and updated using data from LED triggers taken out of spill. The neutral density filter cycled between 0% transmission and 100% transmission every nine minutes during normal data collection. Pedestals and gain corrections were determined for each block by averaging the ADC values for ≈ 100 LED triggers with the filter set to 0% and 100%, respectively. These averages were stored in a large data base. The corrected gain is then given by

$$G_{data} = G_{calib} \frac{\langle ADC \rangle_{calib}}{\langle ADC \rangle_{data}} PIN \quad (3.12)$$

with PIN given by the ratio of the ADC values for a PIN diode in the data to the value at calibration averaged over the three diodes. This later term was used to correct for the change in light output of the LEDs.

3.3.4 Dynamic Pedestal

Most LED data was taken out-of-spill and consequently only monitored the raw gains and pedestals for the calorimeter glass. To study systematics of the pedestals and gains under the same conditions as normal data we accepted LED triggers in-spill for a small portion of our data. Subsequent analysis of these data lead to the discovery of a pedestal shift which was determined to be proportional to the instantaneous power deposited by electromagnetic and hadronic showers in a particular block [22]. The proportionality constant differed depending on the different type of glass, SCG1-C scintillation glass and SF5 lead glass.

If one assumes that the average power in a block is proportional to the average energy deposited in that block. The energy shift due to this pedestal for a single main array block can then be parameterized in terms of the average pedestal shift, $\langle E_{ped} \rangle_0$, and average interaction rate, R_0 , from the in-spill data, as

$$E_{shift} = \langle E_{ped} \rangle_0 + k(\langle E \rangle_0 R_0 - \langle E \rangle R), \quad (3.13)$$

where $\langle E \rangle$ and R are the average deposited energy and interaction rate in the data for any time in the run, respectively. The term in parantheses is then just the difference between the power deposited during the in-spill data and data taken at any other time during the run. The values of $\langle E \rangle_0$ and $\langle E \rangle$ were determined for minimum bias triggers in the in-spill LED data and for data of different beam and magnet polarity combinations. A linear relationship was found between the *BEFORE* energy, E_B , and the interaction rate. The *BEFORE* energy is defined as

$$E_B = \sum_i^{MA\ Blocks} G_i BEF_i, \quad (3.14)$$

where G_i is the gain and BEF_i is the ADC before value, and ADC before for main array block i . Combining the proportionality constant k from equation 3.13 with the linear dependence observed in equation 3.14 yields the dynamic pedestal which was used in the analysis:

$$E_{shift} = \langle E_{ped} \rangle_0 + \langle E \rangle_0 (A \langle E_B \rangle_0 + B) - \langle E \rangle (A E_B + B), \quad (3.15)$$

where the parameters A and B were determined from analysis of the in-spill

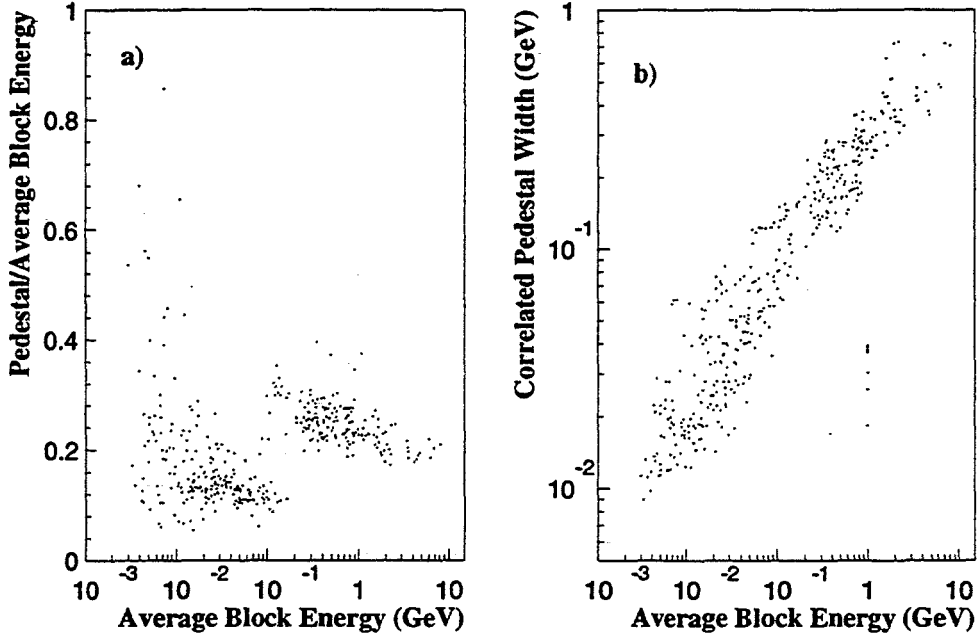


Figure 3.4: Energy fraction from the dynamic pedestal a) and correlated uncertainty b) as a function of average block energy

data. The typical size of the dynamic pedestal ranged from 2–40% of the average minimum bias block energy and is shown plotted against the average block energy in figure 3.4 a).

The uncertainty associated with the dynamic pedestal under a shower in the data was estimated by calculating a correlated pedestal width for each main array block from N in-spill events:

$$\sigma_{shower} = \sqrt{\frac{1}{N-1} \sum_{i=1}^N (\langle E_P \rangle - E_{P_i})^2}, \quad (3.16)$$

where $\langle E_P \rangle$ is the average pedestal and E_{P_i} is the event pedestal in a cluster. A cluster typically consisted of nine blocks as defined by the

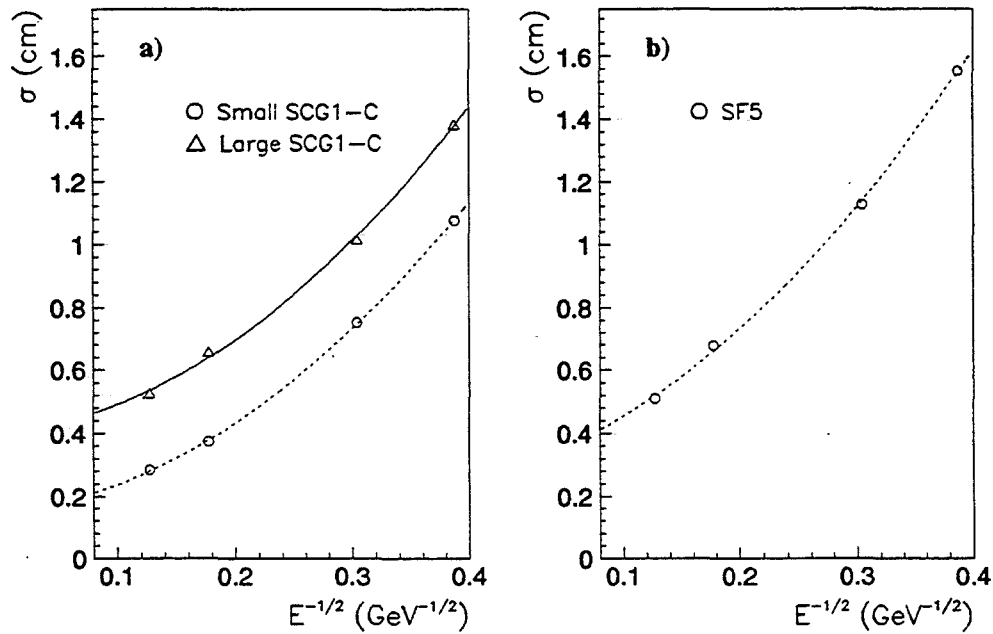


Figure 3.5: Main Array glass position residuals from calibration data: a) scintillation glass, b) lead glass. The lines represent fits to a second degree polynomial.

pattern recognition. The correlated uncertainty for a shower in any event was arrived at by scaling the in-spill result by $E_{shift}/\langle E_{Ped} \rangle_0$. The correlated uncertainty is also plotted versus average block energy in figure 3.4 b.

3.3.5 Alignment and Position Resolution

The different elements of the calorimeter were aligned relative to the beam (and hence to each other) using the same data as the energy calibration. This fixed the positions of the hodoscopes and glass to 0.5 mm and 1.1 mm, respectively. The techniques used for the position determination in each

device are discussed in chapter 4. Resolutions were also determined for each device and are summarized in figures 3.5 and 3.6.

The calorimeter alignment was also monitored and adjusted when necessary using the charge track information from electrons reconstructed in the data. Chapter 4 contains a discussion of electron reconstruction.

3.3.6 Time Calibration and Resolution

The time calibration of the Main Array glass proceeded in a manner similar to the energy calibration. Normally incident, monoenergetic electrons were used to produce showers in the Main Array with the data coming from the time measurements of the blocks participating in the shower. Because the START signal for each TDC was derived from a discriminated pulse from the ADC module, the timing displayed a pulse height dependence (see figure 3.7). Therefore, several energies of electron showers were used for a single calibration. These energies were typically 6, 10, 30, and 60 GeV. All of the showers for every energy setting were condensed into a single file which contained only the the original data tape numbers, calorimeter table positions, and pulse height and time information for each block participating in the showers.

The pulse height dependence was observed to follow the functional form:

$$t_{fit} = A \log(ADC - ADC_0) + t_0, \quad (3.17)$$

where ADC is the pedestal subtracted ADC counts and A , ADC_0 and t_0 are parameters determined by minimizing the width of the time residual

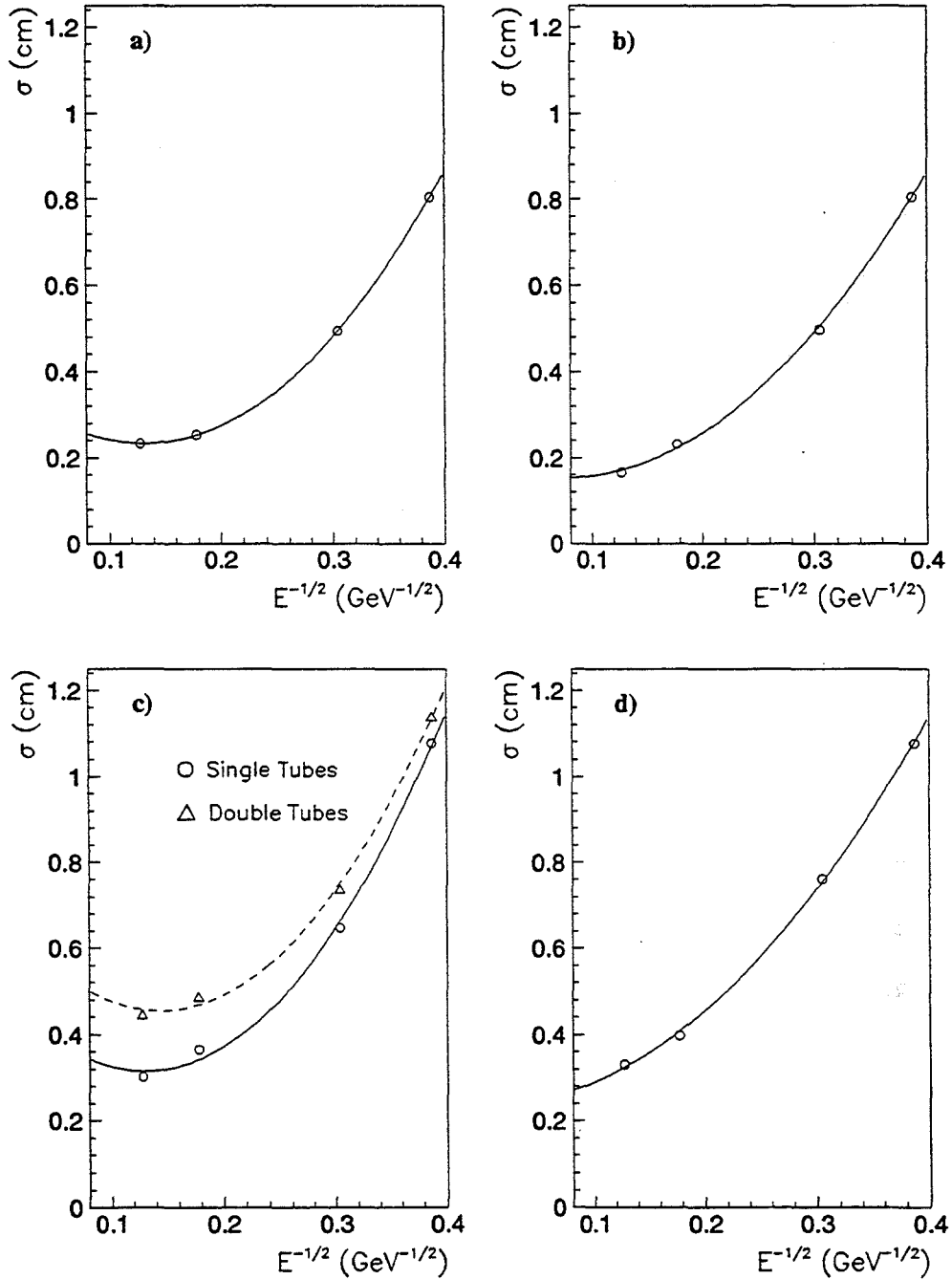


Figure 3.6: Hodoscopes position residuals from calibration data: a) LGC x, b) LGC y, c) GTH x, d) GTH y. The lines represent fits to a second degree polynomial.

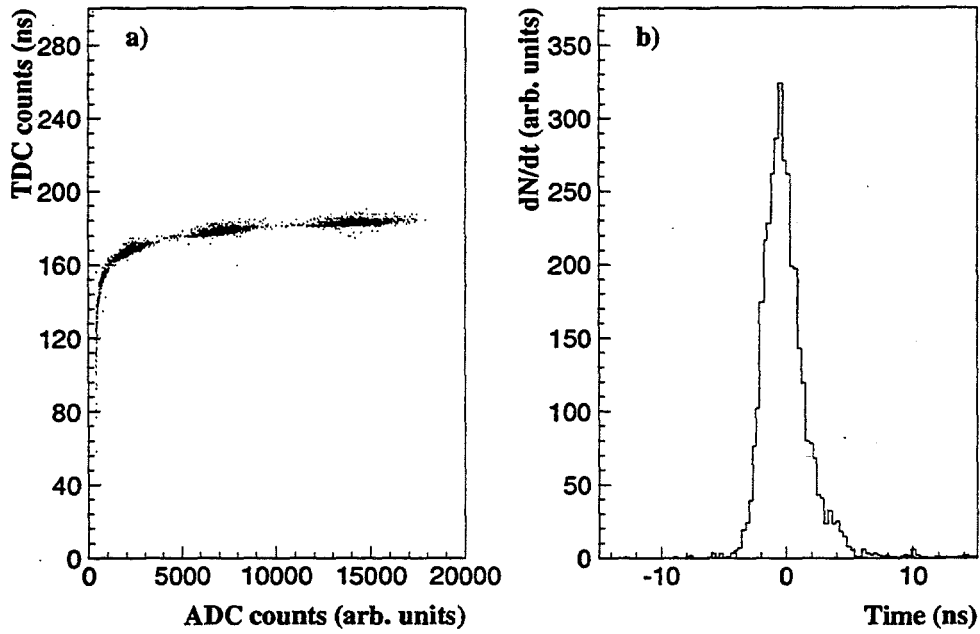


Figure 3.7: Timing for block 147; a) Time vs pedestal subtracted ADC counts, and b) time resolution.

distribution ($t_{measured} - t_{fit}$).

Several blocks had the low pulse height part of their time vs ADC distribution cut off. This phenomenon was due to interaction of the discriminator with induced noise on the ADC output signal from the BEFORE (TDC stop) signal above the pick-off discriminator threshold*. The artificial, high thresholds corresponded to block energies in the range 6–12 GeV, whereas the discriminator threshold corresponded to a 2–3 GeV deposition per block. There were two solutions to this problem that didn't require major modifi-

*Each TDC pick-off module had one common threshold for its 16 channels.

Table 3.5: Time resolution of the Main Array glass by block type.

Calibration		Resolution (ns)				
Date	Energies (GeV)	Sm-SCG1C	Lg-SCG1C	SF5	Over All	
Aug. '87	6,10,30,60	1.467	2.090	1.895	1.886	
Nov. '87	6,10,30,60	1.321	1.600	1.550	1.519	
Feb. '88	10,30,60	1.392	1.723	1.613	1.563	

cations to the ADC electronics: lengthening the minimum width of the time over threshold in the discriminator circuit or raising the discriminator threshold. The former solution effectively deadened all the channels in a pickoff module for long periods of time (≈ 400 ns); obviously an unacceptable solution. The later solution raised all the thresholds in the pickoff module to that of the worst channel. This was also unacceptable, since many modules had only a few channels with this problem and it degraded the TDC efficiency near the higher discriminator threshold.

In order to account for timing changes on a channel by channel basis, due to drifts in pick-off thresholds, high voltages, etc., a simple system of measuring offset times was used. Data was taken, both at calibration and during normal data runs using the LED pulser with the filter set to 100% transmission. The ADC dependence of the timing with this filter setting could be approximated by a constant. A time offset (t_{off}) was calculated by subtracting the pulser times at calibration from those during data runs.

In subsequent analysis, a deposit time relative to the triggered interaction

was assigned to each block according to

$$t_{deposit} = t_{measured} - t_{fit} + t_{off} \quad (3.18)$$

and was used to reject out of time electromagnetic showers.

Chapter 4

Event Reconstruction

Once the individual devices in the experiment were calibrated one could begin reconstructing events from the information in the detectors. This included charged particle trajectories through the spectrometer, their momentum, energy and possibly their type (mass). Also the identification and reconstruction of photons. In the following sections the algorithms for determining charged particle trajectories and momenta is outlined and the electromagnetic shower reconstruction is presented in detail. The detector reconstruction is followed by a discussion of the momentum and energy determination, and identification of selected particles.

4.1 Track Reconstruction

The charged particle reconstruction used three different algorithms to determine the trajectories from the tracks (hits in the wire chambers) of charged particles as they passed through the spectrometer. Each of the different algorithms corresponded to a different region of the spectrometer and were referred to as the beam, upstream and downstream regions. The beam tracking reconstructed charged particle tracks into the ${}^7\text{Li}$ target, whereas the upstream and downstream tracking reconstructed the trajectories of charged

particles between the target and Rosie and between Rosie and the electromagnetic calorimeter, respectively.

4.1.1 Beam Tracking

The algorithm to find the beam particle trajectory into the target only used the wire hit information from the beam chambers. First, spacial points were located by finding common three wire and two wire crossings (triples and doubles) in the three beam chambers. For each pair of spatial points in BC1 and BC3, a road was defined and all hits in BC2 were recorded yielding three point tracks. At this point hits may be used by more than one track. Each track was fit to a straight line and the tracks were ordered by increasing chi squared. If one track shared a hit with another the track with the lowest chi squared was kept. No more than five beam tracks were kept in any case. Reference [28] contains a more detailed description of the beam tracking algorithm.

4.1.2 Upstream Tracking

The upstream tracking used the hit information from the proportional chambers and the time information from the upstream drift chambers (DC1-3) to reconstruct three dimensional lines from the target to the magnet aperture. Rather than use spatial points from the wire triples or doubles in each chamber as the beam tracking, the upstream tracking algorithm first reconstructed tracks in two-dimensional views (xz , uz and vz planes) then combined these *view tracks* into three dimensional tracks (spatial lines).

A two-dimensional track was found by forming a line from a hit in each of two *seed planes*. Both of the ambiguities were used for hits from drift chamber seed planes.* If the line was in the acceptance of the spectrometer (pointed from the target into the magnet) a list of chamber hits was created containing the two seed hits. The line was then projected into other planes, for that view, and the nearest hit within tolerances was added to the list. Lines with at least four hits were considered 2-D track candidates and were fit to a straight line. All possible seed plane combinations were used to find the maximum number of track candidates possible. Each candidate was compared with others for duplication with the version having the largest chi squared-per-degree-of-freedom (χ^2/DOF) removed. The remaining candidates were stored as a list of view tracks with each view treated alike.

Three-dimensional tracks were made by calculating the xz and yz slopes and intercepts using the uz and vz view tracks. If the 3-D track candidate passed acceptance cuts and had more than four hits, its xz slope and intercept was compared with the slopes and intercepts from the xz view tracks. Matches had a χ^2/DOF calculated and was checked against other tracks for duplicates. Duplicated tracks were treated in the same manner as the view tracking. The hits on the found 3-D track were then fit to a spatial line. Remaining two-dimensional tracks were then reprocessed through this algorithm ultimately producing a list of three dimensional, upstream tracks.

*Because the information obtained from the drift chambers is a distance from the sense wire, one doesn't know, a priori, which side of the wire the charged particle passed. This is often referred to as the *right/left ambiguity* independent of view.

4.1.3 Interaction Vertex Determination

The interaction vertex was determined using one of two methods depending on whether a beam track could be associated with the upstream tracks. The association of a beam track with upstream tracks was performed by stepping each beam track through the target and calculating the number of upstream tracks within a circle of radius three times the combined uncertainty in the beam track and upstream track positions. The beam track with the maximum number of associated upstream tracks greater than three was used to determine the interaction vertex.

For the case of associated beam and upstream tracks, the z position of the vertex was determined by minimizing the chi squared:

$$\chi^2 = \sum_{i=1}^{N_{tracks}} \frac{(x_i - x_b)^2}{\sigma_{x_i}^2 + \sigma_{x_b}^2} + \frac{(y_i - y_b)^2}{\sigma_{y_i}^2 + \sigma_{y_b}^2}, \quad (4.1)$$

where (x_i, y_i) and (x_b, y_b) are the positions of the i th upstream track and beam track at the z position of the vertex and σ_{x_i} , σ_{y_i} , σ_{x_b} , and σ_{y_b} are the x , y , upstream and beam track uncertainties, respectively. The sum in equation 4.1 is over all upstream tracks that satisfy the combined uncertainty discussed in the previous paragraph. The x and y position of the vertex was then given by the beam track at the z position as determined above.

When beam track information was not available, or all the beam tracks were associated with less than three upstream tracks, the vertex was determined by the upstream tracks alone by minimizing the chi squared for the

vertex position:

$$\chi^2 = \sum_{i=1}^{N_{tracks}} \frac{(a_{x_i} z_v + b_{x_i} - x_v)^2}{\sigma_{x_i}^2} + \frac{(a_{y_i} z_v + b_{y_i} - y_v)^2}{\sigma_{y_i}^2}, \quad (4.2)$$

where (x_v, y_v, z_v) is the vertex position and a_{x_i} , a_{y_i} , b_{x_i} , and b_{y_i} are the i th x and y upstream track slopes and intercepts, respectively. This procedure was repeated with the upstream tracks contributing seventy or more to the chi squared rejected as not associated with the vertex. The vertex resolution using these methods was determined to be 0.1 cm, in the x and y and 5 cm in the z directions[28].

4.1.4 Downstream Tracking

The downstream track reconstruction algorithm used the timing information from the downstream drift chambers (DC4–6) and the hit information from the CPH and muon counters to reconstruct three dimensional lines from the magnet aperture through the rest of the spectrometer. The algorithm first found two dimensional, view tracks in the xz plane and combined the x hit information from the found 2-D tracks with the u and v hits to locate 2-D tracks in the yz plane. The xz and yz two dimensional tracks were then combined into 3-D tracks.

The xz view track finding used a similar seed plane algorithm as that used to find upstream view tracks. The line projected from the hits in the seed planes had to originate in the magnet aperture and fall within the spectrometer's angular acceptance. The additional requirement that the line pass through either a hit CPX counter or a muon counter helped to eliminate

potential track candidates that were out-of-time with the triggered event. Lines with at least four hits and one hit occurring in each drift chamber became track candidates and were fit to a straight line. All possible seed plane combinations were used to achieve the largest number of track candidates. Each candidate was checked against the others for duplicates. Duplicated tracks were removed based on χ^2/DOF in the same manner discussed in the section on upstream tracking above. All remaining candidates were stored as in a list of xz , view tracks.

The y tracking used the hits on the xz tracks, previously found, and combined them with the hits in the u and v planes to produce a list of effective “ y hits”. These “ y hits” were then used to find tracks again using the seed plane technique as described above. Successful yz track candidates had to originate in Rosie’s aperture, have a yz slope consistent with the spectrometer’s angular acceptance, point to a hit CPY or MUY counter and contain at least two “ y hits”. A list of yz , view tracks resulted by removing duplicated candidates.

The xz and yz downstream view tracks were combined into three dimensional lines. We then fit the hits associated with each of these lines to produce a list of 3-D, downstream tracks.

4.1.5 Momentum Determination

Once upstream and downstream track segments were determined, they were paired with each other in order to measure the momentum of the particle

that produced the track. The matching required that the yz upstream and downstream slopes nearly agree and that their projected (x, y) position at $z = z_{match}$ agree within tolerances, where z_{match} is defined in terms of Rosie's magnetic field, B :

$$\int_{-\infty}^{z_{match}} B \cdot dz = \frac{1}{2} \int_{-\infty}^{\infty} B \cdot dz. \quad (4.3)$$

Given Rosie's geometry and current settings z_{match} was determined to be -4.8 cm in the experiment coordinate system. If no upstream segment was found for a downstream segment, a line was projected between the downstream (x, y) intercept and the vertex position and an attempt was made to find an upstream track along this line. If a track was found it was tagged as *matched* and the upstream segment found added to the upstream track list. If no upstream track was found, the projected upstream line was called a pseudo-upstream segment, added to the list of upstream tracks and the track was tagged as *unmatched*.

The momentum of a charged particle was then determined by measuring x deflection between the upstream and downstream tracks in the magnet. Using a box field approximation (the field is uniform and constant inside the box and zero outside) and the xz and yz slopes from the upstream tracking, m_{xz} and m_{yz} , the total particle momentum is given by

$$p_{total} = \frac{p_{T_{kick}} \cos \theta_{in} \sqrt{1 + m_{xz}^2 + m_{yz}^2}}{\sin \theta_{xin} - \sin \theta_{xout}}, \quad (4.4)$$

where θ_{in} , θ_{out} and $p_{T_{kick}}$ are the angles, in the xz plane, between the upstream, downstream tracks and the beam and an effective transverse momen-

tum “kick” given by the Rosie. The components of the particle’s momentum are then given by

$$\begin{aligned}
 p_x &= \frac{m_{xz} p_{total}}{\sqrt{1 + m_{xz}^2 + m_{yz}^2}} \\
 p_y &= \frac{m_{yz} p_{total}}{\sqrt{1 + m_{xz}^2 + m_{yz}^2}} \\
 p_z &= \frac{p_{total}}{\sqrt{1 + m_{xz}^2 + m_{yz}^2}}.
 \end{aligned}
 \tag{4.5}$$

Once all the charged particle tracks for an event were found analysis of these particles could be performed. This was in the case of with dimuon triggers (see chapter 5). However, whether they were analyzed or not, the charged tracks were attached to the end of the event in a “pseudo-channel” for subsequent analysis after the electromagnetic reconstruction could be performed.

4.1.6 Momentum Resolution and Efficiency

The track momentum resolution and reconstruction efficiency were both determined using the Monte Carlo technique described in chapter 5. The momentum resolution is usually parameterized as a fractional uncertainty (σ_p/p) and was found to follow the empirical form

$$\sigma_p/p = 0.2 + 0.02p + 0.001p^2,
 \tag{4.6}$$

where σ_p/p is in percent and the momentum (p) is measured in GeV/c. The reconstruction efficiency was found to be $78 \pm 1\%$ [28].

More information may be found regarding the track reconstruction program in references [28, 29, 30].

4.2 Electromagnetic Reconstruction

The electromagnetic reconstruction was a FORTRAN program, MAINEMD, which used an iterative procedure to determine both the positions and energies of showers in the calorimeter. The program also identified these showers as either electromagnetic or hadronic. This reconstruction process began once an event was read into the program and the detectors making up the calorimeter and the charged particle tracks were decoded. The detectors involved in the reconstruction include the LGC, GTH, the Active Converter and Main Array glass blocks. For the remainder of this chapter, the LGC and GTH will be, collectively, referred to as *the hodoscopes*. From the Main Array block energy information, we formed *clusters* consisting of nominal three-by-three block patterns which contained a substantial deposited energy. These clusters and their parameters were placed in a list as part of a special COMMON block of shower candidates (see appendix A). A second pattern recognition was also performed which combined the charged track and hodoscope information to locate additional clusters in the Main Array and help resolve later problems associated with the x - y matching of signals in the hodoscopes.

Once an initial list of clusters was formed, we determined the position of each shower using the Main Array block energy information. The cluster block energies were then fit to an assumed electromagnetic shower shape at this position and the blocks shared between one or more other clusters had their energy partitioned. The partitioning or *sharing* of the block energy

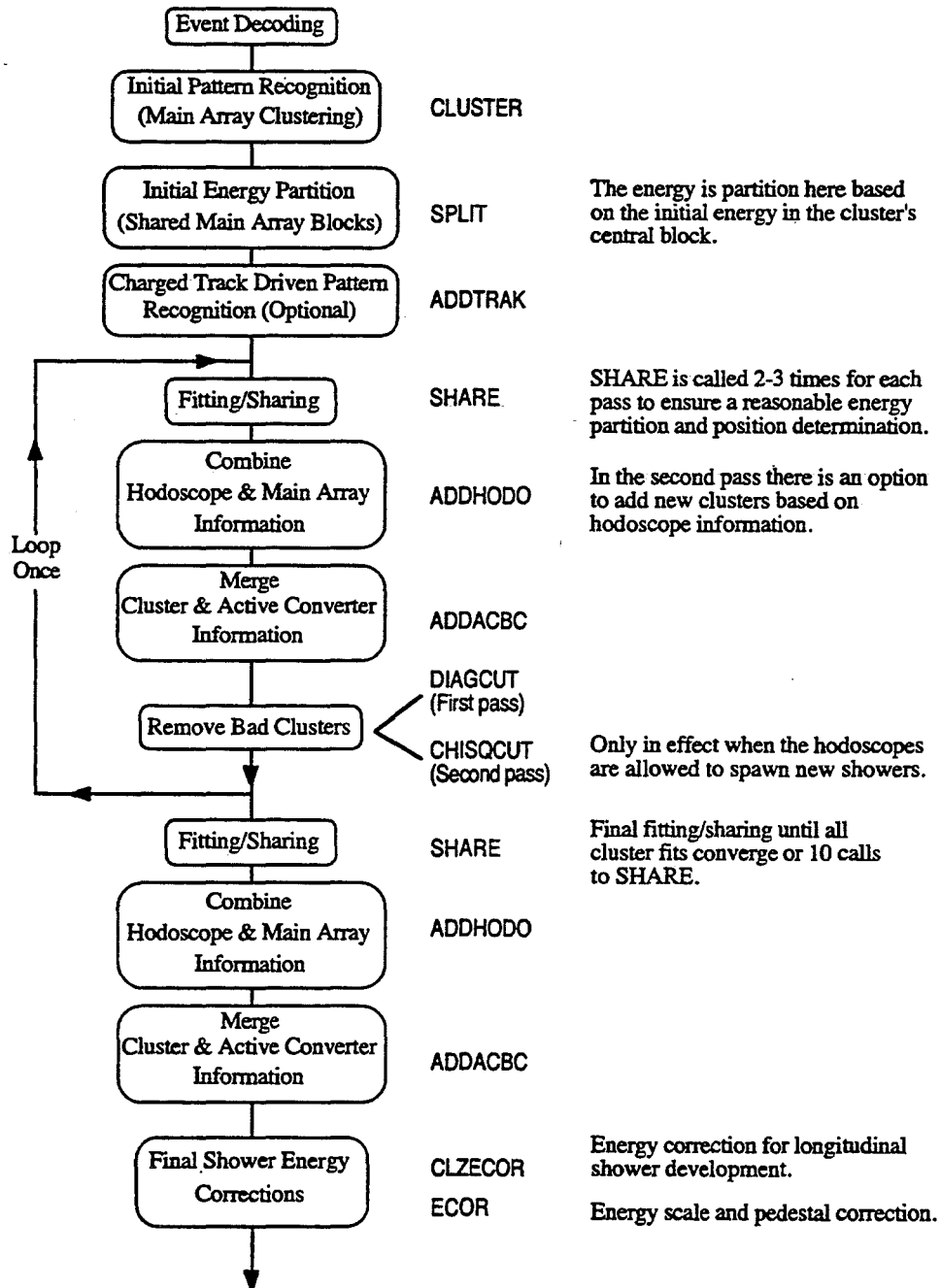


Figure 4.1: Electromagnetic reconstruction program flow diagram.

was performed in such a way as to maintain the total energy in the block and satisfy the requirements of the cluster fits as closely as possible. The position determination, fitting and sharing were run through at least twice to give more consistent results before new information was added. Better estimates of the total shower energy and position were made by combining the above Main Array information with that from the hodoscopes and Active converter. Appropriate corrections were made for the position dependence in these devices. At this point, clusters which no longer satisfied minimum requirements or had known topological defects introduced by the pattern recognition algorithms were flagged as bad and removed.

After two passes through the steps outlined above a final fit and energy partition was performed on all remaining clusters. The clusters were once again combined with the Active Converter and hodoscopes information to pick up anything missed in the previous iterations. Finally, energy corrections for the longitudinal shower development, energy scale and pedestal were made and the list of clusters was passed on to be analyzed. The separate steps outlined above were all FORTRAN subroutines called by the main program. Figure 4.1 shows a flow diagram of MAINEMD with the names of the subroutines used to the right of the box describing their function.

4.2.1 Device Decoding

Four detector systems and the charged particle track channel were decoded for the calorimeter reconstruction. However, only two ADC systems were

used to instrument these detectors thus simplifying the detector decoding. The calorimeter glass used the Fermilab precision ADCs described in chapter 2. The 16 bits of each ADC word was made up of 12 bits of the actual ADC pulse height, 3 bits giving the status of the energy in a block before the trigger and a single $\times 8$ multiplier bit to extend the dynamic range of the ADC. The energy in each Main Array block was decoded by multiplying the pedestal subtracted ADC pulse height by its gain and then subtracting off the dynamic pedestal determined as described in the previous chapter. The result was stored in the array EMA for further analysis. The Active Converter block energy could not be determined at decoding time because of the y position dependence of the block energy as given by equation 3.9. For this reason we stored the gain times the pedestal subtracted ADC count in the array EAC. The actual energy in an Active Converter block was later determined when the position of a shower was known.

Both the GTH and LGC used the LeCroy 2280 ADC system operating in the sparsified mode and subtracted pedestals on-line. For the GTH, the ADC values were multiplied by a tube-to-tube relative gain and a plane gain. The plane gains were determined at calibration and were used to ensure the x and y pulse heights from a single shower agreed with each other. The ADC values in the GTH double tube region were also divided by 2 so that a corrected ADC spectrum would be continuous across the single-double tube boundary. For simplicity in the following discussions the GTH corrected ADC values will hereafter be referred to as energies. The LGC channels were decoded

into energies in a similar manner with an additional correction applied to account for the high voltage sag when running at higher interaction rates. The correction for x dependence in the y pad energies was made later when information from the two views were matched (see section 4.2.4). All the decoded hodoscope information was stored by plane in the array ENERTB.

The charged particle track decoding used the inverse algorithm used to encode and append the information to the event and will not be described.

4.2.2 Pattern Recognition

Three types of pattern recognition were used to identify showers in the calorimeter, either electromagnetic or hadronic; each type used a different set of detectors. The first two algorithms are discussed in this section while the third is discussed in section 4.2.4.

The primary pattern recognition algorithm was driven by the energy information from the Main Array glass blocks requiring a block to contain at least 300 MeV and have more energy than its immediate x and y neighbors. Any block satisfying these criteria was called a *peak block*. Peak blocks not part of the outer edge of the Main Array became the center blocks of a clusters.

A cluster consisted of a nominal three-by-three set of Main Array glass blocks which were numbered according to the scheme in figure 4.1 a. Because the Main Array contained blocks of two different sizes, special case clusters were formed on the boundary between the different sizes of blocks. The case

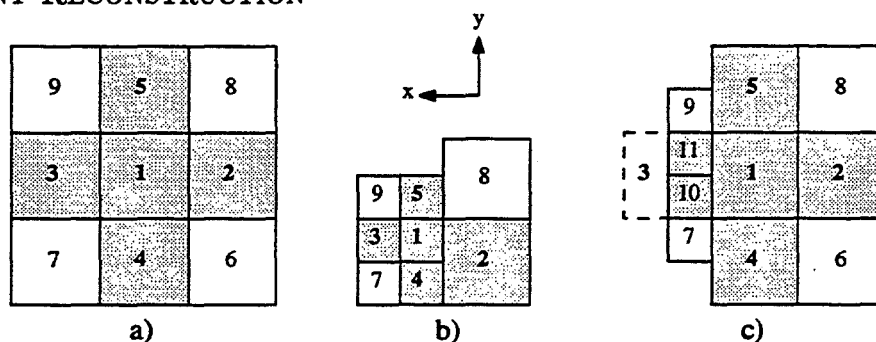


Figure 4.2: Main Array block patterns for three different cases: a) same size blocks, b) small-to-large block boundary and c) large-to-small block boundary. Shaded regions identify the blocks used in the peak finding algorithm. Blocks 10 and 11 are combined into a “virtual block” for fitting purposes.

for a small peak block neighboring a large block and a large peak block neighboring small blocks are shown in figures 4.2 b and c, respectively. To keep the numbering consistent for all clusters for fitting purposes the two small blocks next to a large block peak were combined into a *virtual block* (this feature is discussed later in the fitting section of this chapter).

The second algorithm used the downstream charged particle tracks in association with the hodoscopes to find clusters. A track was first projected into the hodoscopes and a window twice the expected x resolution by twice the expected y resolution was searched for x , y crossings. The method used to find prospective crossings is described in section 4.2.4. For the case where multiple crossings occurred in the window, the crossing closest to the track position was chosen. When a track-hodoscope crossing match was found, the track was projected onto the Main Array front face and the block hit

by the track was determined. Tracks falling within 1.0 cm of a block's edge were projected an additional 10 cm into the Main Array and the block at this x, y position was called the hit block. The cluster list was then searched for peak blocks that matched the hit block. When a match was found, the position of the shower was determined by projecting the track at the hodoscope position onto the front face of the Main Array. If no match was found a new cluster was formed and added to the list when the hit block contained at least 300 MeV raw energy (EMA) and the position was assigned as described above.

4.2.3 Shower Fitting

EGS Tables

In order to determine the positions and energies of electromagnetic showers in the calorimeter, one needs a set of known shower shapes with which to compare the data. To this end, samples of monoenergetic showers were generated using the EGS-IV electromagnetic shower simulation program with our detector geometry. The showers were generated at five different, logarithmically distributed energies, 1.00, 2.54, 6.05, 14.88, and 36.6 GeV, and three different particle types:

1. Photons entering the calorimeter as if produced in the target.
2. Electrons entering the calorimeter as if deflected in Rosie.
3. Electrons entering the calorimeter at normal incidence.

The first two particle types were used in normal data analysis while the third was used to reconstruct calibration events for test and debugging purposes. The incident angle for the deflected electrons was assumed to depend only on the electron's energy and position in the calorimeter.

To avoid position biases in the tables to be generated from these showers, one ideally would want to distribute them uniformly across the calorimeter. However, this distribution would limit the number of showers in many of our complicated boundary regions. Therefore, by using the symmetry of the Main array, one could assign each Main Array block to one of 36 regions occurring in the $x > y$ half of the first quadrant. We then populated each region uniformly with equal numbers of showers. Thus avoiding position biases and increasing the number of showers at the complicated boundaries. Showers were generated in all eight half-quadrants avoiding possible biases due to the breaking of the Main Array symmetry caused by the LGC or the electron deflection in Rosie.

These shower samples were used to parameterize functions describing the shower position and deposited energy in a Main Array block. The functions were simplified by assuming the two dimensional shower shape could be represented by uncorrelated three block x and three block y distributions. The three blocks used to represent the x and the y distributions were 1,2,3 and 1,4,5, respectively, where the numbers indicate the corresponding blocks in figure 4.2. These functions were simplified further by using the Main Array to fold the produced showers into the first quadrant for deflected electron

showers, and the $x > y$ half of the first quadrant for photon and normal incident electron showers. We avoided an enormous set of multidimensional fits to arrive at these functions by storing them in tables for specific, measurable parameters. Sample diagrams of these function may be found in reference [22]. Averaging the position projection or the normalized block energy over the number of showers of a given parameter set determined the table entries. The standard deviation was also kept as an estimated uncertainty for each table entry.

The position tables were parameterized in terms of the 3 particle types, 5 shower total energies, 8 Main Array regions, 4 longitudinal shower depths, 2 projections (x and y) and 10 values of the 3 ratios:

$$\begin{aligned} r_{12} &= \frac{E_1 - E_2}{E_1 + E_2} \\ r_{13} &= \frac{E_1 - E_3}{E_1 + E_3} \\ r_{23} &= \frac{E_2 - E_3}{E_2 + E_3} \end{aligned} \quad (4.7)$$

where E_i is the energy in block i of the cluster. The y projection of the position tables were parameterized by similar ratios with block indices 2 and 3 replace by 4 and 5, respectively. The eight detector regions corresponded to three block sets of SSS, SSL, SLL, LLL, LLP, LPP, PPP_{inner} and PPP_{outer} blocks. The letters S, L and P represent small SCG blocks, large SCG blocks and SF5 (Pb glass) blocks, respectively. The outer SF5 region corresponded to the outer five columns of blocks. The four longitudinal shower depths were distinguished by upper limits in the ratio $R_z = \frac{E_{AC}}{E_{MA}}$ and are found in

Table 4.1: R_z upper limits for the z depth index in the EGS tables.

E_{shower} (GeV)	Depth index	R_z (Upper Limit)	
		LGC Region	AC Region
1.00	1	0.238	0.296
	2	0.348	0.436
	3	0.460	0.559
	4	-	-
2.54	1	0.147	0.198
	2	0.236	0.316
	3	0.329	0.430
	4	-	-
6.05	1	0.091	0.128
	2	0.157	0.221
	3	0.227	0.315
	4	-	-
14.88	1	0.054	0.082
	2	0.100	0.151
	3	0.150	0.222
	4	-	-
36.60	1	0.032	0.049
	2	0.062	0.096
	3	0.097	0.148
	4	-	-

table 4.1.

The first five parameters of the block energy tables were the same as those used for the position tables, namely: particle type, shower energy, Main Array region, longitudinal shower depth and projection. These tables were also parameterized by 20, 1 cm projected positions relative to the center of the peak block, and 3 block numbers. The block energy functions were normalized to the total three block energy sum in the projected direction;

$$e_1 = \frac{E_1}{E_1 + E_2 + E_3}$$

$$e_2 = \frac{E_2}{E_1 + E_2 + E_3} \quad (4.8)$$

$$e_3 = \frac{E_3}{E_1 + E_2 + E_3}.$$

Again, E_i indicates the energy deposited in cluster block i and the y normalized block energies were given by replacing the appropriate block indices.

For the case of the large-small block boundary when the peak block is large (see figure 4.2 c), the two small block energies on the boundary were summed into a virtual block energy. This virtual block energy was then treated as described above when determining table entries.

Main Array Shower Position Determination

Armed with the above set of position tables and partitioned Main Array block energies, the (x, y) positions of showers could be crudely determined for real showers in calibration or data. If energy was deposited in all three blocks of an x or y projection the position and its uncertainty was determined using all three position indicators according to the prescription:

$$x = \frac{w_{1,2}r_{1,2} + w_{1,3}r_{1,3} + w_{2,3}r_{2,3}}{w_{1,2} + w_{1,3} + w_{2,3}} \quad (4.9)$$

$$\delta x = \{w_{1,2} + w_{1,3} + w_{2,3}\}^{-\frac{1}{2}}, \quad (4.10)$$

where the $x_{i,j}$ and $w_{i,j}$ are the positions and inverse variances ($\frac{1}{\sigma_{i,j}^2}$) predicted by the tables for the position estimator $r_{i,j}$. The actual position used was the result of an interpolation in energy between adjacent $r_{i,j}$ entries. For the case when no energy was deposited in one of the side blocks the position and

estimated uncertainty was determined by the table entry of a single estimator and its uncertainty. When no energy was deposited in either side block, the position was assigned to the center of the peak block and the uncertainty was assigned as half the block size.

The mean position resolution of this method was determined to vary between 0.3 and 1.5 cm for isolated showers from the electron calibrations. The glass position resolutions for various block types and calibration energies are summarized in figure 3.5 of the previous chapter.

Main Array Energy Fit

Once the shower position has been determined and projected to the Main Array front face, the partitioned block energies for a given cluster were fit to an assumed electromagnetic shower shape (see energy partitioning below). The above energy tables gave the relative energy distribution or shower shape for the five blocks in the plus shape of a nine block cluster (the shaded region in figure 4.2). To get the best estimate of the shower shape possible, an interpolation was performed between adjacent entries in both the position and energy. Since the three block patterns for the x row and y column of the plus were assumed independent, the peak block had two possible values. This degeneracy was removed by scaling the three block y shape so that the energy proportion of block one from the y tables matched the value given by

the x tables. This is best illustrated as follows:

$$\begin{aligned} s_1 &= e_1^x & s_2 &= e_2 & s_3 &= e_3 \\ s_4 &= \frac{e_1^x}{e_1^y} e_1^y & s_4 &= \frac{e_1^x}{e_1^y} e_4 & s_5 &= \frac{e_1^x}{e_1^y} e_5, \end{aligned} \quad (4.11)$$

where s_i indicates the unnormalized energy proportion in block i of a cluster and e_1^x, e_1^y are the values for the block 1 energy proportion given by the x and y tables, respectively.

The relative energy proportions in the corner blocks was arrived at by assuming the energy shape of the cluster's central, three block row was similar to the top and bottom rows containing the corner blocks. An empirically determined correction was then applied. For example, the energy proportion in block 6 of a cluster was given by:

$$s_6 = F_6 \frac{s_3 s_4}{s_1}, \quad (4.12)$$

where the s_i are the energy proportions in the blocks indicated by the subscript given by equations 4.11 and

$$F_6 = (A + B x_{edge,6} y_{edge,6}) \left(1 + \frac{r}{d_{blk}} \frac{z_{blk}}{z_{MA}} C \cos \theta_{diag,6} \right). \quad (4.13)$$

The constants A, B and C were determined using calibration electrons and depend on the peak block type. The x and y distances from the edges of the peak block closest to the corner block, in this case block 6, to the shower position are $x_{edge,6}$ and $y_{edge,6}$, respectively. The width and thickness of the peak block is d_{blk} and z_{blk} located at $z = z_{MA}$. The distance, r is measured from the center of the Main Array to the shower position while $\theta_{diag,6}$ is the

angle between the vector \vec{r} and the diagonal of the peak block pointing from its center to the corner block, again, block 6 in this case. Similar expressions hold for the other three corner blocks.

With the shape of a shower at a position (x, y) in the Main Array now determined, the energy of the shower was fit by minimizing the generalized chi squared function:

$$\chi^2 = \sum_i \sum_j (E_i - As_i) \mathcal{M}_{ij}^{-1} (E_j - As_j). \quad (4.14)$$

The double sum is over all blocks in the cluster; E_i is the partitioned energy for cluster block i , A is a scale factor and \mathcal{M}^{-1} is an approximation to the inverse of the covariance matrix. We defined this matrix as follows:

$$\mathcal{M}_{ij}^{-1} = \begin{cases} \left(\frac{s_i s_j}{\max(s_i, s_j)^2} \right)^{\frac{1}{4}}, & \text{neighboring blocks} \\ 0, & \text{otherwise.} \end{cases} \quad (4.15)$$

This form for the inverse covariance matrix maximized the correlation between adjacent blocks with equal energy and minimized it between non-neighboring blocks. The energy for each block in the cluster was given by multiplying the relative block energy proportions, s_i by the scale factor A . Each fitted block energy was stored, by cluster, in a special array so that blocks that were shared between two or more clusters could have their raw (EMA) energy partitioned using information from the individual shower fits.

The total Main Array portion of a shower energy was the summed block energies from the fit corrected for a 2% variation with position relative to the center of the peak block. This correction factor was given by a fifth order polynomial in position with the coefficients depending on particle type,

detector region and shower energy. Each coefficient was determined empirically by comparing isolated EGS simulated showers with the information returned from the fit above. This correction was applied only to the total Main Array fitted energy.

Two quantities were calculated to indicate how well the data fit the electromagnetic shower shape. One indicator was a chi squared-per-degree-of-freedom where the chi squared was determined by equation 4.14. The number of free parameters was either one or three depending on whether or not the shower position was fixed by the hodoscopes, while the number of blocks involved in the fit varied depending on the position of the cluster in the Main Array. The second indicator was a fractional energy change which was defined:

$$\frac{\delta E}{E} = \frac{\sqrt{\sum_i^{N_{blocks}} (E_{out} - E_{in})_i^2}}{E_{shower}} \quad (4.16)$$

where $(E_{out} - E_{in})_i$ is the difference between the input and output energy from the fit for block i and E_{shower} is the Main Array fitted shower energy. Both calculated quantities were used in accordance with other information to determine whether a shower was electromagnetic in character (see the section on particle identification), and quantify the quality of the shower measurement.

Virtual Block Energy Partition

Because the tables and the energy fit combined the energies from the two small scintillation glass blocks for clusters defined as in figure 4.2 c this

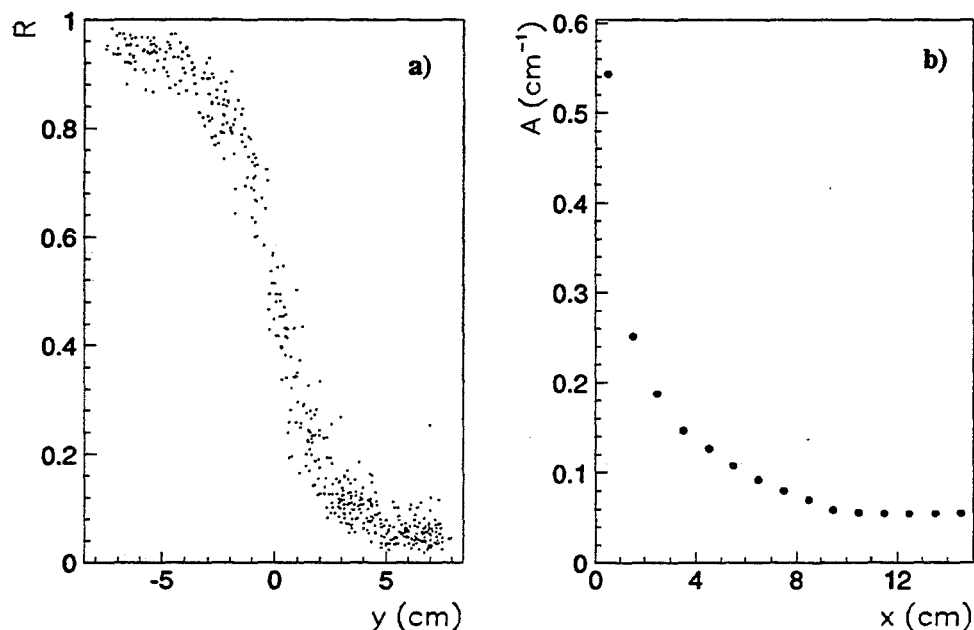


Figure 4.3: Energy partition of a virtual large block's energy from EGS simulated showers. Figure a) shows R vs y for shower centers within 1 cm inside the large block from the boundary. The variation of the parameter $A(x)$ (equation 4.18) is shown in b) for 1 cm steps.

virtual block energy had to be partitioned into energies for its constituent small blocks. For the case illustrated in figure 4.2 c the ratio R was defined:

$$R = \frac{E_{10}}{E_{10} + E_{11}}. \quad (4.17)$$

Using EGS showers, this ratio was then observed to fit the functional form

$$R = \begin{cases} 1 - \frac{\exp(A(x)y)}{2}, & y < 0 \\ \frac{\exp(-A(x)y)}{2}, & y > 0. \end{cases} \quad (4.18)$$

The constant A was determined to depend only on the distance from the boundary (x in the case given). Figure 4.3 shows the dependence of R and A

as a function of x and y for the case discussed above. No energy dependence was observed in R .

Main Array Energy Sharing

When a single block occurred in the block lists for more than one cluster, its energy was distributed or shared between the different clusters. Two sharing algorithms were used in the Main Array reconstruction. An initial energy partition occurred immediately after the primary pattern recognition (call to the subroutine CLUSTER) and distributed the energy of the shared block by the amount of energy in the peak block of each cluster to which the shared block contributed, namely:

$$E'_{i,j} = \frac{E_{1,i}}{\sum_k^{N_{share}} E_{1,k}} E_{i,j}, \quad (4.19)$$

where $E_{i,j}$ is the initial block energy from EMA and $E'_{i,j}$ is the partitioned energy in block i of cluster j .

The second and main sharing algorithm was performed immediately after all the showers were fit. In this algorithm, the energy in block i from the fit of cluster j was scaled so that the summed energy over all clusters in which this block appears was equal to its measured energy in the array EMA.

$$E'_{i,j} = \frac{E_{i,j}^{fit}}{\sum_k^{N_{share}} E_{i,k}^{fit}} E_{i,j} \quad (4.20)$$

The $E_{i,j}^{fit}$ are the block energies from the fit of block i to cluster j . Again, $E_{i,j}$ is the initial block energy from EMA and $E'_{i,j}$ is the partitioned energy in block i of cluster j .

After several calls to SHARE, the cluster list was then ordered by decreasing energy to speed reconstruction and subsequent analysis. This ordering was motivated by the most energetic showers typically being less influenced by overlapping showers.

4.2.4 Position Determination

After a few (2-3) passes through the fitting and sharing algorithms, the cluster positions and energies were reasonably well determined by the Main Array glass. The Main Array position information was then merged with that from the hodoscopes to provide a more precise position measurement and to determine the shower energy deposited in the LGC. Rather than try and form x - y pair crossings in the hodoscopes and try to match these with showers, the Main Array determined positions were projected into the hodoscopes assuming that the particle came directly (undeflected) from the target and a small, rectangular window was searched for possible crossings. The half width of the window was set to three times the expected position error in each view with the x view constrained to the range 3.0-6.0 cm and the y view constrained to the range 3.5-6.0 cm. Using these small windows driven by the glass information eliminated most of the combinatorial problems associated with a full hodoscope pattern recognition, x - y matching and the later association of the possible crossings with clusters.

The search for peaks within the window described above was carried out using the deconvolution method as described in reference [33] and outlined in

appendix B. This technique had the advantage that once a peak was found, its integrated energy was returned along with its position. Also, because the hodoscopes were positioned early in the shower development, the energy versus position spectra were subject to statistical fluctuations which caused multiple peaks to be found for a single shower. This problem was particularly manifest in the low energy showers occurring the GTH region. This method lent itself to the application of digital filtering techniques [34] which we used to minimize the effect of these fluctuations. A description of the filters used and their consequences is given in appendix B.

Two lists of hodoscope peaks within the window were then formed, one for the x view another for the y view. These lists were then ordered according decreasing integrated energy. If corresponding peaks were found in the LGC and the GTH in the hodoscope overlap region (distance between LGC and GTH peak was less than 3.0 cm), the LGC peak was kept. This provided an active plane energy and better position measurements. Peaks in each view that were already associated with a cluster were removed as well as LGC peaks with energy below 150 MeV. The two lists of remaining peaks were then combined to form a list of possible x - y crossings and the one-to-one asymmetry, $A_{1,1}$, was calculated for each crossing.

$$A_{1,1} = \frac{|E_x - E_y|}{E_x + E_y}. \quad (4.21)$$

The hodoscope integrated peak energies for the x and y views are represented in the above equation by E_x and E_y , respectively. The LGC x position dependence of the E_y was also corrected out at this time (see chapter 3 and

reference [33]).

When only one crossing was found within the window and its energy asymmetry was less than 0.30 for the LGC or 0.35 for the GTH, the (x, y) position was projected 10 cm inside the Main Array. The uncertainties assigned to the hodoscopes were 0.17 and 0.36 cm for the x and y views of the LGC and 0.65 and 0.80 cm for the x and y views fo the GTH. If this projected position occured within the peak block the shower position was calculated as the weighted average of the hodoscope position projected onto the front face of the Main Array and glass position.

When two or more crossings occurred in the window an alternate, two peaks in one view to one peak in the other, matching hypothesis was tried by forming the alternate asymmetries $A_{1,2}$ and $A_{2,1}$:

$$A_{1,2} = \frac{|E_x - (E_{y_1} + E_{y_2})|}{E_x + (E_{y_1} + E_{y_2})} \quad (4.22)$$

$$A_{2,1} = \frac{|(E_{x_1} + E_{x_2}) - E_y|}{(E_{x_1} + E_{x_2}) + E_y}, \quad (4.23)$$

where the second subscript indicates either the first or second peak in that view. If the asymmetry for the two-to-one match was better than both the one-to-one matches, the two-to-one hypothesis was kept and the single crossing asymmetries were given the value of either $A_{1,2}$ or $A_{2,1}$, which ever was applicable. Ultimately, the crossing with the lowest asymmetry satisfying the cuts described above was selected as the hodoscope position. For the two-to-one matches, the first crossing appearing in the list was taken. This crossing had the highest energy in the non-degenerate view because the

peaks were ordered as previously discussed. The final shower position was then taken as the weighted average of the glass position and the hodoscope position projected onto the Main Array front face.

On the second time through the position determination, there was an option to add new clusters to the list based on the hodoscope information. With this option invoked, the search window for hodoscope peaks was increased to the size of the cluster. Then all crossings that satisfied the above requirements were projected into the Main Array. If the block into which this position was projected contained more than 300 MeV a new cluster at the location of the Main Array projected hodoscope position was added to the cluster list. The new cluster's initial energy was taken to be the sum of its constituent block energies without sharing. Shared blocks later had their energy partitioned according to the algorithm previously discussed and the position from the Main Array glass was determined in the final fit. This option was only invoked for the analysis of the photon triggers to separate the closely spaced photons from high energy pizero decays.

4.2.5 Active Plane Energy

The one remaining piece of information necessary to complete a shower measurement was the active plane energy. The previous section discusses how x - y crossings in the LGC were picked and associated with individual clusters. The energy measurement for a particular shower in the LGC was taken from the integrated x peak energy of the crossing as returned by the decon-

volution. For the case where the chosen crossing was part of a single x peak matching two y peaks, the energy of the two crossings was given by:

$$E_{x_1} = \left(\frac{E_{y_1}}{E_{y_1} + E_{y_2}} \right) E_x \quad (4.24)$$

$$E_{x_2} = \left(\frac{E_{y_2}}{E_{y_1} + E_{y_2}} \right) E_x, \quad (4.25)$$

with the appropriate crossing chosen as described above.

The shower energy deposited in the Active Converter blocks was reconstructed by projecting the cluster position into each of the two Active Converter block planes, AC and BC. In each plane, three blocks were selected initially, the block hit by the projected position and one block on each side. When the projected position was within 2.0 cm of the $y = 0$ plane, an additional three blocks were added either above or below those already selected to ensure that all the shower energy deposited in each plane was reconstructed. Because the lateral shower size of electromagnetic showers is quite narrow at this point in the shower development,[†] only the blocks within 4.0 cm in x of the projected shower position were used to calculate the Active Converter energy. When an Active Converter block occurred in only one shower, its energy was given by the appropriate EAC value corrected for the y position dependence given by equation 3.9.

For the case when an Active Converter block was shared between two or three showers, the energy deposited in that block was split between the

[†]From shower shape studies using calibration electrons we know that the average shower width in the GTH is 3.0 cm (FWHM). Since the Active Converter blocks occur earlier in the shower development, the lateral shower size must be narrower (see reference [33] for the GTH shower shape information).

different showers so that the ratio of the Active Converter block energies for each shower were proportional to the square root of the different Main Array cluster energies, namely for two showers one has:

$$R_{12} = \frac{E_{AC_1}}{E_{AC_2}} = \left\{ \frac{E_{MA_1}}{E_{MA_2}} \right\}^{\frac{1}{2}}, \quad (4.26)$$

where E_{AC_1} , E_{AC_2} are the Active Converter block energies and E_{MA_1} , E_{MA_2} are the Main Array cluster energies for showers 1 and 2, respectively. Combining this information with the parameterization of the y light attenuation given by equation 3.9 the single block energies the block energies for two shower sharing are given by

$$E_{AC_1} = (y_1 + 10)^n \left[\frac{R_{MA} P_{AC}}{R_{12} + a_{12}^n} \right] \quad (4.27)$$

$$E_{AC_2} = (y_2 + 10)^n \left[\frac{a^n P_{AC}}{R_{12} + a_{12}^n} \right], \quad (4.28)$$

where P_{AC} is the value of EAC for the Active converter block of interest, a_{12}^n is the ratio of the y correction factors, $(y_1 + 10)^n / (y_2 + 10)^n$, and R_{12} is given in equation 4.26. For three shower sharing one has

$$E_{AC_1} = \frac{a_{23}^n R_{13} P_{AC}}{a_{13}^n R_{23} + a_{23}^n R_{13} + (a_{13} a_{23})^n} \quad (4.29)$$

$$E_{AC_2} = \frac{a_{13}^n R_{23} P_{AC}}{a_{13}^n R_{23} + a_{23}^n R_{13} + (a_{13} a_{23})^n} \quad (4.30)$$

$$E_{AC_3} = \frac{(a_{13} a_{24})^n P_{AC}}{a_{13}^n R_{23} + a_{23}^n R_{13} + (a_{13} a_{23})^n}, \quad (4.31)$$

If more than three showers share an Active Converter block, the showers were flagged as bad and no attempt was made to reconstruct their Active

Converter energy. This topology was seen to happen in less than one percent of the events.

The Active Converter energy was calculated for the AC and BC planes by summing up the energies in the individual blocks. The total shower, active plane energy was then given by the sum of the associated AC, BC and LGC energies.

4.2.6 Cluster/Shower Removal

There were two known defects in the electromagnetic reconstruction up to this point and both involved picking up too many clusters. The first such problem involved the primary pattern recognition while the second involved the spawning of new clusters from the LGC and GTH information. For each of these problems, an attempt was made to remove the extra, spurious clusters.

Since the primary pattern recognition used a peak-over-five algorithm, cluster peak blocks could be diagonal neighbors of each other, ie. blocks 6-9 in the standard cluster numbering scheme could be peak blocks of another cluster. Therefore, when a single shower center was near a corner, two clusters were often formed. The DIAGCUT subroutine identified clusters with diagonal peaks and tested them for a single cluster hypothesis. If the cluster with the smaller energy of the identified pair had no associated hodoscope crossing it was flagged as bad and removed from the analysis.

When the hodoscope was allowed to spawn new clusters from crossings

too many identical clusters (those with the same peak block) were often added. Because the shower statistics for the GTH were poor and the asymmetry cuts were loose for both hodoscopes, extra crossings could be formed with each spawning a new cluster. These extra clusters were removed by the routine CHISQCUT which first found all the clusters with the same peak block. If more than two such clusters were found, only the two with the lowest χ^2/DOF were kept. The other clusters were then flagged as bad and removed from the analysis. This later cluster removal scheme was only in effect when the cluster spawning option described in the shower position determination section was in effect (for analysis of the photon triggers).

After the removal of the bad clusters all clusters were refit and the block energies were repartitioned until all the clusters converged or the sharing had been performed ten times.

4.2.7 Energy Corrections

The final step in the electromagnetic reconstruction process was the application of the various corrections to the shower energies. First a correction for the longitudinal light attenuation in the Main Array was made as described in the previous chapter. Then an overall energy scale and pedestal correction was made based on studies of E/p for electrons reconstructed using the tracking and calorimetry.

$$E_{corrected} = \alpha E_{measured} - \beta \quad (4.32)$$

Table 4.2: Energy correction constants for negative beam by calorimeter region.

Region	September		January	
	α	$\beta(\text{GeV})$	α	$\beta(\text{GeV})$
S-SCG	0.9998 ± 0.0036	0.318 ± 0.040	0.9827 ± 0.0022	0.294 ± 0.025
L-SCG(LGC)	0.9890 ± 0.0046	0.267 ± 0.040	1.0048 ± 0.0032	0.380 ± 0.027
L-SCG(AC)	1.0080 ± 0.0037	0.141 ± 0.022	0.9830 ± 0.0023	0.137 ± 0.015
SF5	1.0320 ± 0.0034	0.117 ± 0.017	0.9995 ± 0.0020	-0.091 ± 0.010

Table 4.3: Energy correction constants for positive beam by calorimeter region.

Region	November		January	
	α	$\beta(\text{GeV})$	α	$\beta(\text{GeV})$
S-SCG	1.0000 ± 0.0054	0.446 ± 0.058	0.9926 ± 0.0046	0.258 ± 0.051
L-SCG(LGC)	0.9748 ± 0.0063	0.388 ± 0.056	1.0110 ± 0.0065	0.389 ± 0.054
L-SCG(AC)	0.9891 ± 0.0052	0.165 ± 0.033	0.9572 ± 0.0038	0.032 ± 0.024
SF5	1.0187 ± 0.0050	0.103 ± 0.025	0.9925 ± 0.0036	-0.065 ± 0.018

The correction parameters α and β were found for the four detector regions in four separated data eras during the run and are presented in tables 4.2 and 4.3. The determination of this last correction is presented in the following section.

4.3 Particle Identification

Limited charged and neutral particle identification was available to E705 by combining the information from several detector systems. Charged particles could be identified as either muons, electrons or pions. Muon identification was accomplished by reconstructing a charged particle track which pointed at a triple coincidence in the muon hodoscopes and a hit MUY counter. Electrons were identified as charged particle tracks pointing at an electromag-

netic shower in the calorimeter where the momentum and energy matched within the experiment resolution. Because most charged reaction products are pions, all other charged particle tracks were identified as pions. Neutral particles were identified as photons by requiring an electromagnetic shower in the calorimeter without an associated charged particle track. All other showers in the calorimeter were identified as unknown. The limited charge particle reconstruction in the region surrounding the beam precludes any particle identification in the central region of the calorimeter.

4.3.1 Hadron Rejection

Because hadrons dominate as reaction products, and the Main Array glass had a large number of nuclear interaction lengths, hadronic showers comprised a substantial background in the electromagnetic calorimeter. Showers in the calorimeter were then classified in the calorimeter using the active plane energy information and the quality of the fit to an assumed electromagnetic shower shape. Figure 4.4 shows a comparison of active plane energy and shower fit χ^2/DOF from showers induced by 6.6 GeV, normal incident electrons and pions. From these data it was determined that requiring an energy deposit in the active plane of between 0.2–0.4 GeV kept 94–92% of the electrons while rejecting 84–92% of the pions. The lower and upper limits of this range will hereafter be referred to as the loose and strict electromagnetic cuts, respectively.

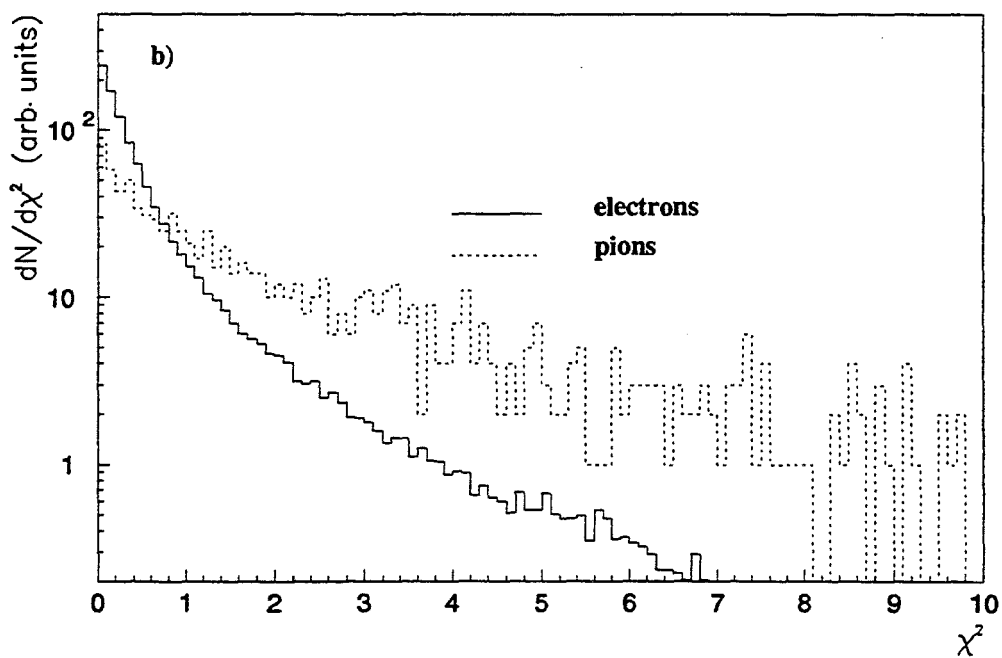
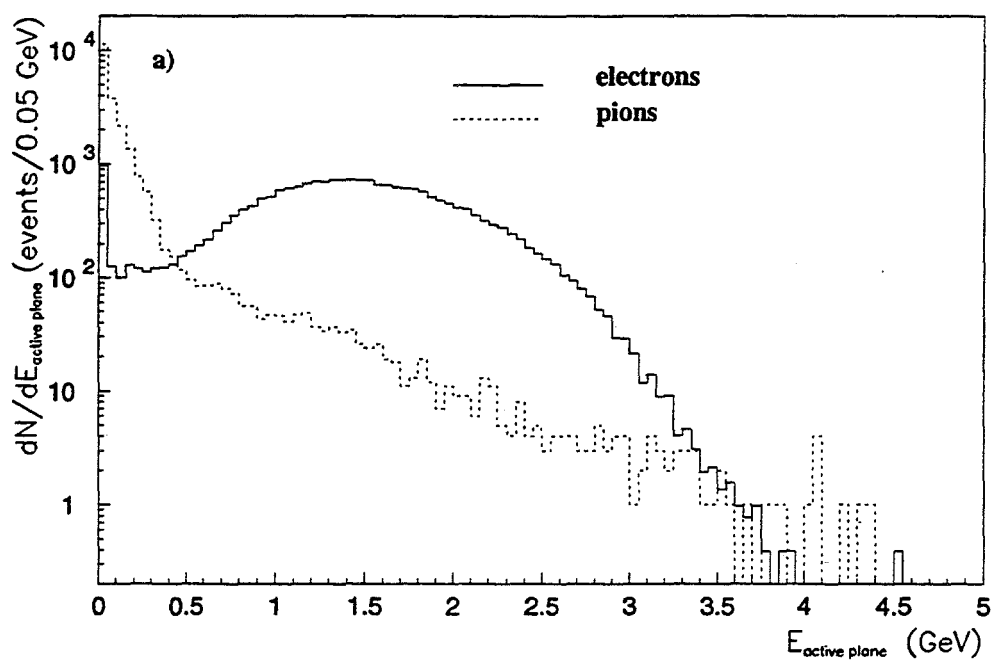


Figure 4.4: Comparison of 6.6 GeV, normal incident electrons and pions: a) active plane energy distributions and b) χ^2/DOF distributions.

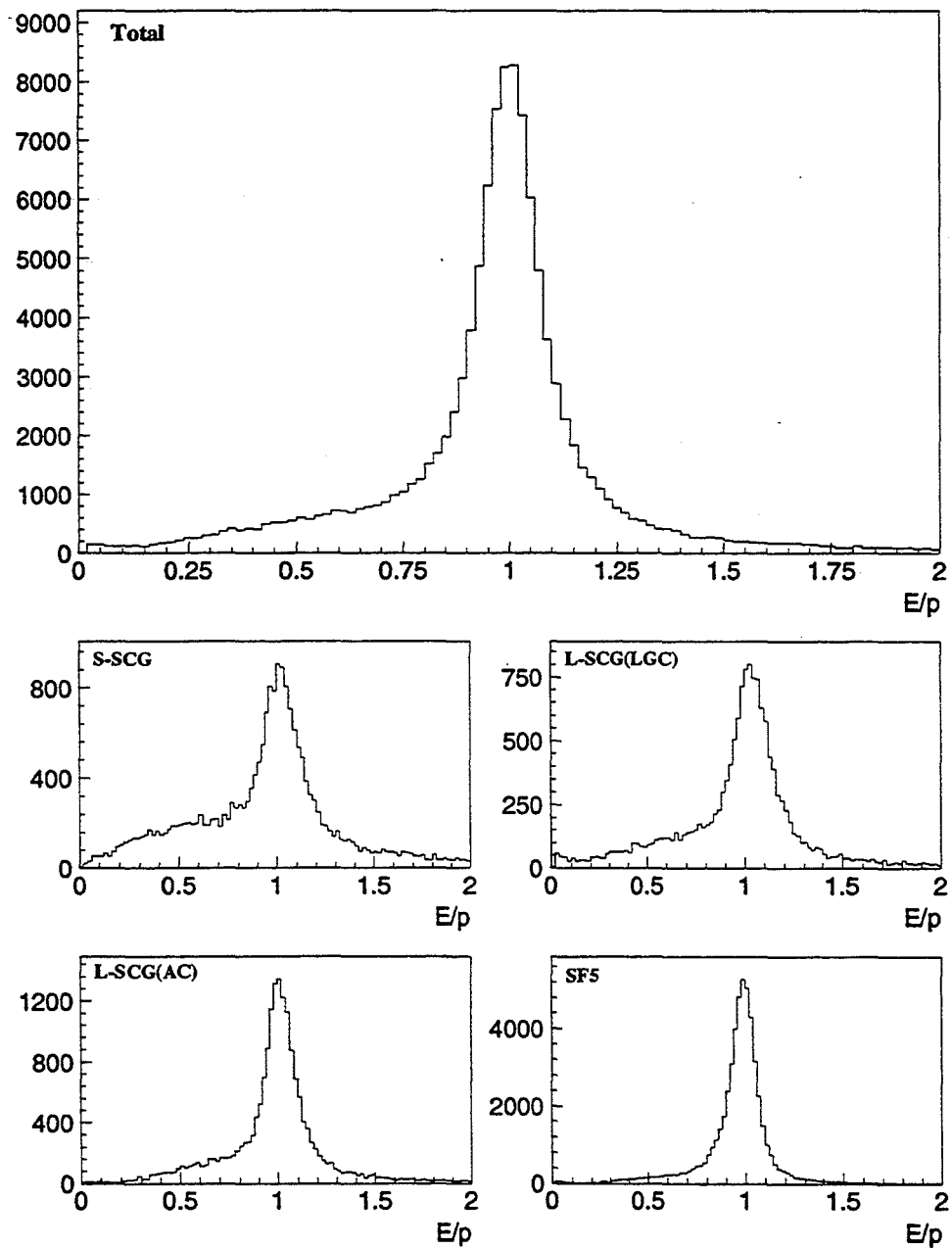


Figure 4.5: E/p spectrum for track-electromagnetic shower matches for the whole detector and by calorimeter region.

4.3.2 Electron/Positron Reconstruction

An electron or a positron, which hereafter will be referred to as electrons, was tagged by first requiring that the position of a strictly defined electromagnetic shower with a hodoscope hit match the position of a charged particle track projected on the Main Array front face within 2.5 cm. Because the minimum track momentum in the spectrometer is 2 GeV/c, measured electrons are extremely relativistic, therefore, the ratio of their energy, E , to their momentum, p , should be unity with the width of the E/p distribution giving the experiment's combined energy and momentum resolution. A typical E/p spectrum is shown in figure 4.5 showing a clear electron peak. Electrons were identified as charged particles satisfying the above criteria with $0.75 < E/p < 1.25$.

Energy Corrections from Electron Studies

The peak in the E/p spectrum was observed to be different from unity and demonstrated a momentum and region dependence. The momentum dependence for each calorimeter region was observed to be nearly linear in $1/p$. This dependence was corrected using the E/p signal in the data with the additional requirement that the χ^2/DOF be less than 2.5 to match subsequent psi-gamma analysis. This E/p spectrum for each region of the calorimeter was split into momentum intervals. Each E/p spectrum was fit to a Gaussian and a fourth order polynomial background. Typical fits are shown in figure 4.6 for the September photon trigger data in the S-SCG region of the

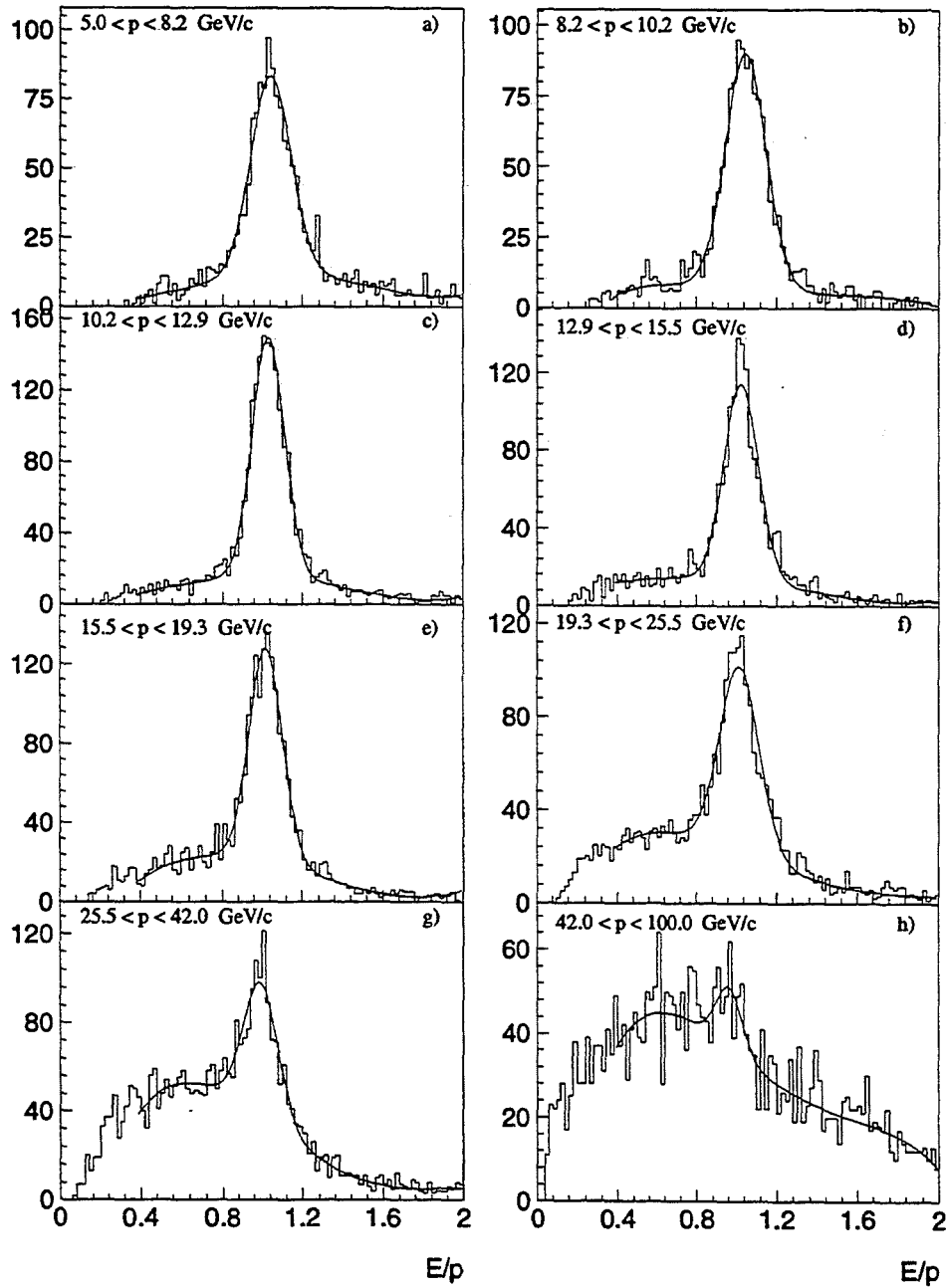


Figure 4.6: Typical E/p spectra in the S-SCG region for various momentum ranges. The plots are from the September data sample with the superimposed curves representing fits described in the text.

September Negative

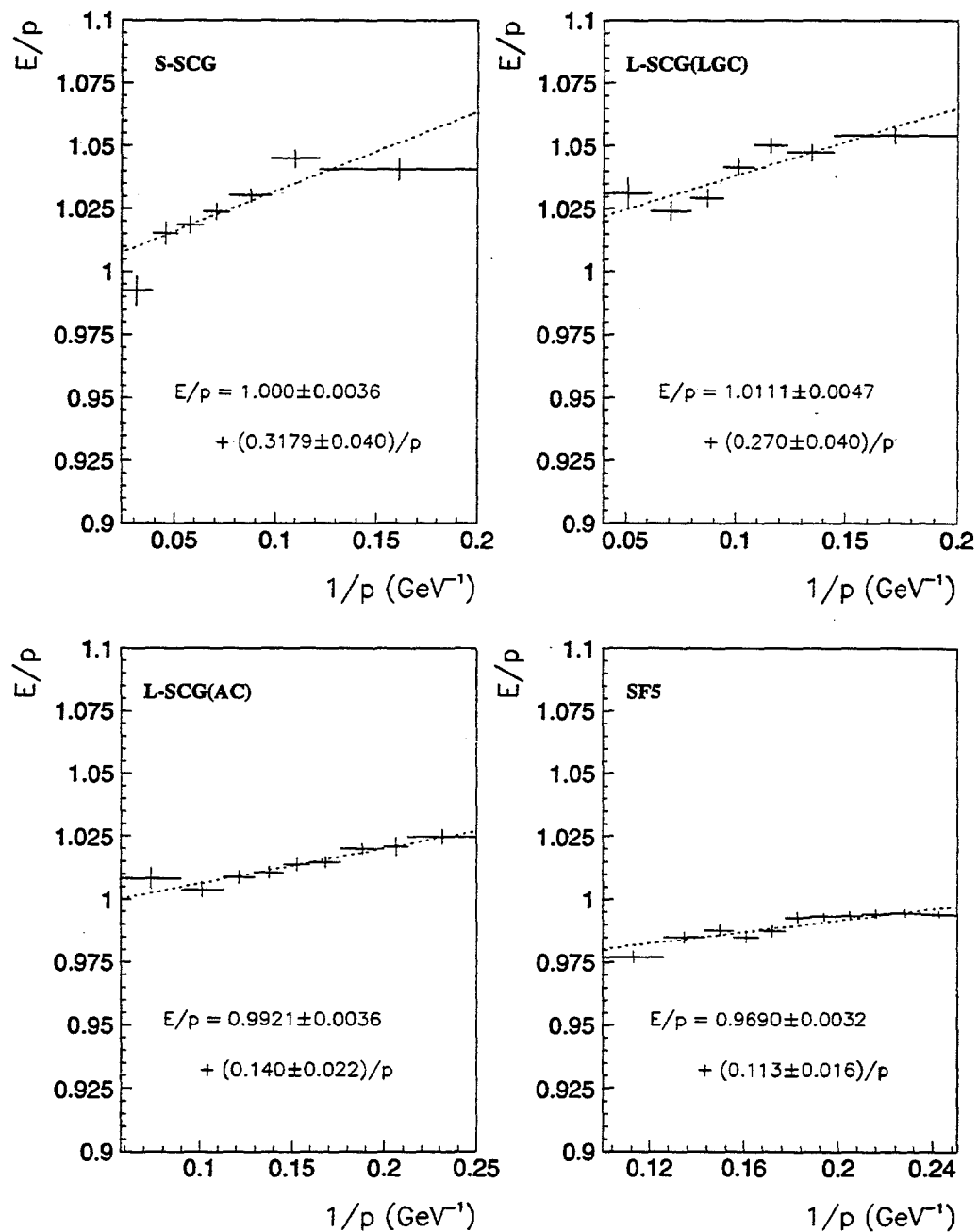


Figure 4.7: September negative electron E/p momentum dependence in the four calorimeter regions: S-SCG, L-SCG behind the LGC, L-SCG behind the Active Converter, SF5.

November Positive

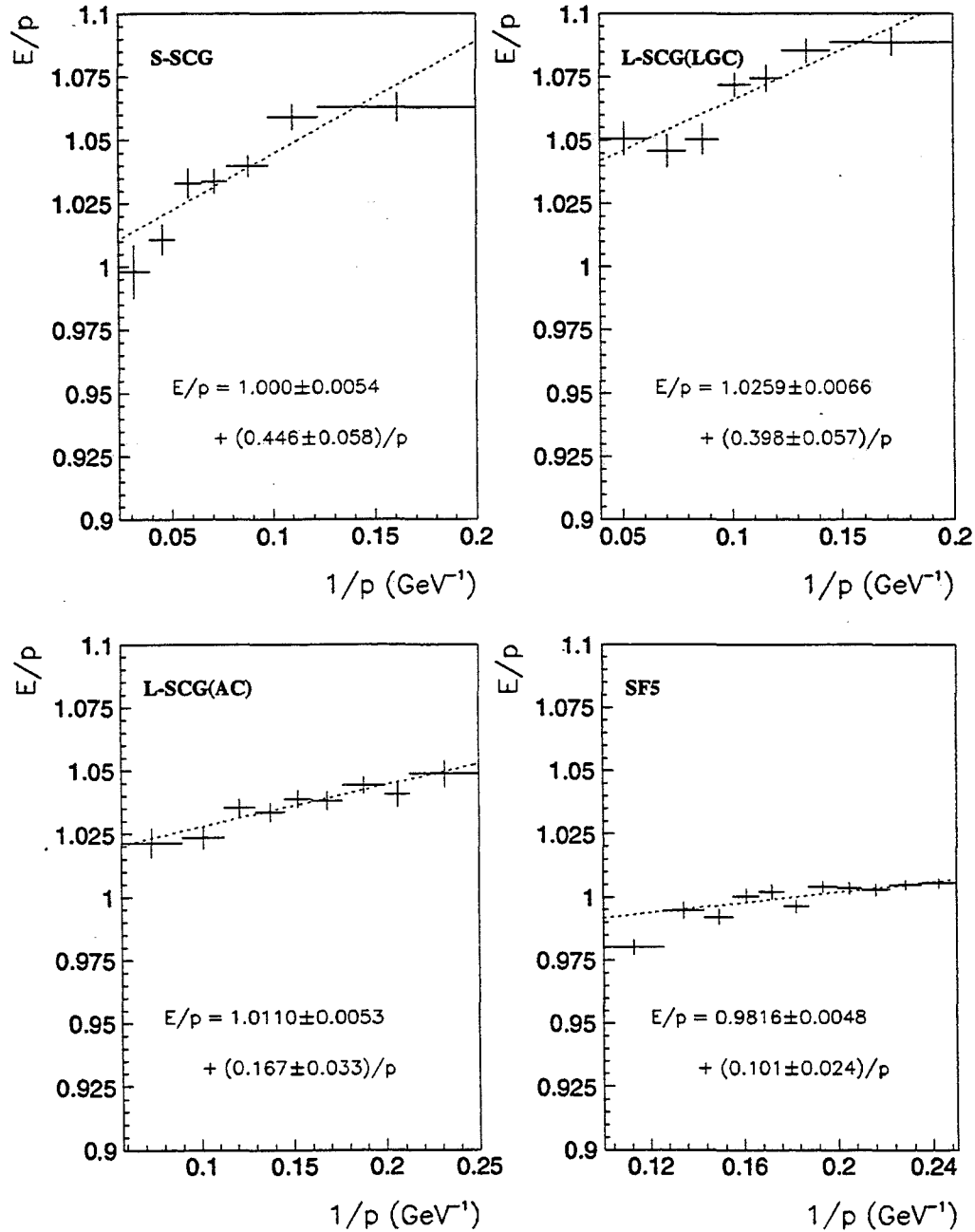


Figure 4.8: November positive electron E/p momentum dependence in the four calorimeter regions: S-SCG, L-SCG behind the LGC, L-SCG behind the Active Converter, SF5.

January Negative

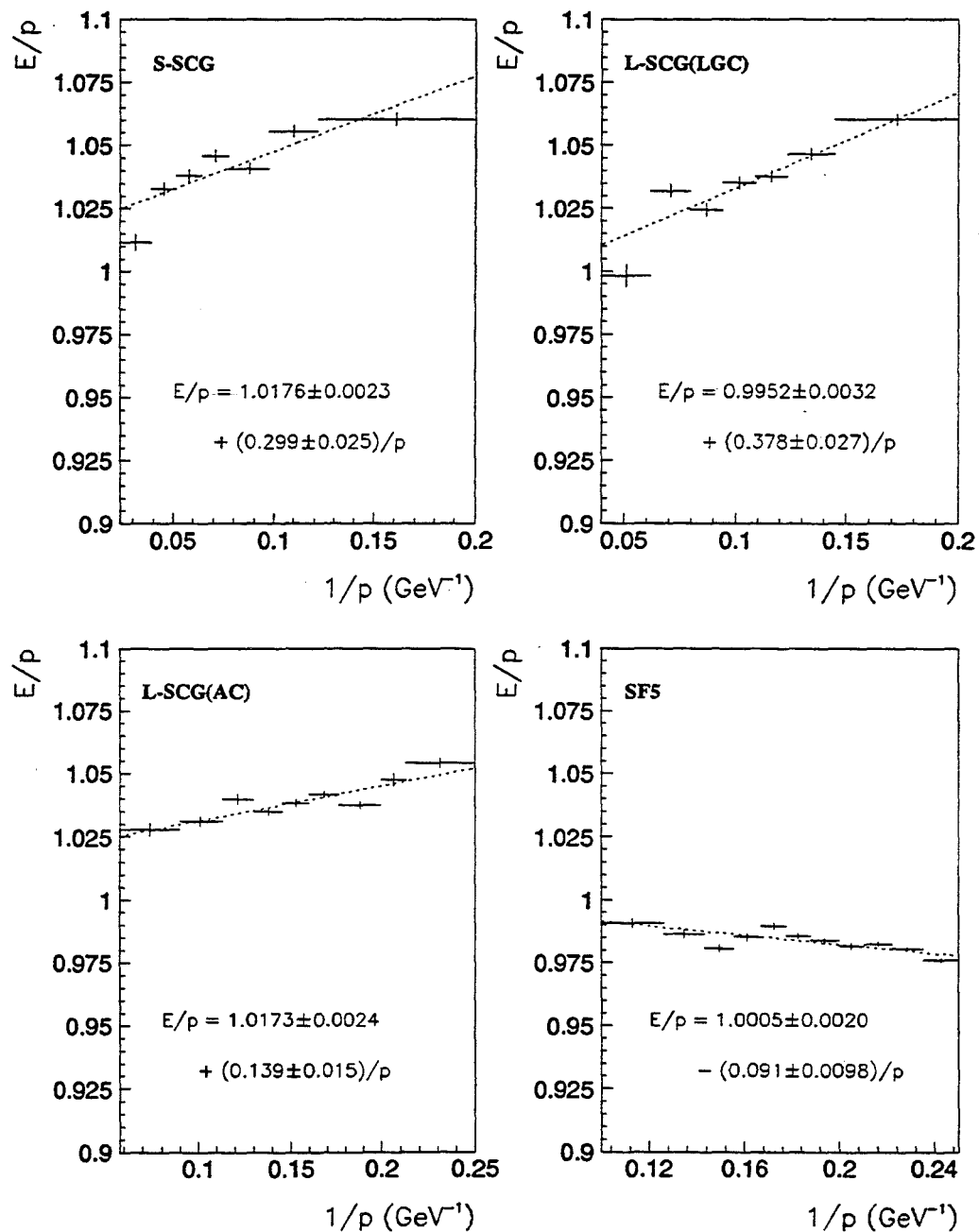


Figure 4.9: January negative electron E/p momentum dependence in the four calorimeter regions: S-SCG, L-SCG behind the LGC, L-SCG behind the Active Converter, SF5.

January Positive

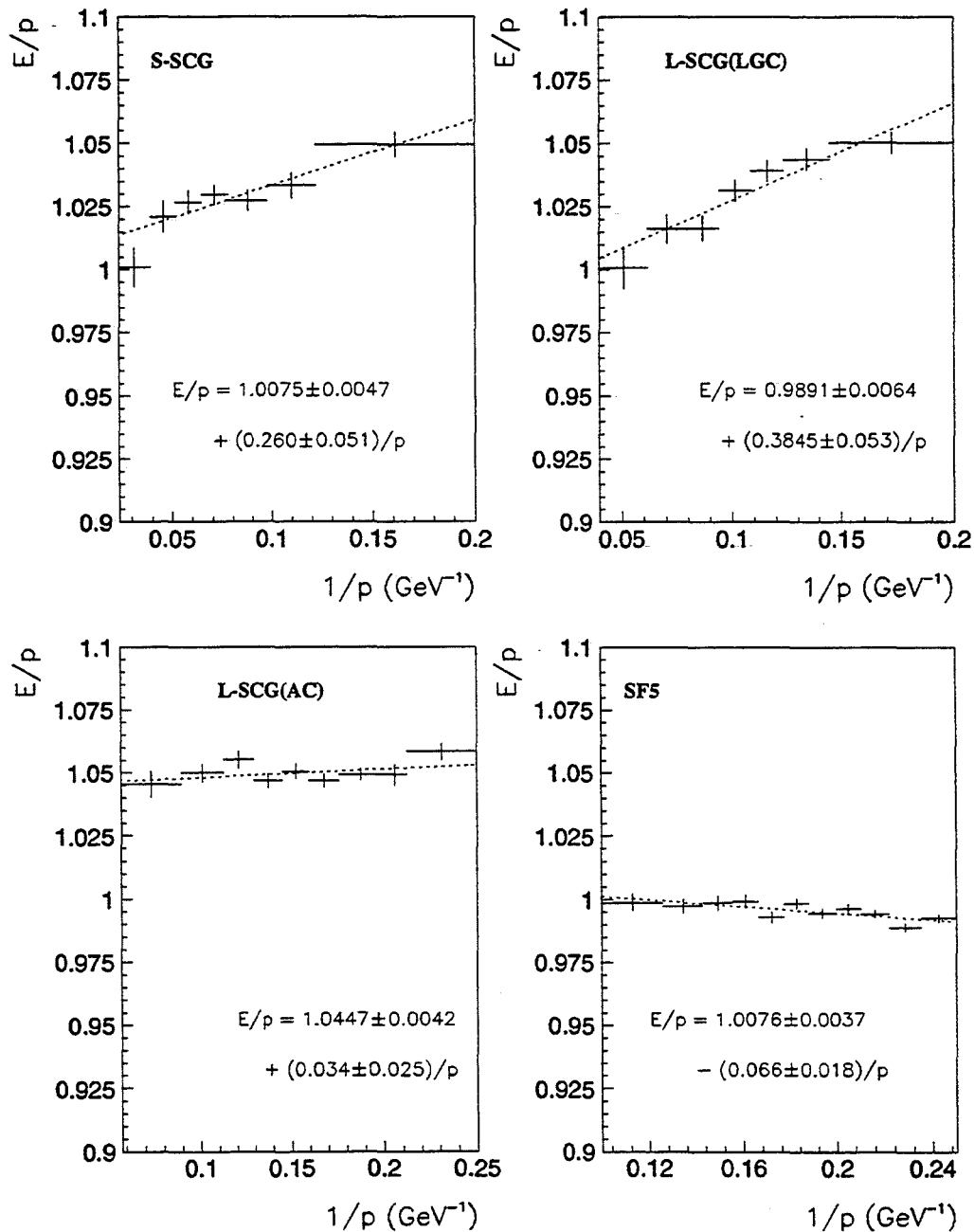


Figure 4.10: January positive electron E/p momentum dependence in the four calorimeter regions: S-SCG, L-SCG behind the LGC, L-SCG behind the Active Converter, SF5.

Table 4.4: Energy resolution parameters from tagged electrons.

Region	a (%)	b (% GeV ^{1/2})
S-SCG	6.40 ± 0.73	7.8 ± 2.3
L-SCG(LGC)	4.14 ± 0.94	13.5 ± 2.7
L-SCG(AC)	4.44 ± 0.69	7.5 ± 1.7
SF5	3.33 ± 0.54	6.2 ± 1.2

calorimeter. The highest momentum interval for each region was not used due to the limited signal available (cf figure 4.6 h). Figures 4:7–4.10 show the momentum dependence and linear fits for the constants a and b below

$$E/p = a + b/p \quad (4.33)$$

for one hundred tape samples of tracked photon triggers in four data eras during the run. Using the above parameterization, and assuming that the momentum measurement is correct, the corrected shower energy is then given by equation 4.32 where the correction constants α and β are defined:

$$\alpha = 1/a, \quad \beta = b/a. \quad (4.34)$$

The values of a and b were determined from the linear fit described above. Again, the correction constants for the four data eras are summarized in tables 4.2 and 4.3.

Energy and Position Resolution

Electrons were also used to determine the calorimeter energy and position resolutions in normal data triggers. The final energy resolution was deter-

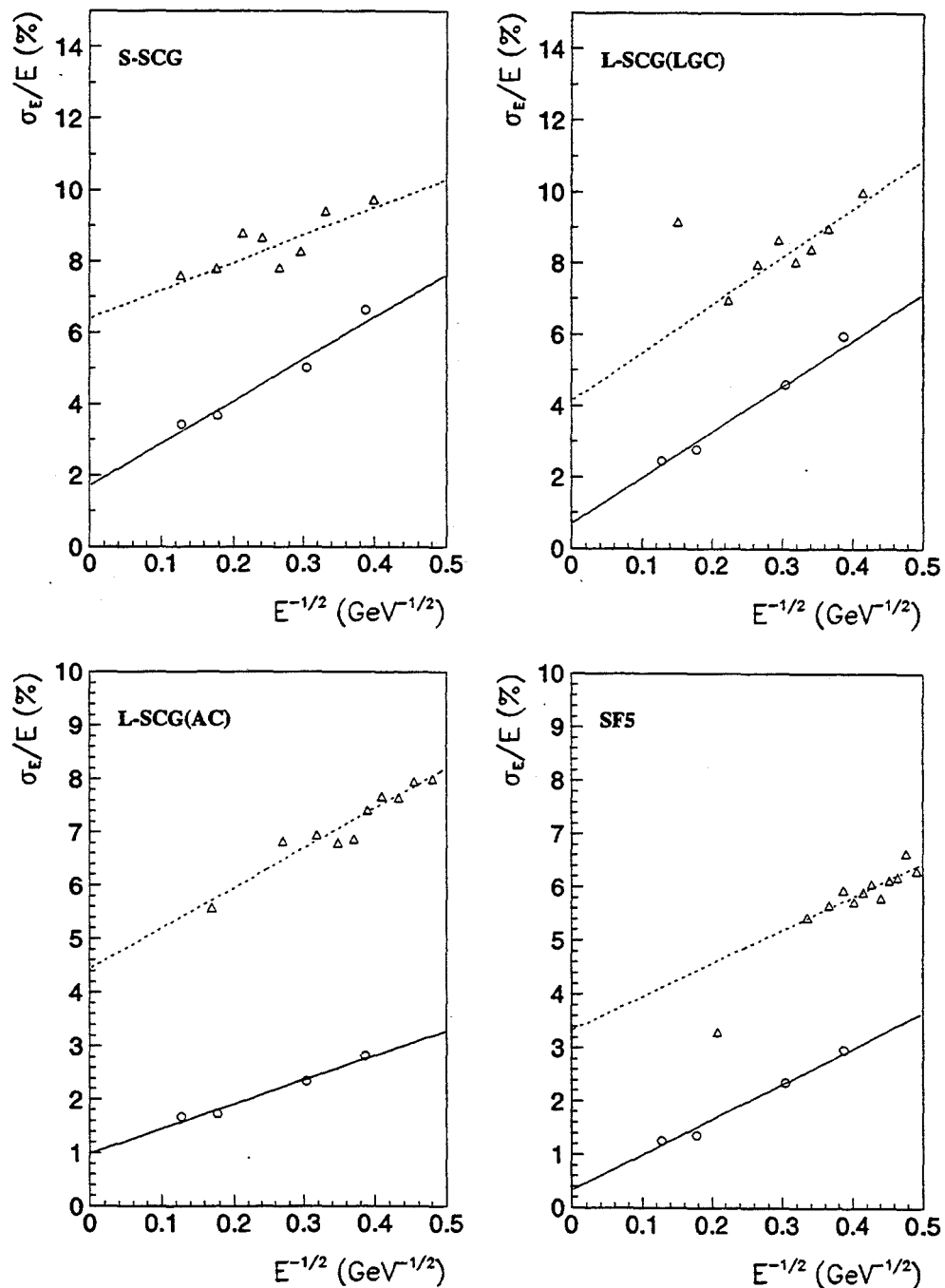


Figure 4.11: Energy resolution compared between data (triangles) and calibration (circles) in the four calorimeter regions.

Table 4.5: Position resolution from tagged electrons.

Region	Position Resolution (cm)	
	x view	y view
LGC [†]	0.1653 ± 0.0026	0.423 ± 0.008
GTH-sngl	0.4944 ± 0.0063	0.655 ± 0.013
GTH-dbl	0.6937 ± 0.0050	0.683 ± 0.013

mined after applying the energy corrections discussed above, the E/p signals were broken up into detector regions and momentum regimes and fit using the same method to get the E/p momentum dependence. The width of the Gaussian returned from the fit was then plotted as a function of $\frac{1}{\sqrt{p}}$. Figure 4.11 compares these results with those from calibration, and summarized in table 4.4. The discrepancy between these two methods of determining the energy resolution is attributed to the dynamic pedestal and confusion in the event due to overlapping showers at different positions and times.

The position resolution was determined by comparing the track position projected on the Main Array front face with that of the shower for tagged electrons. The resulting residual distributions are compared with the results from calibration and are displayed in figure 4.12. The discrepancy between the calibration and data results qualitatively agrees with multiple scattering of the beam in the Čerenkov counter mirrors. Because of the weak

[†]The LGC position residuals were not Gaussian so these numbers were converted to sigmas from a FWHM measurement. The errors come from the uncertainty in the sigma measured from Gaussian fits. The results of which are 0.2095 ± 0.0026 cm with $\chi^2/\text{DOF} = 6.80$ for the x residual and 0.4697 ± 0.0075 cm with $\chi^2/\text{DOF} = 2.85$ for the y residual.

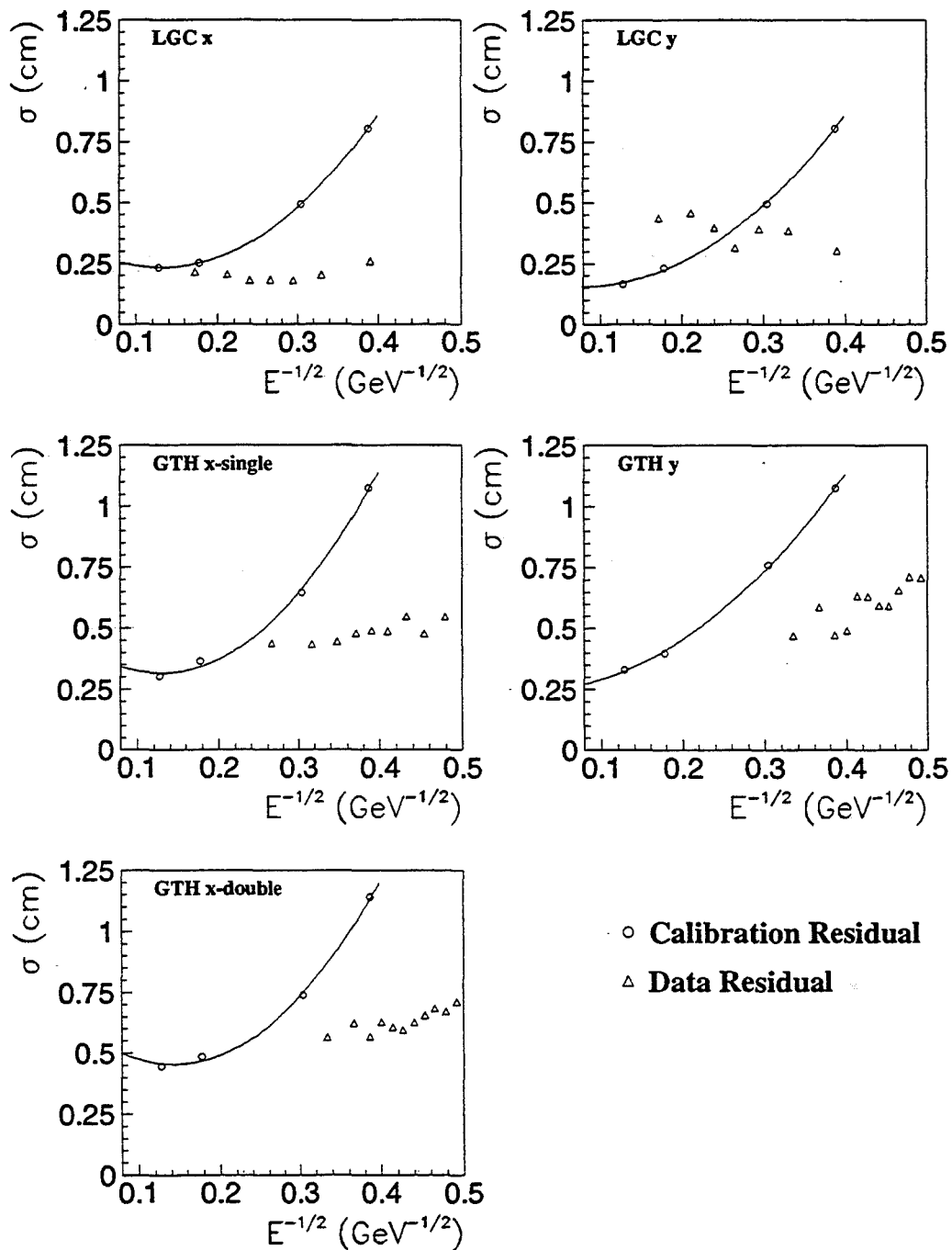


Figure 4.12: Position resolutions comparison between data (triangles) and calibration (circles) for both views of the three hodoscope regions.

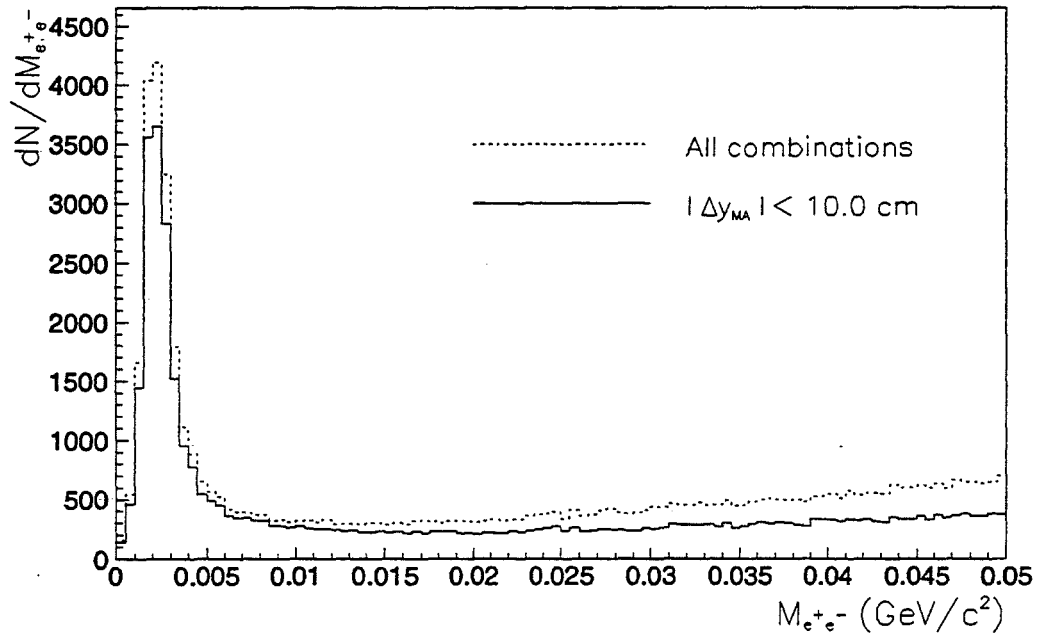


Figure 4.13: Opposite sign track pair invariant mass (assuming electrons)

momentum dependence from electrons in the data, the position resolution was fit to a Gaussian distribution with a single width. The values for the fits in different hodoscope regions are presented in table 4.5.

Reconstruction Efficiency

The electromagnetic reconstruction program's efficiency was determined using electron/positron pairs from photon conversions in the target. An electron/positron pair candidate was identified as a two opposite sign tracks in

the spectrometer. The projected position of each track had to hit within the calorimeter and the individual track momentum was required to be in the range $2.5 < p < 150$ GeV/c. Since Rosie's main magnetic field component was in the y direction, charged particles were deflected primarily in x . An additional requirement that the tracks have a difference in their projected y position at the Main Array front face less than 10 cm cut down on background pairs. Figure 4.13 compares the invariant masses of opposite sign track pairs satisfying the above requirements assuming each track was produced by an electron both with (solid line) and without (dotted line) the Δy requirement. An electron/positron pair candidate was identified as a pair of tracks satisfying the above requirements with an invariant mass $M_{e^+e^-} < 0.01$ GeV/c.

Once a low mass pair was found, the event was run through the electromagnetic reconstruction program. One electron was tagged by searching either sign track for a matching cluster satisfying the electron requirement discussed in section 4.3.2. With one track tagged as an electron we counted the number of times the second track was identified as an electron using the calorimeter information. The reconstruction efficiency was then given by:

$$\epsilon = \frac{\# 2^{\text{nd}} \text{ electrons found}}{\# \text{ electrons expected}} \quad (4.35)$$

A correction to this efficiency then needed to be applied for the misidentification of low mass pairs. Two methods were used to estimate this correction. The first method used same sign pairs and found a misidentification probability of $(8 \pm 1)\%$. The second method mispaired opposite sign tracks

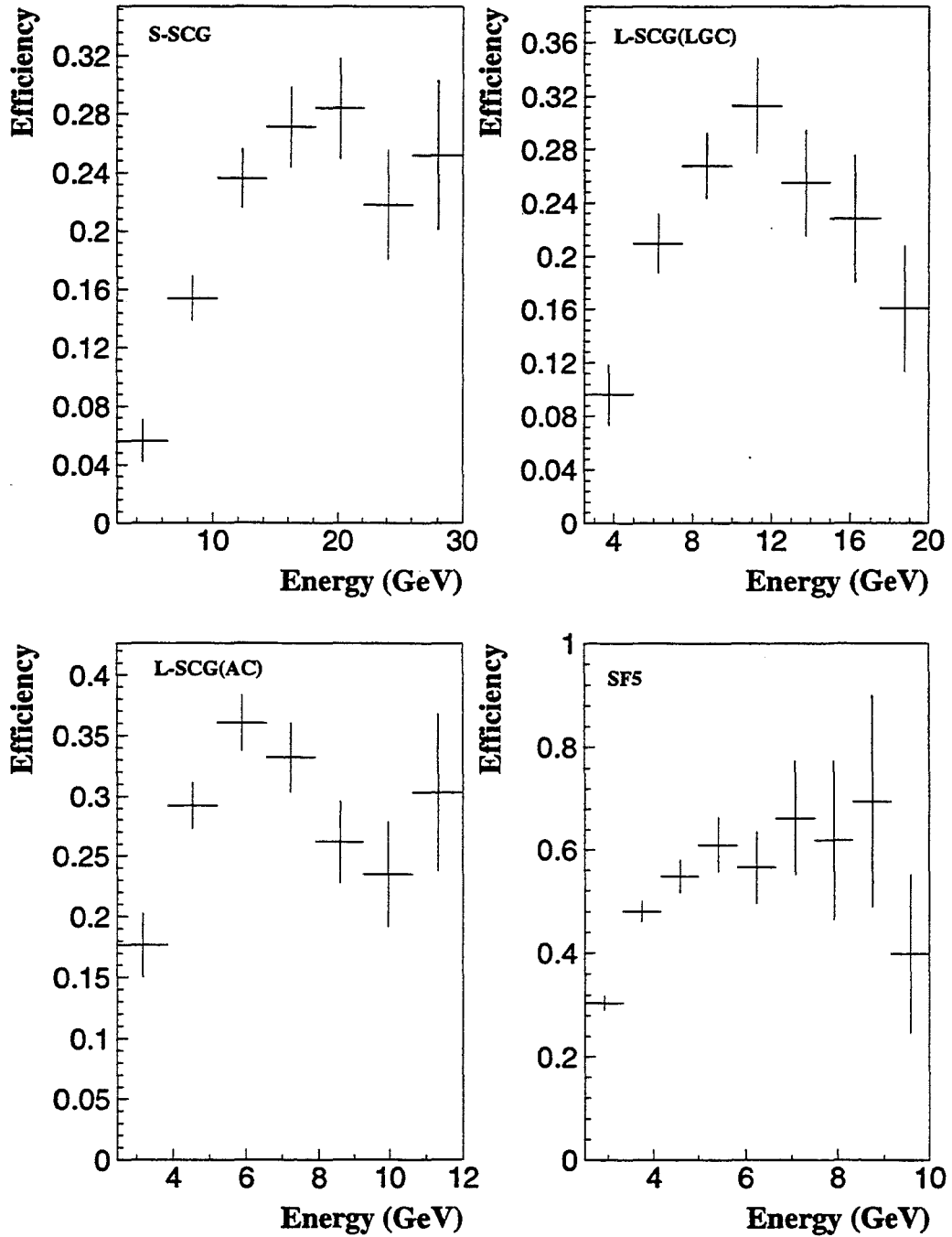


Figure 4.14: Electron reconstruction efficiency for the four detector regions

from different events and found a misidentification probability of $(16 \pm 1)\%$. The average of these two numbers was used giving the value for the correction to the reconstruction efficiency of 1.14 [28].

$$\epsilon = 1.14 \frac{\#2^{\text{nd}} \text{ electrons found}}{\#e^+/e^- \text{ pairs}}. \quad (4.36)$$

Figure 4.14 shows the electron reconstruction efficiency as a function of electron momentum for the four calorimeter regions.

4.3.3 Pizero Reconstruction

In order to verify our understanding of the uncertainties in the calorimeter measurements pizeros were reconstructed from their electromagnetic decay $\pi^0 \rightarrow \gamma\gamma$. Photons were identified as strict electromagnetic showers with a $\chi^2/\text{DOF} < 2.5$ and no associated charged particle track ($R_{tk-clstr} > 6.0$ cm). A photon-photon invariant mass from our final dimuon sample (see chapter 5 is shown in figure 4.15 with photons satisfying the above requirements. The solid curve is the result of a fit to the expected pizero resolution as determined by the Monte Carlo simulation discussed below and a fourth order polynomial background. This fit gave a mass for the pizero peak of 136.42 ± 0.66 MeV/c². We identified pizeros as two photon combinations with an invariant mass in the range $0.105 < M_{\gamma\gamma} < 0.175$ GeV/c².

The expected pizero mass resolution was determined using identified pizeros in the data. The momenta of the photons from these pizeros were rescaled to give a delta function pizero invariant mass. Each photon was then projected back into the Main Array and its x and y positions smeared with

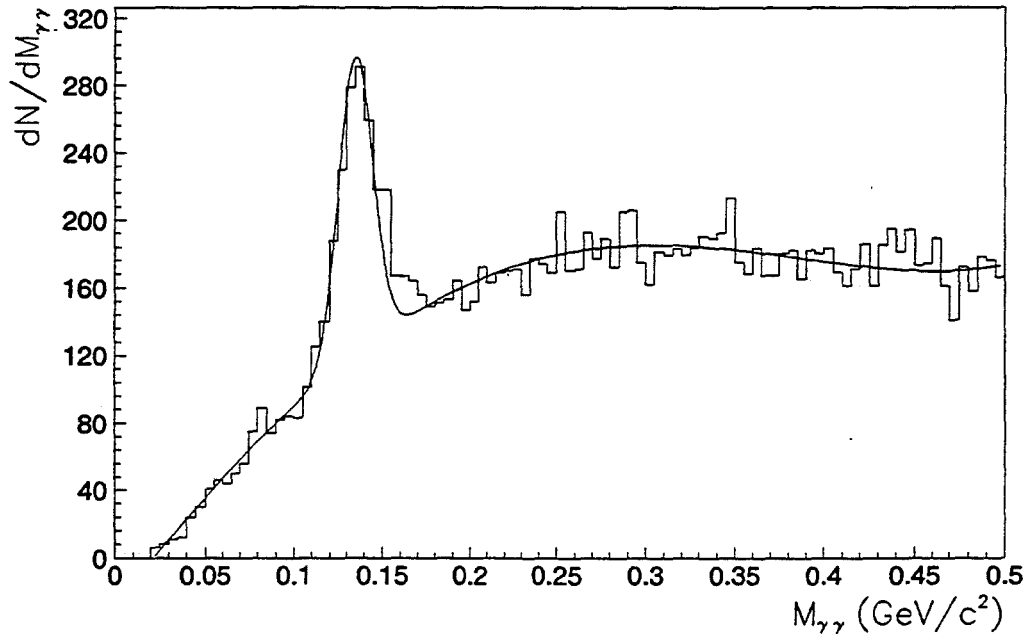


Figure 4.15: Photon-photon invariant mass. Solid line shows the expected π^0 mass resolution on a fourth order polynomial background.

Gaussian distributions with the widths given in table 4.5. The energy resolution of the photons was determined using the results from table 4.4, corrected in the LGC region for the lower average LGC energy deposition of photons relative to electrons.

The difference in the energy resolution between the large SCG blocks behind the LGC and the large SCG blocks behind the Active Converter was attributed entirely to the LGC energy measurement. Therefore, to correct for the different energy depositions, we subtracted in quadrature, the E/p

width in the L-SCG(AC) region from that of the L-SCG(LGC) as a function of energy. This width was then scaled by the relative average LGC energy for photons compared with electrons $R_{\gamma e}$ defined as:

$$R_{\gamma e} = \frac{\langle E_{LGC\gamma} \rangle}{\langle E_{LGCe} \rangle}, \quad (4.37)$$

where $\langle E_{LGC\gamma} \rangle$ and $\langle E_{LGCe} \rangle$ are the average LGC energies for photons and electrons of the same total shower energy, respectively. The average LGC depositions were determined for the incident particle energies described earlier in this chapter from an EGS simulation of the calorimeter. The rescaled LGC width contribution was then added in quadrature back into the L-SCG(AC) width to give the average width for the L-SCG(LGC) for photons. This can be summarized as follows:

$$\sigma_{LGC\gamma} = \left\{ R_{\gamma e}^2 \sigma_{LGCe}^2 + (1 - R_{\gamma e}^2) \sigma_{L-SCG(AC)e}^2 \right\}^{\frac{1}{2}}. \quad (4.38)$$

The same procedure was used to determine the energy resolution of the small SCG block region of the calorimeter.

The individual ‘‘Monte Carlo’’ photon energy was smeared with a Gaussian with the width described above. An invariant mass for the smeared photons was then calculated and fit to Gaussian distribution. The width parameter of this distribution was found to be 9.0 ± 0.5 MeV/c² and agrees reasonably well with the data (see figure 4.15).

Chapter 5

Analysis

The previous chapter described the methods and algorithms used in reconstructing the events in our spectrometer. However, these methods were too slow, the tracking and electromagnetic reconstruction taking in excess of two seconds per event on a VAX 11/780, to fully reconstruct the large number of dimuon triggers taken during the run. Therefore, a certain amount of trigger pre-processing (filtering) was done to reduce the data sample to a manageable level. Events passing the filter were analyzed more completely with tighter selection criteria to arrive at our final dimuon sample. We used the resulting data sample to reconstruct the radiative decays into a J/ψ final state. This chapter presents the methods used to pre-process the data into our final J/ψ -photon sample.

5.1 Data Reduction

5.1.1 Dimuon Filtering (Pass I)

All the dimuon triggers were preprocessed on the Fermilab Advanced Computer Program (ACP) system [35] with a dimuon filter program. The filter program served to verify the trigger and to perform a more accurate mass calculation for the triggering muons. The algorithm used by the filter was

similar to that used by the dimuon trigger processor as described in chapter 2 and reference [25].

The raw dimuon trigger was verified by requiring the muon counter latches had at least two triple coincidences occurring in different quadrants for the event. An additional requirement that a MUY hit overlap each triple coincidence was also made. The hits in the x views of the downstream drift chambers were decoded using the time information to accurately determine the position of the hit in each plane. A road in the xz plane was formed for each triple coincidence and searched for tracks using an abbreviated version of the seed plane method discussed in the previous chapter. Acceptable tracks were required to have at least one hit in either x plane of each downstream drift chamber and the track trajectory was required to be within the spectrometer's acceptance. Upstream track segments were formed from the (x, y) position of the downstream track at $z = 0$ and projecting to the (x, y) position of the beam track located at the z position of the target's center. When no beam track was found or multiple beam tracks were found, the (x, y, z) position of the target center was used to anchor the upstream line segment. The momentum of each muon candidate was calculated using only xz view tracks. Mass combinations were then formed for each opposite sign muon pair using the MUY hit for the particular triple coincidence to help determine the opening angle between the two muons candidates. Events which had an opposite sign muon pair with a mass passing greater than $2.6 \text{ GeV}/c^2$ were analyzed further with the algorithms discussed in the previous chapter and

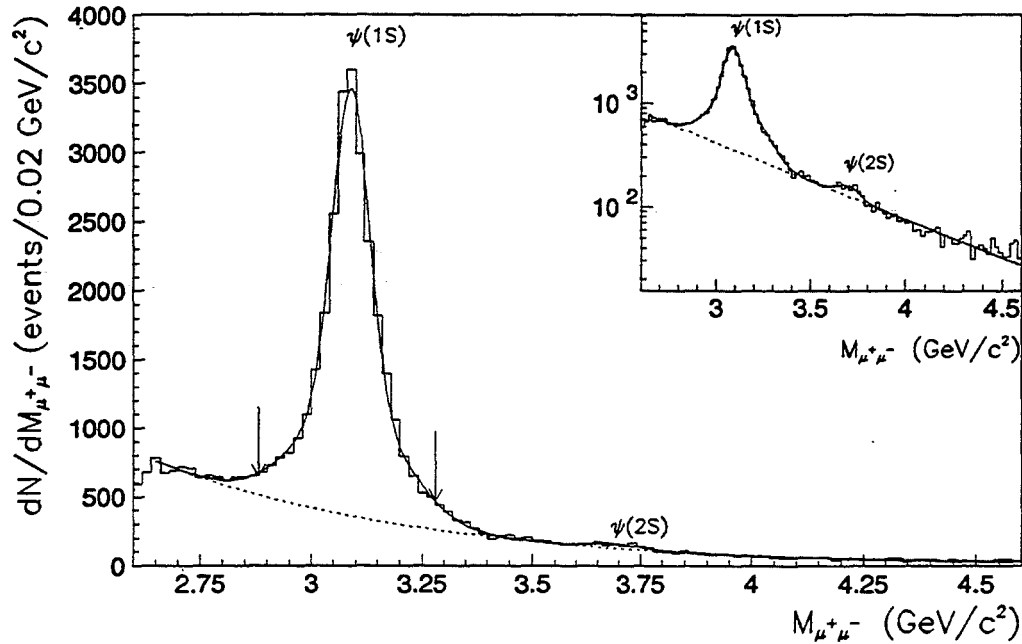


Figure 5.1: Opposite sign dimuon mass spectrum. The solid line represents the fit described in the text. Arrows indicate the pass II definition of the J/ψ mass region.

written to tape for subsequent analysis. More details on the filter program and its performance may be found in reference [30].

5.1.2 J/psi Reconstruction (Pass II)

Events which passed the filter requirements and were tracked as discussed above were subsequently re-analyzed with more restrictive requirements on the muons to further reduce the background on our dimuon sample. The parameters used to cut the data included:

- Rear track quality (χ^2 from the fit and number of hits on the track).

- Muon counter residuals (Δx_{MU1} , Δx_{MU2} , Δx_{MU3} and Δy_{MUY}).
- Front and rear track y slope match (Δm_{yz}).
- Front and rear track segment position match at the matching plane,
 $z_{match} = -4.8 \text{ cm}(\Delta x_{match}, \Delta y_{match})$.
- Maximum muon momentum.

The specific values for the cuts, the method used to determine them and results of their application are listed in reference [28]. Figure 5.1 shows our pass II dimuon sample. J/psis were identified by the pass II program as having an opposite sign dimuon mass in the range $2.88 < M_{\mu^+\mu^-} < 3.28 \text{ GeV}/c^2$. This range was restricted further for the J/psi–photon analysis.

We obtained the number of J/psis and psiprimes in our sample by first fitting the dimuon mass spectrum for the entire sample to a double Gaussian function for the J/psi and a single Gaussian for the psiprime with an exponential background. The double gaussian resolution function for the J/psi was parameterized according to:

$$S(m) = \frac{N_\psi}{\sqrt{2\pi}(C\sigma_1 + \sigma_2)} \left\{ C e^{-\frac{1}{2}\left(\frac{m-m_0}{\sigma_1}\right)^2} + e^{-\frac{1}{2}\left(\frac{m-m_0}{\sigma_2}\right)^2} \right\}. \quad (5.1)$$

The values for C , σ_1 and σ_2 were determined from this fit to be 2.83, 0.041 GeV/c² and 0.115 GeV/c², respectively. This result compares favorably with the resolution obtained from a Monte Carlo simulation which yields the fit parameter values: 2.94 ± 0.25 , $(0.038 \pm 0.001) \text{ GeV}/c^2$ and

Table 5.1: Number of reconstructed J/ψ s and ψ primes by beam type.

Beam Type	Number of J/ψ s		Number of ψ primes (total)
	All x_F	$x_F > 0$	
π^+	5724 ± 91	5150 ± 87	68 ± 22
π^-	10200 ± 110	9190 ± 120	105 ± 29
π^\pm (combined)	15900 ± 150	14330 ± 140	156 ± 33
p	6425 ± 97	5710 ± 86	66 ± 22
\bar{p}	160 ± 16	160 ± 16	–
Total	23490 ± 180	21090 ± 170	317 ± 70

(0.115 ± 0.015) GeV/ c^2 [28] for the same parameters, respectively. The width of the ψ prime was measured to be 0.56 GeV/ c^2 .

The J/ψ and ψ prime resolution function parameters were fixed to the values determined from the fit to the entire sample. The sample was then broken up into the different beam types and fit for the number of J/ψ s and ψ primes above background. Table 5.1 lists the number of J/ψ s and ψ primes observed. The number of J/ψ s observed in the forward hemisphere was also kept because many publications quote cross sections only in this kinematic regime. These numbers will be used later to calculate the cross sections for the χ states.

5.2 Electromagnetic Showers

Because photon triggers were used to determine the energy corrections used in this analysis (see section 4.3.2) the question arises whether these cor-

Table 5.2: Means and widths of E/p in our dimuon and photon trigger samples.

Data Sample	LGC Region		AC Region	
	$\langle E/p \rangle$	$\sigma_{E/p}$	$\langle E/p \rangle$	$\sigma_{E/p}$
ψ candidates	0.9976 ± 0.0068	0.0920 ± 0.0075	0.9809 ± 0.0018	0.0749 ± 0.0020
September Negative	0.9959 ± 0.0010	0.0906 ± 0.0011	0.9906 ± 0.0004	0.0748 ± 0.0004
November Positive	0.9951 ± 0.0016	0.0920 ± 0.0017	0.9949 ± 0.0005	0.0800 ± 0.0006
January Positive	0.9963 ± 0.0013	0.0893 ± 0.0014	0.9945 ± 0.0004	0.0766 ± 0.0004

rections are appropriate for our final J/psi candidate sample. Studies to determine corrections directly from E/p in the J/psi candidate data are severely limited by the number of events in this sample. Therefore, we resorted to comparisons between distributions in the different E/p samples for the two active plane regions of the calorimeter.

First, comparisons were made between parameters of the peaks in the E/p distributions themselves. Each E/p distribution was fit to a Gaussian peak and a fourth order polynomial. Figure 5.2 shows representative E/p distributions from the J/psi candidate and September negative data samples with the fits overlaid. For completeness, representative momentum distributions for electrons tagged using E/p are also shown in figure 5.3. Means and sigmas from the Gaussian of the fits are summarized in table 5.2. The LGC region shows good agreement among all the different data samples, while the Active Converter region shows a one percent shift in the mean of the J/psi candidate E/p peak relative to that of the photon trigger samples. Otherwise the Active Converter regions shows reasonable agreement among the widths in the different samples.

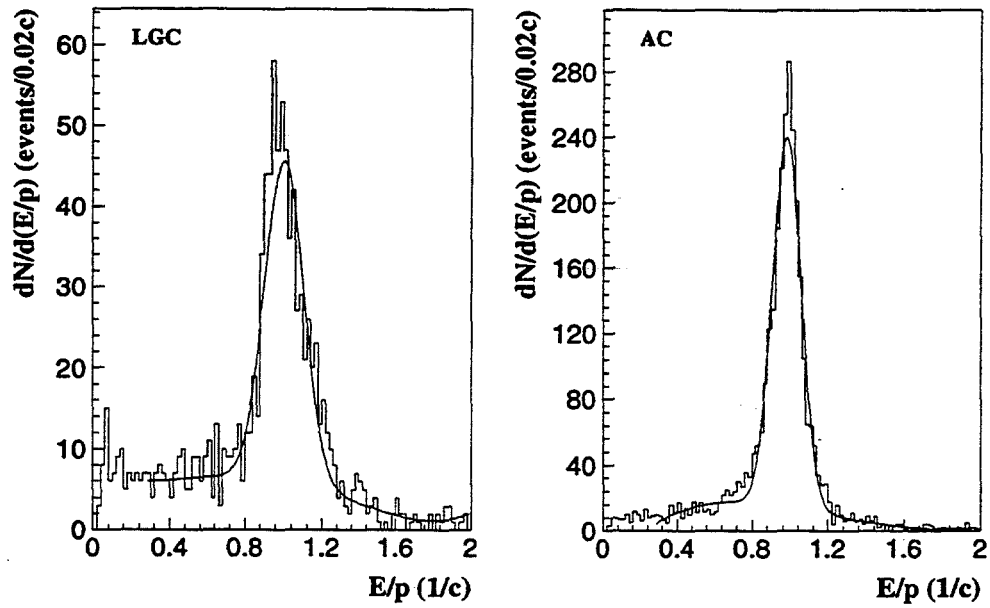
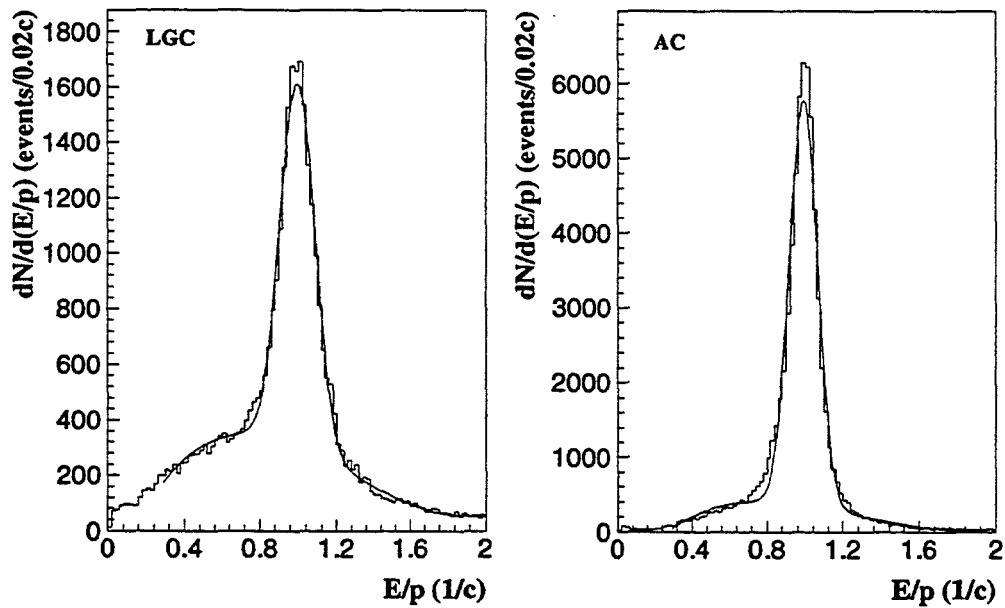
J/psi Candidates**September Photon Triggers**

Figure 5.2: E/p for J/ψ candidates and photon triggers. The curves represent the fits described in the text.

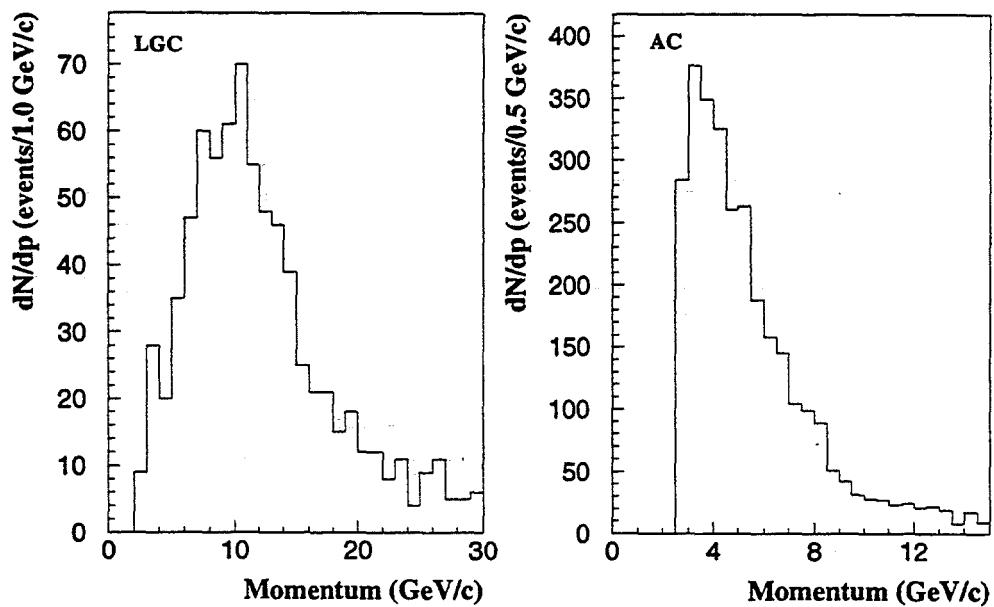
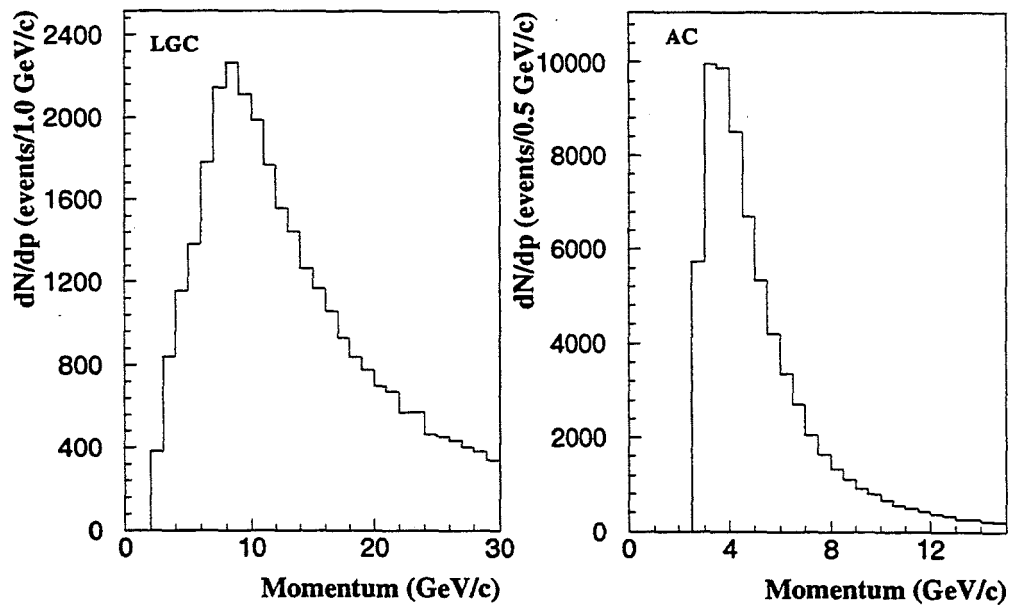
J/psi Candidates**September Photon Triggers**

Figure 5.3: Momentum distributions for J/psi candidate and photon trigger electrons.

Table 5.3: Kolmogorov comparisons of J/psi candidate and photon trigger samples of E/p.

Detector Region	Probability of Shape Compatability		
	Sept. Neg.	Nov. Pos.	Jan. Pos.
LGC	0.9076	0.7527	0.8529
AC	0.0018	0.0034	0.0010
AC ($1.012 \times E$)	0.5583	0.3240	0.9998

As an additional check on the consistency of the shape of the distributions a Kolmogorov test [37] was applied comparing the E/p distributions from the J/psi candidate data with the those from the photon trigger data. To compare only the peaks of the distributions the restriction $0.8 < E/p < 1.2$ was made. The results of these comparisons are expressed in terms of probabilities that the sample distribution (J/psi candidate sample in this case) came from the parent distribution (photon triggers). The results of these tests are tabulated in 5.3. The LGC region shows good good agreement between the J/psi candidate data and that from the photon triggers. When the one percent offset is accounted for in the Active Converter region reasonable agreement between the different data sets is attained.

However, this one percent correction was not used in the final analysis of our J/psi-photon sample. Monte Carlo studies show that nn.nn% of chi photons are found in the scintillation glass region of the calorimeter and a one percent correction to the SF5 region would have little effect. As an additional test, the correction was applied and the chi signal was fit using the

method described in the following chapter with no measureable difference in the fit parameters.

5.3 J/psi–Photon Mass Spectrum

The J/psi candidates in the pass II definition of the dimuon mass window were observed to have a signal/background of 3.3. We increased this ratio to 5.6 by further restricting the range of dimuon masses accepted to $2.98 < M_{\mu^+\mu^-} < 3.18 \text{ GeV}/c^2$ which gave a purer sample of J/psis.

In order to observe J/psi–photon final states, all strict electromagnetic showers (defined in the previous chapter) with associated hodoscope crossings were combined with the J/psi candidate and the mass difference, defined as:

$$M_{diff} = M_{\mu^+\mu^-\gamma} - M_{\mu^+\mu^-}. \quad (5.2)$$

was calculated for each pair. The advantage to using the mass difference over the $M_{\mu^+\mu^-\gamma}$ calculation is that the contribution to the width of J/psi–photon masses near the J/psi mass due to the uncertainty in the measurement of the muons is reduced (cf. appendix C). Figure 5.4 a shows the mass difference spectrum for J/psi candidates paired with strict electromagnetic showers with associated hodoscope crossings. The strict electromagnetic shower multiplicity and energy distributions are also found in figure 5.4 b and c.

Because the average shower multiplicity for strict electromagnetic showers is 1.8 there are extra J/psi–photon combinations on the plot due to electrons and due to photons from pizero decays. These extra combinations

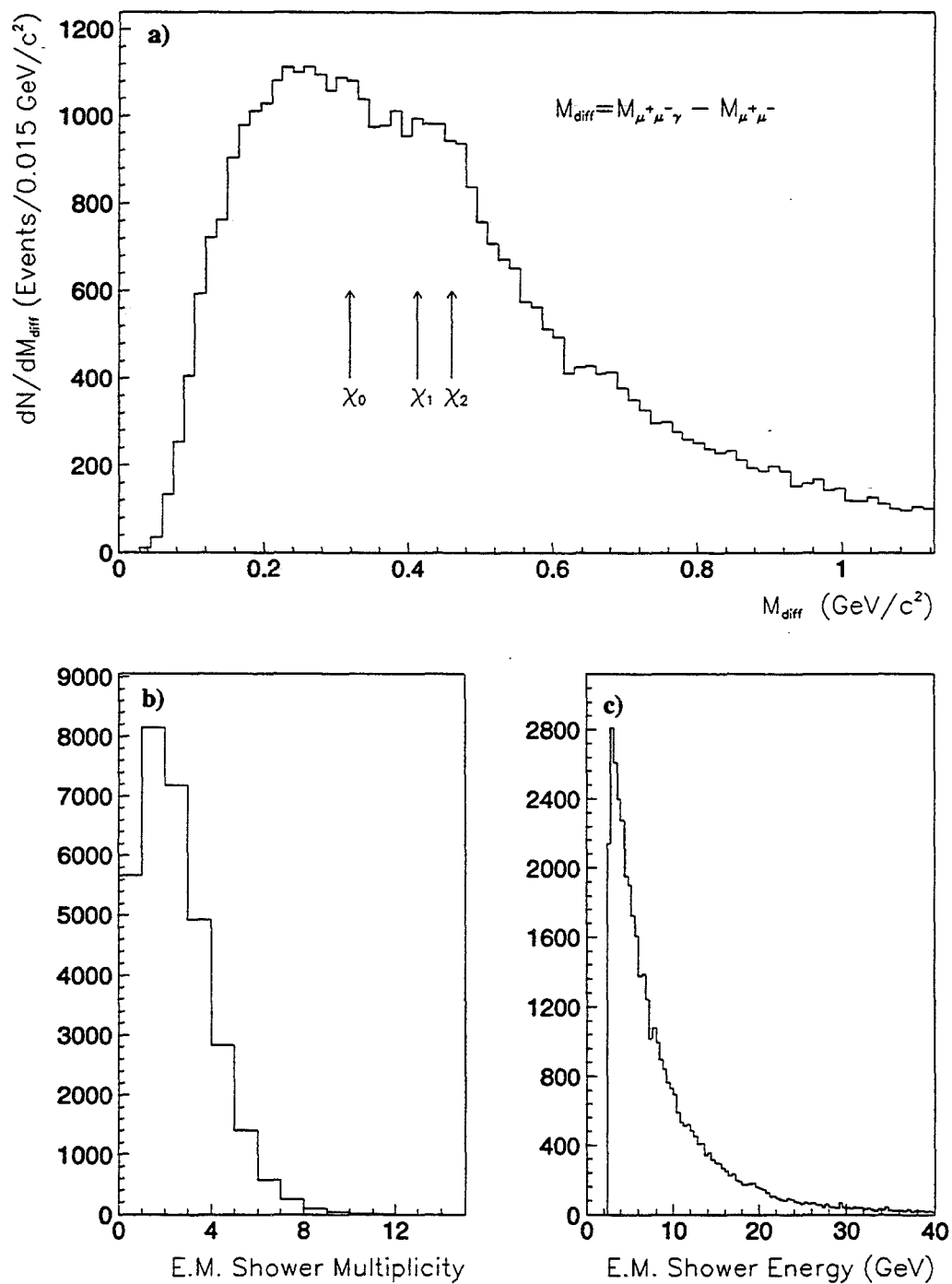


Figure 5.4: J/ψ -electromagnetic shower mass difference, shower multiplicity and shower energy distributions.

contributed to the background and were reduced by making the additional requirements on each shower listed below.

- $E_{shower} > 2.5 \text{ GeV}/c^2$
- $r_{track_{min}} > 6.0 \text{ cm}$
- $M_{\gamma\gamma_{min}} > 200 \text{ MeV}/c^2$
- $\chi^2/\text{DOF} < 2.5$

The minimum energy and chi squared cuts required the showers to be well measured. The cut on the distance from the shower to the Main Array projected position of the nearest charged particle track ($r_{track_{min}}$) was used to remove electrons and hadrons showering in the active plane. Photons from pizero decays were removed by forming the minimum invariant mass for shower pairs ($M_{\gamma\gamma_{min}}$). The first shower was taken as the one of interest and satisfied all the requirements above except the two shower invariant mass, while the second photon was required to satisfy the loose electromagnetic cuts only (see previous chapter). Application of these requirements reduced the average shower multiplicity to 1.4.

Showers passing these cuts defined our *single photon* sample for this analysis. Distributions of the cut parameters are shown in figures 5.5 a–d, where the dotted line is the uncut distribution and the solid line gives the distribution with all cuts in place but the one plotted. The shaded region on each plot indicates the data excluded by the cut. Shower multiplicity distributions before and after the application of the cuts are given in figures 5.5 e and

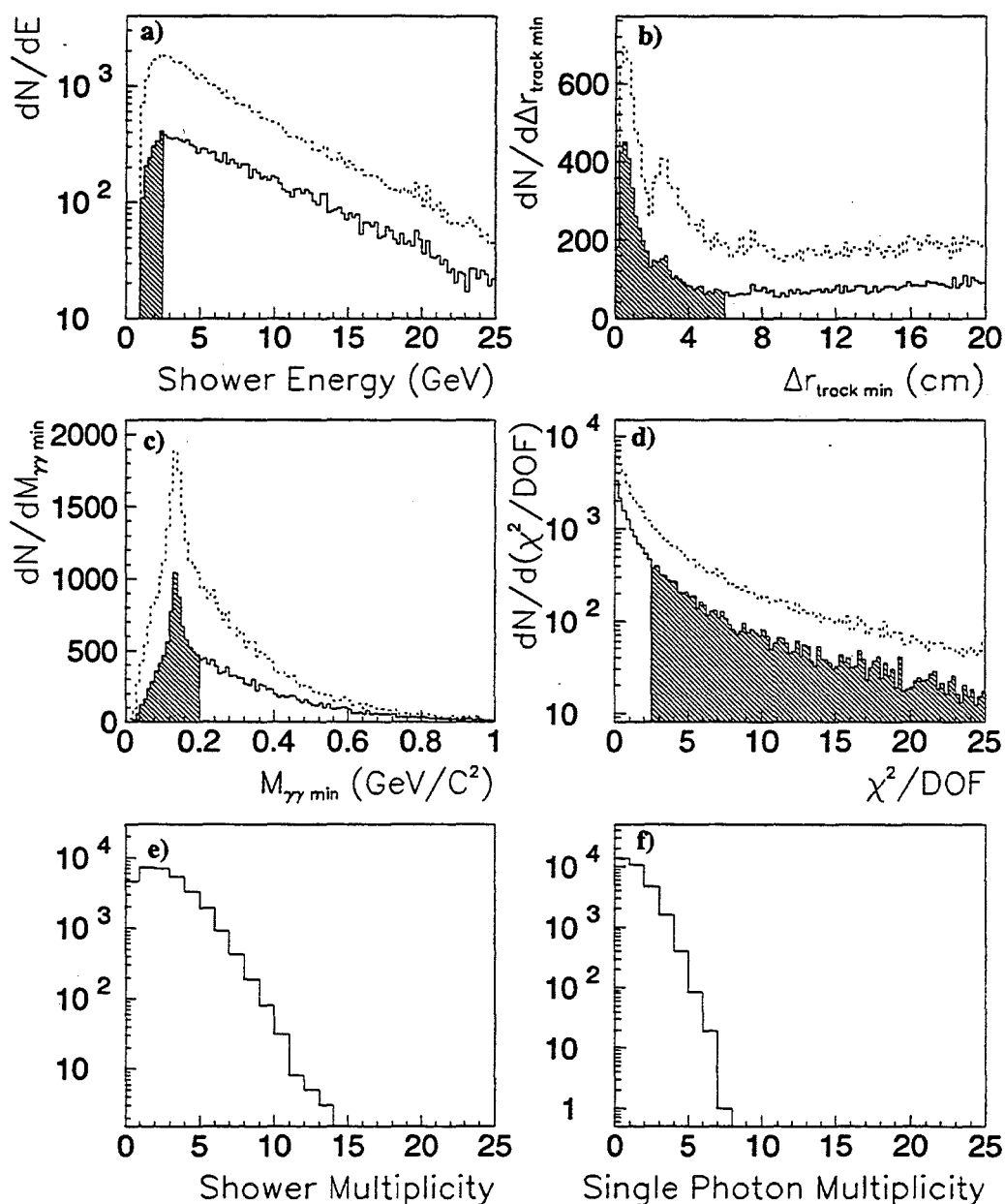


Figure 5.5: Photon cuts imposed on $J/\psi-\gamma$ mass spectrum. a) shower energy, b) radius to nearest track, c) minimum photon-photon invariant mass, d) chi squared of the shower. Dotted lines indicate the uncut, distributions for strict electromagnetic showers, while the shaded areas show the data excluded from the final $J/\psi-\gamma$ sample.

f. Figure 5.6 a show the the J/psi–shower mass difference distribution after the application of the single photon cuts. The single photon multiplicity and energy distributions are also given in figures 5.6 b and c.

5.3.1 Backgrounds

The background for chi states decaying into a J/psi and a photon fall into two categories based on how the psi and photon are related in the event. The first and dominant category is termed the *incoherent background* and is the result of electromagnetic showers in the calorimeter caused by particles which are loosely correlated with the J/psi. A shower in this category may come from one of several sources:

- A photon may come from a π^0 decay where one of the photons is lost, mismeasured or is not identified as electromagnetic.
- Photons may also stem from other neutral meson decays (η , η' and ω) which are unaccounted for.
- Electrons may be mismeasured, the shower position does not match the track position closely enough, or the associated track may not have been found.

The second category, *coherent background*, comes from highly correlated J/psi–photon combinations in which the J/psi and photon are part of the decay products of a more massive state, typically a psi prime meson.

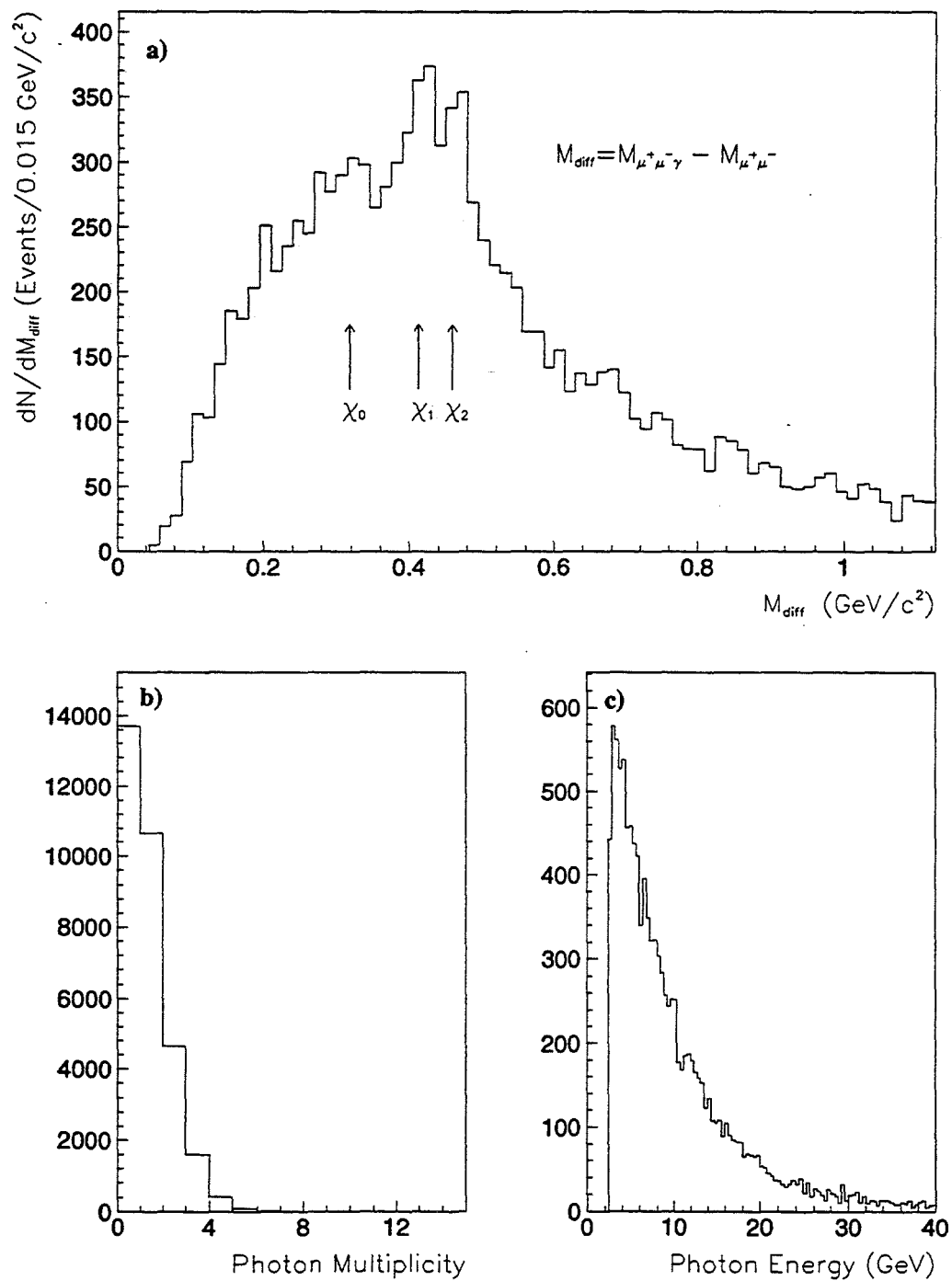


Figure 5.6: J/ψ -photon mass difference, photon multiplicity and photon energy spectra.

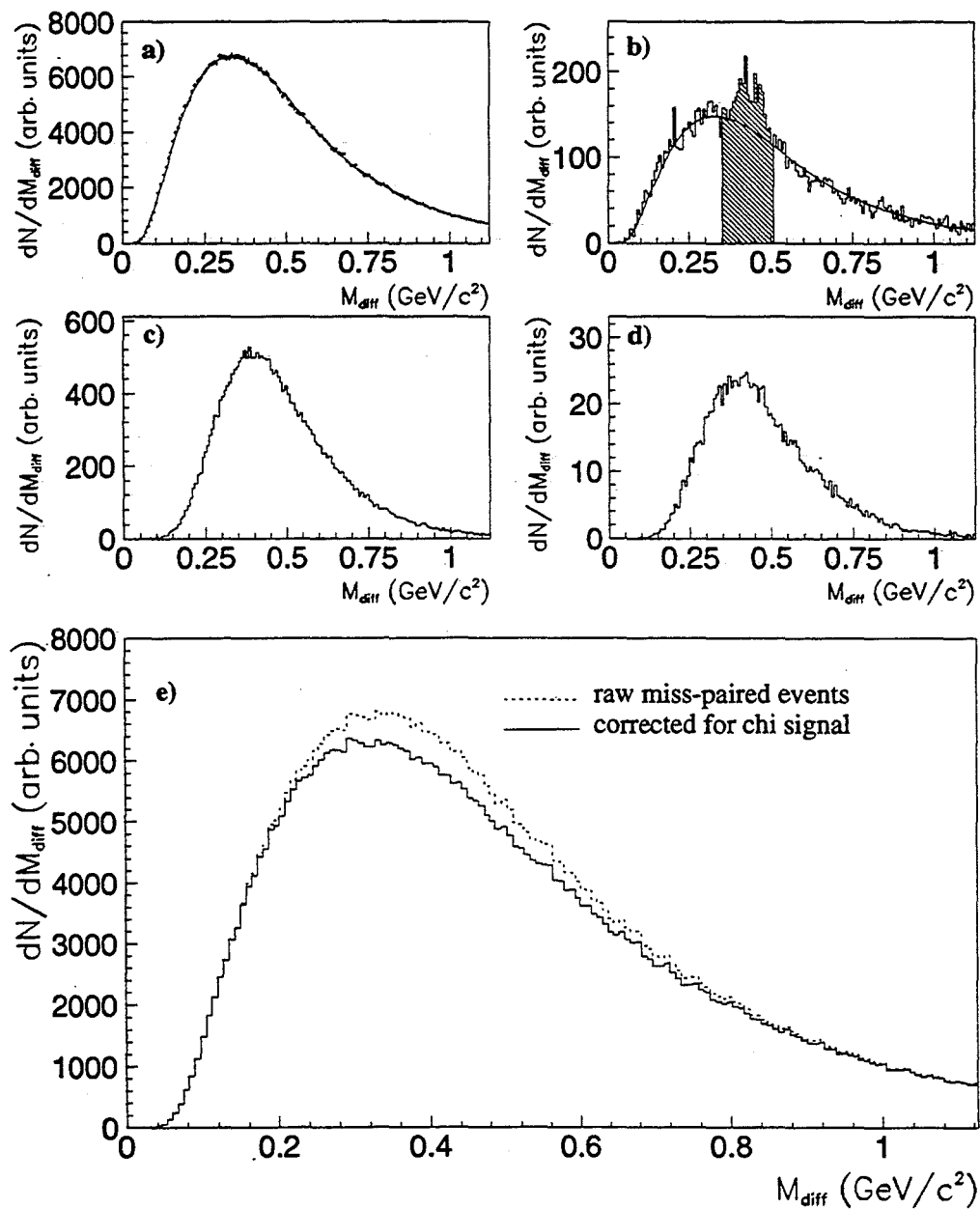


Figure 5.7: Background generated by cross-pairing events: a) raw cross-paired mass difference spectrum, b) data spectrum with raw cross-paired background normalized outside the hatched region, false backgrounds due to c) photons from χ decays and d) ψ s and photons from χ decays; d) comparison of corrected (solid line) and uncorrected (dotted line) backgrounds.

5.3.2 Incoherent Background (Cross Paired Events)

The shape of the incoherent portion of the dimuon-photon mass difference background spectrum was determined by cross or miss-pairing J/psis from one event with photons from another. The J/psis and photons used were from the sample of events that produced figure 5.6 where the psis and photons were paired only if they were produced by the same type of beam particle. Figure 5.7 a shows the mass difference spectrum generated in this manner.

Because some of the events on this plot come from real chi decays, there are false backgrounds due to the pairings of photons from chi decays with background psis and both psis and photons coming from chi decays. These two sources can not produce backgrounds in real events. To estimate these corrections, the probability that a J/psi-photon combination came from a chi decay:

$$P(M_{diff}) = \begin{cases} \frac{\#_{\chi s}}{\#_{\chi s} + \#_{background}} & 0.353 < M_{diff} < 0.503 \text{ GeV}/c^2 \\ 0 & \text{otherwise} \end{cases} \quad (5.3)$$

was determined using the background shape in figure 5.7 a normalized to the mass difference spectrum in figure 5.7 b outside the chi region defined in equation 5.3. Each photon forming a mass difference in the chi window was then weighted by the above probability and paired with unweighted J/psis from other events producing the mass difference spectrum in figure 5.7 c. Weighting the J/psis and pairing them with weighted photons from other events produced the spectrum in figure 5.7 d. A comparison of the corrected and uncorrected backgrounds is shown in figure 5.7 e.

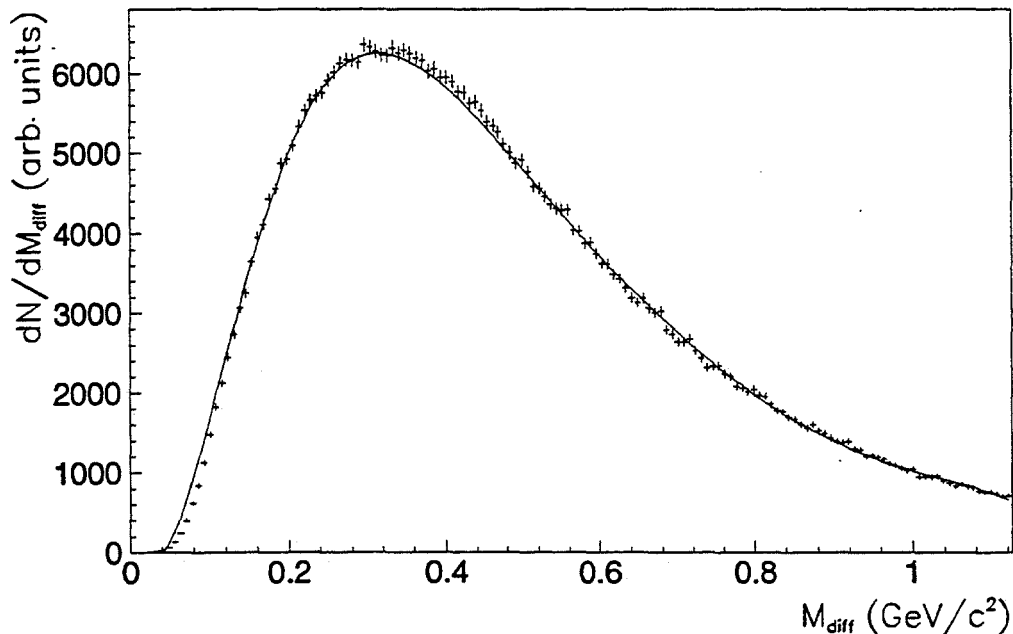


Figure 5.8: Fit to miss-paired background.

The resultant, corrected mass difference spectrum was then fit to a ninth-order polynomial to obtain a smooth shape for the incoherent portion of the background. The result of this fit is shown in figure 5.8.

5.3.3 Coherent Backgrounds

The coherent sources of backgrounds stem from the cascade decay of various mesons in which a J/ψ and a photon represent part of the cascade. Two primary sources of such backgrounds exist; the decay of B and ψ prime mesons.

We estimate the maximum possible contribution to the background in

the J/psi–photon mass difference spectrum due to B decays by making the generous assumption that the production cross section for B's is the same as that for psiprimes. The number of B mesons expected to decay into an observed J/psi (through the dimuon decay channel) is then given by [36]:

$$\#_{B \rightarrow \mu^+ \mu^- \gamma X} = \#_{\psi' \rightarrow \mu^+ \mu^-} \cdot \frac{A_\psi}{A_{\psi'}} \cdot \frac{\text{BR}_{B \rightarrow \mu^+ \mu^- \gamma X}}{\text{BR}_{\psi' \rightarrow \mu^+ \mu^-}}, \quad (5.4)$$

where the number of psiprimes decaying into muon pairs is given by table 5.3 and the relative acceptance for psiprimes compared with J/psi ($A_{\psi'}/A_\psi$) is 1.15 ± 0.03 [30]. The branching ratios for the two dominant decay modes for B mesons to produce a J/psi are: $\text{BR}_{B^0 \rightarrow \psi K^0} = (6.5 \pm 3.1) \times 10^{-4}$ and $\text{BR}_{B^+ \rightarrow \psi K^+} = (7.7 \pm 2.0) \times 10^{-4}$ [36]. The full decay sequences and their combined branching ratios are given below.

$$\begin{aligned} B^0 &\rightarrow \psi K^0 \rightarrow \mu^+ \mu^- 2\pi^0 \rightarrow \mu^+ \mu^- 4\gamma & (1.2 \pm 0.6) \times 10^{-5} \\ B^+ &\rightarrow \psi K^+ \rightarrow \mu^+ \mu^- \pi^+ \pi^0 \rightarrow \mu^+ \mu^- \pi^+ 2\gamma & (9.7 \pm 2.5) \times 10^{-6} \end{aligned} \quad (5.5)$$

The branching ratios for the kaon and pizero decays have also been taken from reference [36]. The combined branching fractions listed above are two orders of magnitude smaller than that for a psiprime decaying into muon pairs ($(7.7 \pm 1.7) \times 10^{-3}$ [36]). Using the combined branching ratios, the relative J/psi to psiprime acceptance and the psiprime branching ratio into equation 5.5 above, we should observe at most 0.4 ± 0.2 events from B^0 decays and 0.4 ± 0.1 events from B^+ decays in which the J/psi was reconstructed. Including the decays of the charge conjugate states only increases the number of expected decays by a factor of two. We may therefore neglect these contributions to the J/psi–photon backgrounds.

Table 5.4: Psiprime cascade decays producing a J/psi and photons.

Background Source	BR (%)	$A \cdot \epsilon_\gamma$ (%)
$\psi' \rightarrow \psi \pi^0 \pi^0$ $\hookrightarrow 4\gamma$	(18.4 ± 2.7) $(98.798 \pm 0.032)^2$ 18.0 ± 2.6	1.66
$\psi' \rightarrow \psi \eta$ $\hookrightarrow \gamma \gamma$	(2.7 ± 0.4) (38.9 ± 0.5) 1.05 ± 0.16	6.56
$\hookrightarrow \pi^0 \pi^0 \pi^0$ $\hookrightarrow 6\gamma$	(31.9 ± 0.4) $(98.789 \pm 0.032)^3$ 0.86 ± 0.13	1.09
$\hookrightarrow \pi^+ \pi^- \pi^0$ $\hookrightarrow \gamma\gamma$	(23.6 ± 0.6) (98.789 ± 0.032) 0.64 ± 0.10	0.54
$\psi' \rightarrow \gamma \chi_0$ $\hookrightarrow \psi \gamma$	(9.3 ± 0.8) (0.066 ± 0.018) 0.06 ± 0.02	2.11
$\psi' \rightarrow \gamma \chi_1$ $\hookrightarrow \psi \gamma$	(8.7 ± 0.8) (27.3 ± 1.6) 2.38 ± 0.26	0.63
$\psi' \rightarrow \gamma \chi_2$ $\hookrightarrow \psi \gamma$	(7.8 ± 0.8) (13.5 ± 1.1) 1.05 ± 0.12	0.18

The decay of psiprime mesons is the second source of coherent backgrounds which was considered. The dominant psiprime decay sequences which produce a J/psi and a photon are listed in table 5.4 along with the individual decay branching ratios in parantheses, and their combined branching ratios into $J/\psi \gamma X$ and the photon acceptance times reconstruction efficiency. The combined branching ratios were determined by multiplying

the published branching ratios for each of the decays in the sequence and propagating the uncertainties. The photon acceptance times reconstruction efficiency was determined using the Monte Carlo program described below by dividing the number of photons reconstructed by the number generated. The number of background events for a particular decay sequence is given by:

$$\#_{\psi' \rightarrow \mu^+ \mu^- \gamma X} = \#_{\psi' \rightarrow \mu^+ \mu^-} \cdot \frac{\text{BR}_{\psi' \rightarrow \psi \gamma X} \cdot \text{BR}_{\psi \rightarrow \mu^+ \mu^-}}{\text{BR}_{\psi' \rightarrow \mu^+ \mu^-}} \cdot \frac{A_{\psi}}{A'_{\psi}} \cdot (A \cdot \epsilon)_{\gamma} \cdot \#_{\gamma}. \quad (5.6)$$

The factor $\#_{\gamma}$ is the number of photons in the final state and is included because each photon may contribute to the J/psi-photon background. The branching ratio for the J/psi decaying into muon pairs is $(5.97 \pm 0.25)\%$ [36].

The photons reconstructed energy, multiplicity and J/psi-photon mass difference distributions along with the photon acceptance times reconstruction efficiency were all determined using a Monte Carlo program. The Monte Carlo program decayed psiprimes isotropically in their rest frame into a J/psi and photons via one of the modes listed above. All decay particles were boosted into the J/psi rest frame. A reconstructed J/psi was then read from a file of Monte Carlo dimuon from J/psi decays and the boost into the J/psi's rest frame was calculated. The photons from the psiprime decay were transformed into the lab frame using the boost parameters just calculated for the J/psi. In the lab frame, the photons were projected through the spectrometer and those hitting the calorimeter were smeared in position and energy using the same method described in the last chapter for the pizero Monte Carlo. Each photon was also assigned a random probability between zero

and one. If this probability was less than the reconstruction efficiency predicted for that photon, based on its location in the calorimeter and energy, the photon was considered reconstructed and a $J/\psi\gamma$ mass difference was calculated. Particulars for each psiprime decay mode are discussed in the following paragraphs.

$$\psi' \rightarrow \psi\pi^0\pi^0$$

The combined branching ratio for the psiprime to decay through the two pizero mode into a J/ψ and photons is 18.4 ± 2.7 %. Both pizeros were assumed to decay via their two photon mode ($BR_{\pi^0 \rightarrow \gamma\gamma} = 98.789 \pm 0.032$ %) [36] when calculating the combined branching ratio. Combining the number of psiprimes from table 5.1 the combined branching ratio and photon acceptance times reconstruction efficiency from table 5.4 with the J/ψ branching ratio to muons and the photon multiplicity of four into equation 5.6 gives 39 ± 13 expected background events for this decay mode. The reconstructed photon multiplicity, energy and J/ψ -photon mass difference spectra are shown in figure 5.9.

$$\psi' \rightarrow \psi\eta$$

The eta meson has several decay modes which contribute a photon to the J/ψ -photon background. However, we considered only the three decay sequences which have the largest branching ratios: $BR_{\eta \rightarrow \gamma\gamma} = (38.9 \pm 0.5)\%$, $BR_{\eta \rightarrow 3\pi^0} = (31.9 \pm 0.4)\%$ for the two neutral decay modes and $BR_{\eta \rightarrow \pi^+\pi^-\pi^0} =$

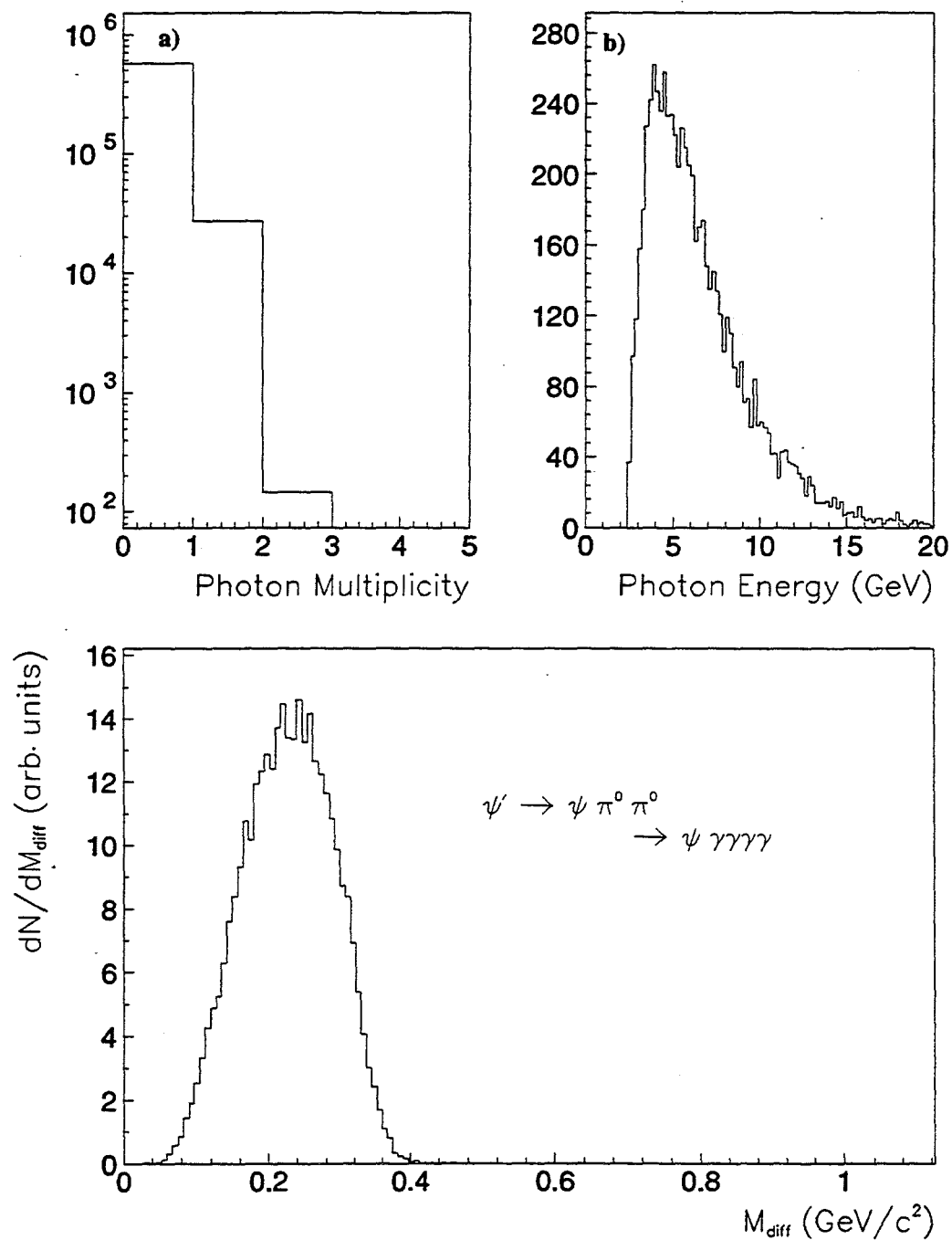


Figure 5.9: Photon multiplicity, energy and $\psi\gamma$ mass difference spectra for $\psi' \rightarrow \psi \pi^0 \pi^0$ decays.

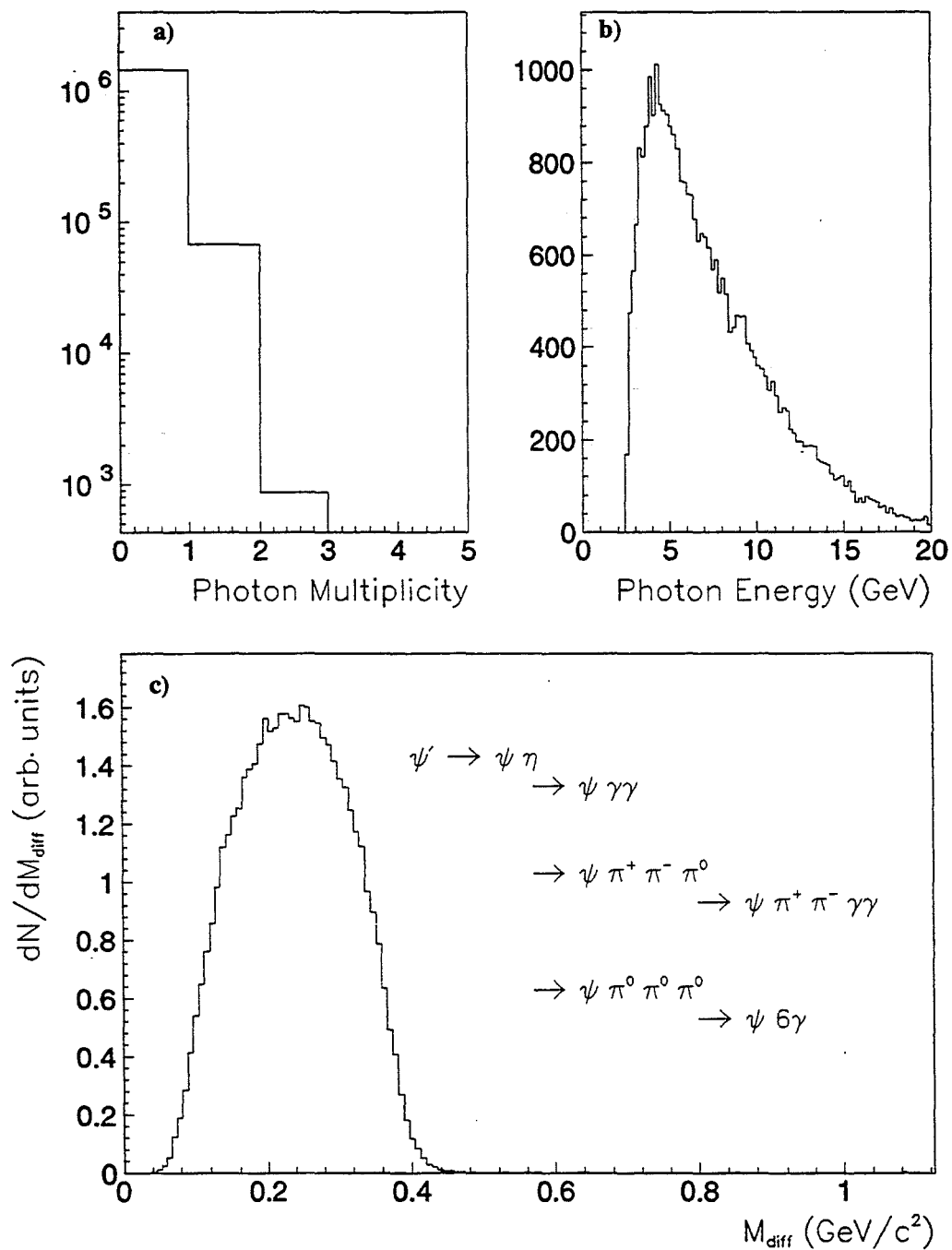


Figure 5.10: Photon multiplicity, energy and $\psi\gamma$ mass difference spectra for $\psi' \rightarrow \psi\eta$ decays.

(23.6 ± 0.6)% [36] for a charged decay mode. The pizeros were assumed to decay into their two photon modes only for the last two decay modes. Each eta decay mode was simulated separately, but all were combined to produce the photon multiplicity, energy and J/psi-photon mass difference spectra shown in figure 5.10. The low photon multiplicity comes about from the minimum photon energy requirement and the low reconstruction efficiency at low photon energies. The expected number of background entries for $\eta \rightarrow \gamma\gamma$, $\eta \rightarrow 3\pi^0 \rightarrow 6\gamma$ and $\eta \rightarrow \pi^+\pi^-\pi^0 \rightarrow \pi^+\pi^-2\gamma$ are 4.4 ± 1.6 , 1.6 ± 0.6 and 0.22 ± 0.08 , respectively.

The other eta decay modes only produce a single photon in the final state and have significantly smaller branching ratios ($\text{BR}_{\eta \rightarrow \pi^+\pi^-\gamma} = (4.88 \pm 0.15)\%$, $\text{BR}_{\eta \rightarrow e^+e^-\gamma} = (5.0 \pm 1.2) \times 10^{-3}$ and $\text{BR}_{\eta \rightarrow \mu^+\mu^-\gamma} = (3.1 \pm 0.4) \times 10^{-4}$ [36]). These two factors lead us to estimate their contributions to be less than one background event on our total sample for each decay mode.

$$\psi' \rightarrow \chi_j \gamma$$

For the above decay mode, the chi states are produced and subsequently decayed but the J/psi is paired with the photon from the radiative decay of the psiprime. The Branching ratios for the pprime to decay into each of the chi states are $(9.3 \pm 0.8)\%$, $(8.7 \pm 0.8)\%$ and $(7.8 \pm 0.8)\%$ for the $j=0,1,2$ chi states, respectively. The branching ratios for the subsequent chi decays are $(6.6 \pm 1.8) \times 10^{-3}$, $(27.3 \pm 1.6)\%$ and $(13.5 \pm 1.1)\%$ for the $j=0,1,2$ states, respectively. Each of these decays was simulated separately, but

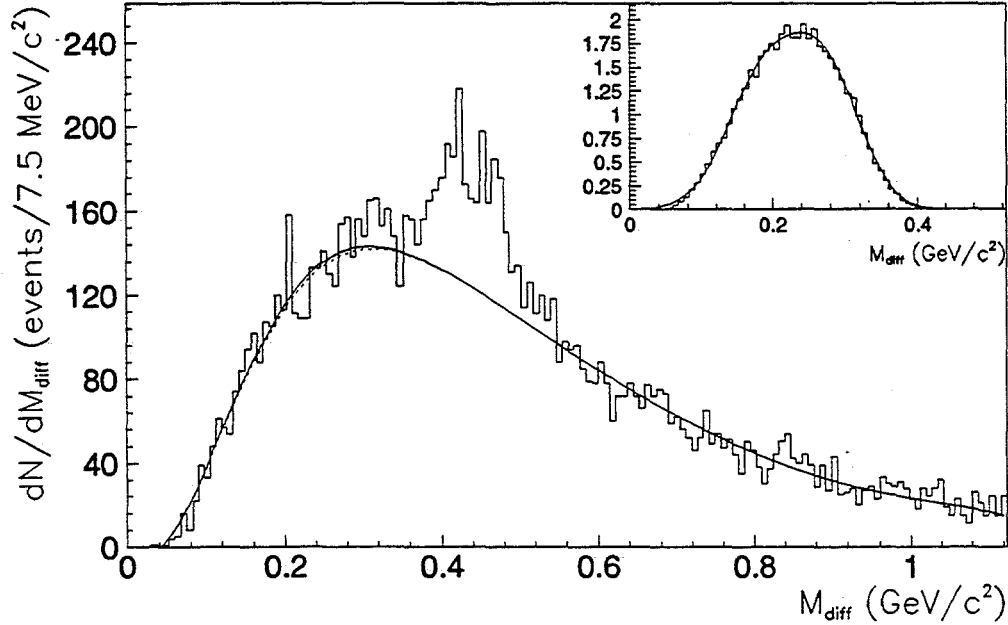


Figure 5.11: $\psi\gamma$ mass difference spectrum with overlaid backgrounds. Solid line is the total background, dotted line is the contribution from mispaired events. Inset shows the coherent backgrounds.

their photon multiplicity, energy and mass difference spectra are combined in figure 5.10. The expected number of background events for each decay mode are (0.041 ± 0.019) , (0.458 ± 0.16) and (0.061 ± 0.02) , respectively. Because less than one background event is expected for these decays they have not been included in the coherent background.

The total background contribution due to coherent sources was arrived at by normalizing the J/ψ -photon mass difference spectra for the $J/\psi\pi^0\pi^0$ and $J/\psi\eta$ psiprime decay modes to the number of expected background events. These spectra were added together and the resultant distribution was fit to

two Gaussians. The background from coherent sources and the two Gaussian fit is shown in the inset of figure 5.11. Using functional forms for the backgrounds allows us to use a binless fitting procedure when later fitting for the chi signals. The total background from coherent and mispaired events is shown as the solid line overlaid on our signal in the same figure. The dotted line represents the contribution due to mispaired events. In this plot, the normalization, a , for the mispaired background, $B_{\text{mispair}}(m)$, was determined by minimizing the chi squared:

$$\chi^2 = \sum_i^{\text{bins}} \left(\frac{D(m_i) - aB_{\text{mispair}}(m_i) - B_{\psi'}(m_i)}{\sigma(m_i)} \right)^2, \quad (5.7)$$

where $D(m_i)$, $B_{\text{mispair}}(m_i)$ and $B_{\psi'}(m_i)$ are the number of events in the data, mispaired and coherent backgrounds for mass difference bin m_i . The normalization was performed outside the chi region previously defined.

Chapter 6

Results and Conclusions

The previous two chapters presented the methods and selection criteria used to arrive at our final sample of J/psi-photon events. In the last chapter, the sources of backgrounds for this sample was also examined. However, to do any physics, different aspects of the reconstruction process need to be well understood. In the sections below, the methods used to determine the final number of chis observed and the efficiency of finding them are discussed. Both total and differential cross sections are calculated for the chi states and compared with other experiments. Decay angular distributions are also presented. Finally, the results of this experiment are summarized and a short discussion of the physics implications of these results are presented.

6.1 Chi Monte Carlo

A Monte Carlo program was used to determine the chi photon acceptance and reconstruction efficiency along with the expected mass difference resolution of the different chi states. This program generated chis in the relative abundance of their published branching ratios, 0.66 : 27.3 : 13.5 [36], using

Table 6.1: J/psi kinematic distribution parameters.

Beam Type	x_0	a	$\langle p_T \rangle^2$ (GeV ² /c ⁴)
pion	0.035	2.24	1.475
proton	0.028	4.73	1.311

our measured J/psi Feynman x and transverse momentum distributions:

$$\frac{d\sigma}{dx_F} \propto (1 - |x_F - x_0|)^c \quad (6.1)$$

$$\frac{d\sigma}{dp_T} \propto p_T e^{-\frac{p_T^2}{\langle p_T \rangle^2}}, \quad (6.2)$$

The parameters for the above distributions are from reference [29] and are summarized in table 6.1.

The generated chi was decayed isotropically in its rest frame into a J/psi and a photon. The J/psi was subsequently decayed into opposite sign dimuons with a $1 + \cos^2 \theta_{\mu^+}$ distribution, where the angle θ_{μ^+} is the angle between the beam direction and the positive muon momentum vector in the J/psi's rest frame. All the decay products were then boosted into the lab frame and projected through the spectrometer using the vertex from a real dimuon event. Muons hitting the wire chambers had their position smeared and the hit efficiency folded in using the information from chapter 3. The generated event was then overlaid onto the real dimuon event from which the vertex came. The chamber and counter hits along with the trigger information from the triggering dimuons were removed from the real event so as to avoid possible conflicts in the reconstruction. The event made up from the

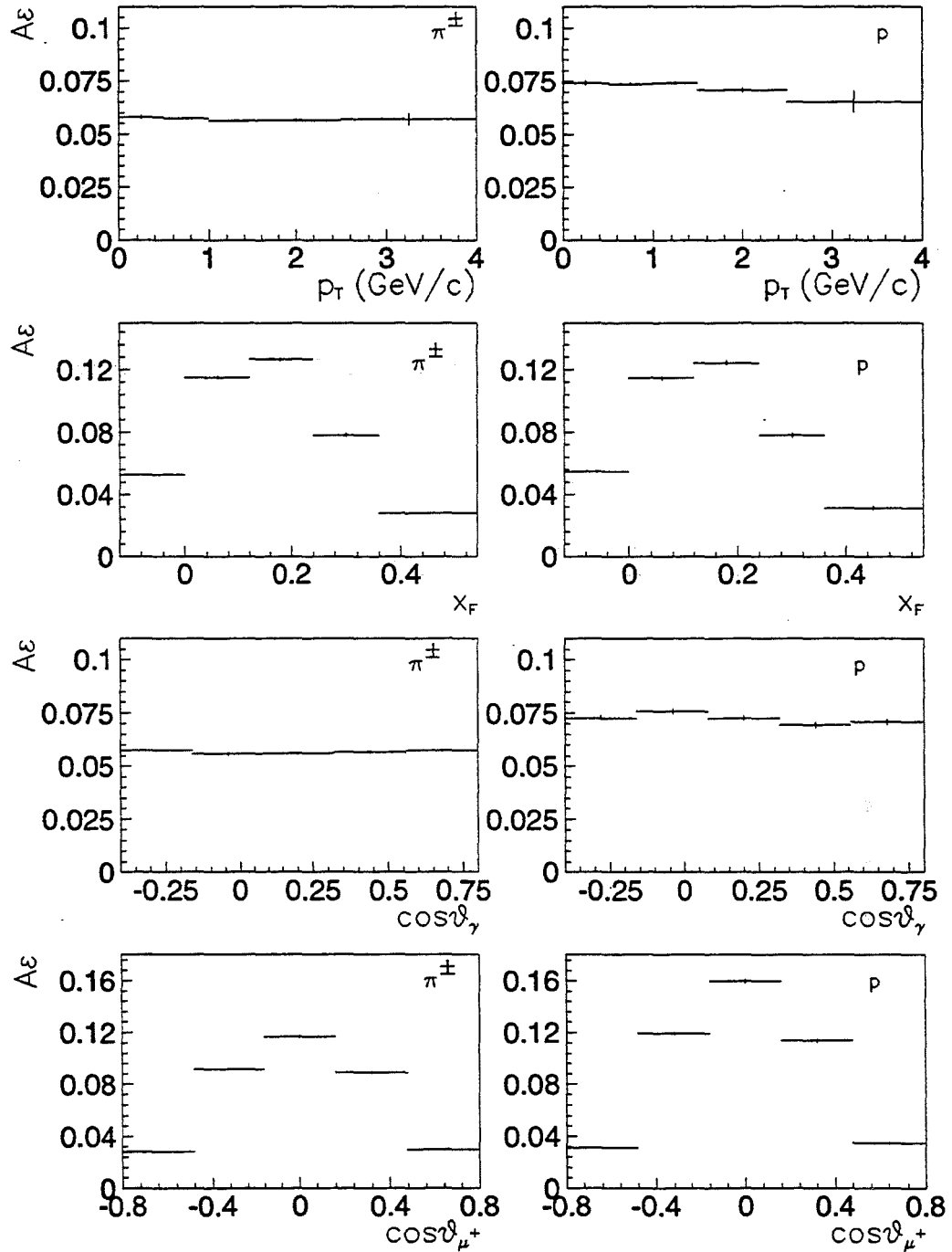


Figure 6.1: J/ψ acceptance times reconstruction efficiency for pion and proton beam as a function of four chi kinematic variables: p_T , x_F , $\cos\vartheta_\gamma$ and $\cos\vartheta_{\mu^+}$.

Monte Carlo chi and the real dimuon trigger was then treated as a real event and run through the filter, track reconstruction and pass II programs. Only events passing the requirements of all of these programs were kept. These events were subsequently used to determine the experiment's resolution, acceptance and reconstruction efficiency for the J/psi. The J/psi resolution was found to agree with the data (see the previous chapter). The acceptance times reconstruction efficiency for the J/psis are shown in figure 6.1 as a function of the kinematic variables for the J/psi-photon system: x_F , p_T , $\cos\theta_\gamma$ and $\cos\theta_{\mu^+}$ where the angles θ_γ and θ_{μ^+} are the angles between the beam direction and the photon and positive muon in the J/psi-photon center of mass frame, respectively. For more information on this aspect of the Monte Carlo program the reader is referred to references [28, 29, 30].

6.1.1 Photon Acceptance and Reconstruction Efficiency

The Monte Carlo chi photons were projected through the spectrometer and those hitting a live region of the calorimeter with more than 2.5 GeV energy were considered accepted. The photon acceptance was then calculated as the number of photons accepted divided by the number of J/psis reconstructed (each J/psi was associated with a photon). The overall chi photon acceptance was determined using this method to be $62.15 \pm 0.61\%$ for the pion beams and $61.89 \pm 0.69\%$ for the proton beam. The acceptance was also determined as a function of four kinematic variables for the J/psi-photon system: x_F , p_T , $\cos\theta_\gamma$ and $\cos\theta_{\mu^+}$. Figure 6.2 shows the acceptance for pion and proton

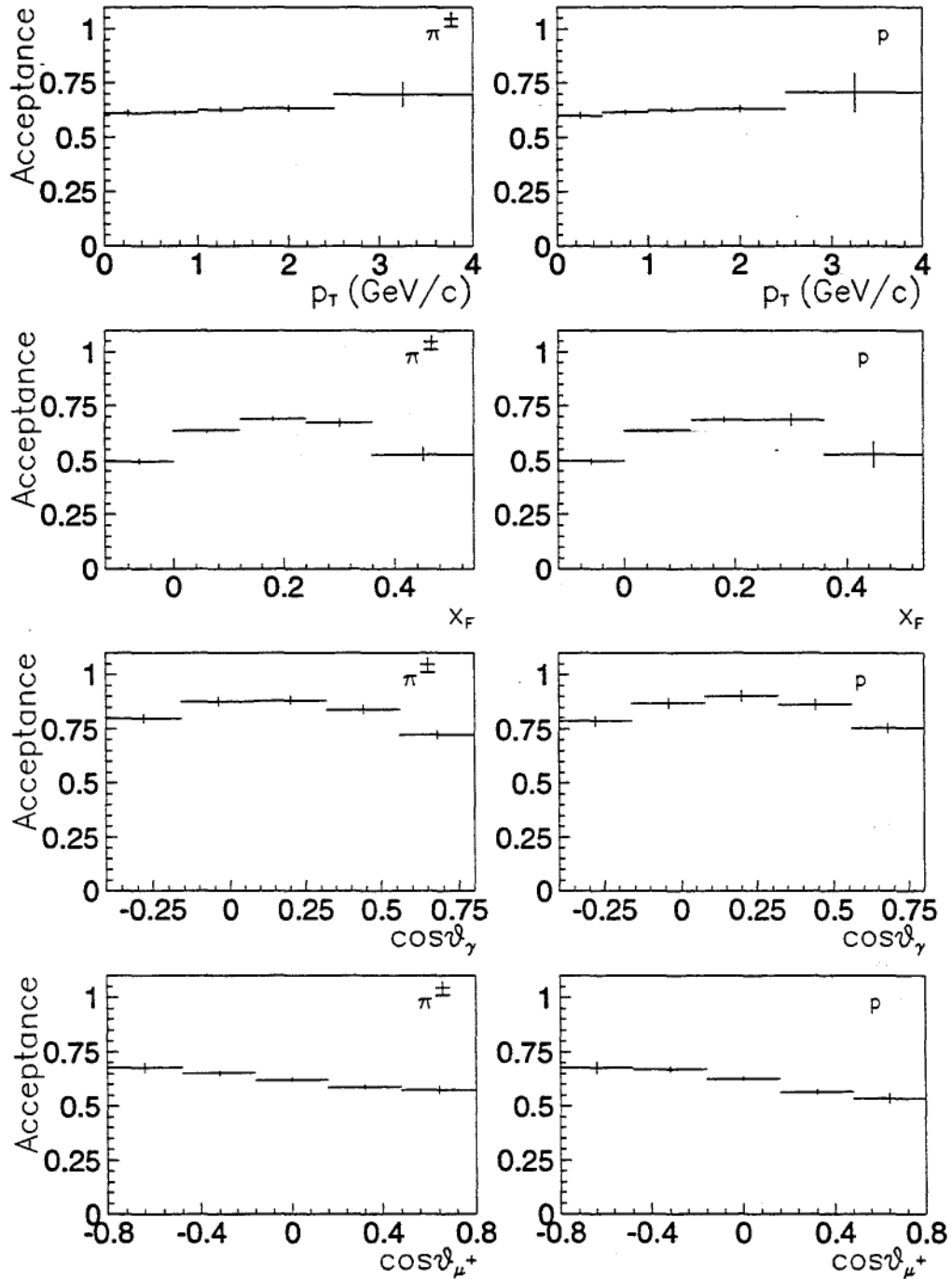


Figure 6.2: Chi photon acceptance for pion and proton beams as a function of four kinematic variables: p_T , x_F , $\cos\theta_\gamma$ and $\cos\theta_{\mu^+}$.

beam types for the above variables.

Accepted photons were smeared in position and energy using the prescriptions discussed in chapter 4. The photon reconstruction efficiency was folded in using the method described in the previous chapter. To reduce statistical effects this was repeated ten times for each accepted photon. These photons were then combined with reconstructed photons from a real J/psi event and the minimum photon-photon mass was calculated. Monte Carlo chi photons were considered reconstructed if their reconstruction probability satisfied the requirements discussed in the previous chapter and their minimum photon-photon invariant mass was greater than $200 \text{ MeV}/c^2$. The reconstruction efficiency was then determined by dividing the number of reconstructed photons by the number of photons accepted. The overall reconstruction efficiency was determined using this method to be $16.76 \pm 0.07\%$ for the pion beams and $16.89 \pm 0.09\%$ for the proton beam. The photon reconstruction efficiency was also determined for the four kinematic variables discussed in the previous paragraph and are shown in figure 6.3.

6.1.2 Chi Resolution Functions

Our experiment's resolution for the chi states was determined by forming the mass difference using the reconstructed J/psi and photons from the Monte Carlo sample used to determine the chi reconstruction efficiency. The mass difference spectrum for each chi state was then plotted separately and fit to a Gaussian. The results of the fits gave $29.91 \pm 0.08 \text{ MeV}/c^2$ and

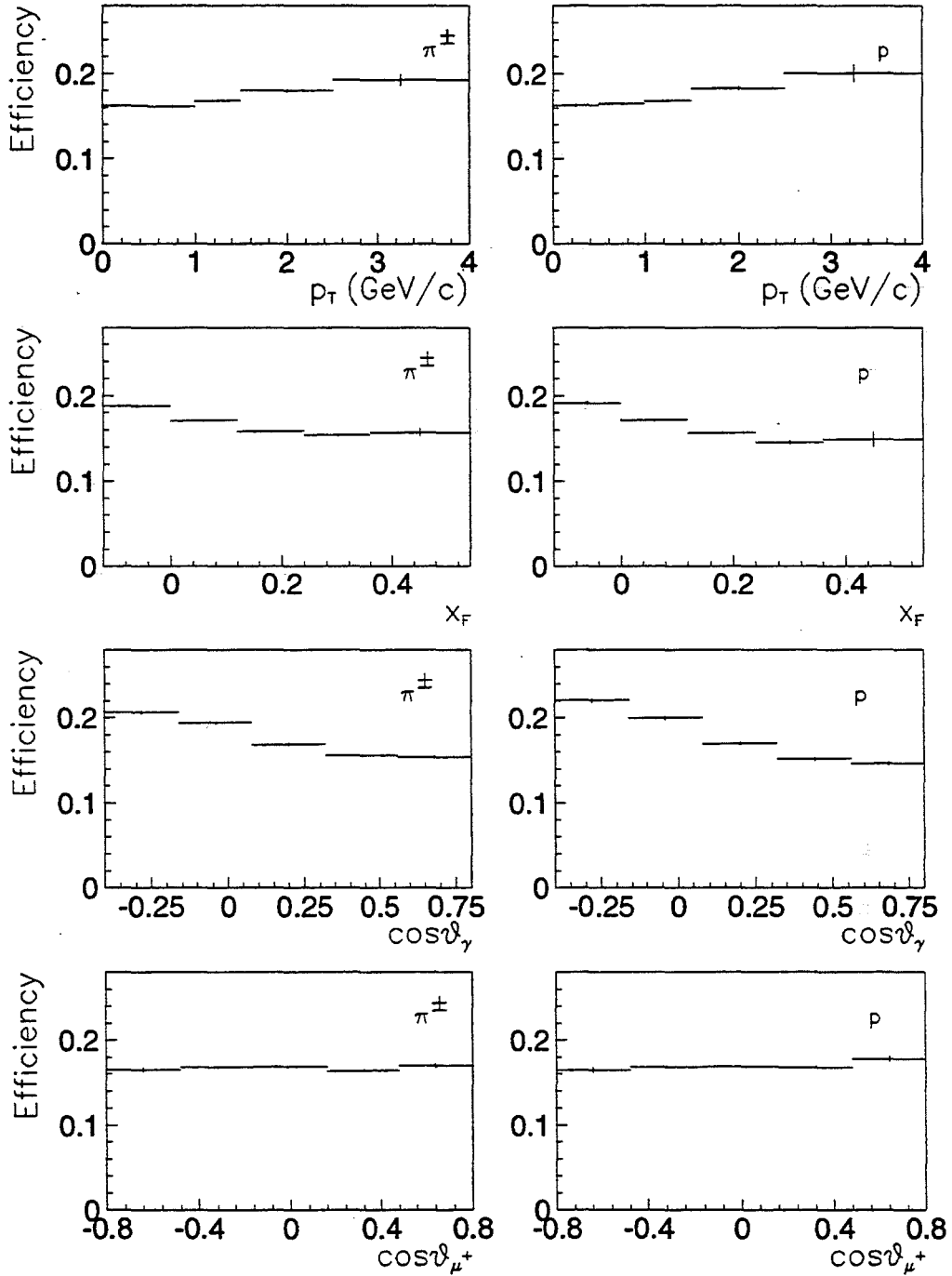


Figure 6.3: Chi photon reconstruction efficiency for pion and proton beams for four kinematic variables, p_T , x_F , $\cos\theta_\gamma$ and $\cos\theta_{\mu^+}$.

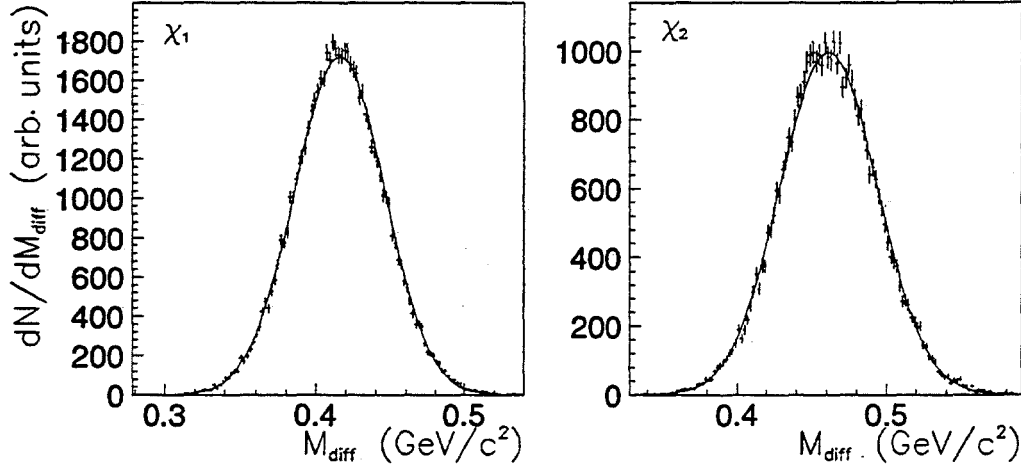


Figure 6.4: χ_1 and χ_2 resolution functions.

$32.48 \pm 0.12 \text{ MeV}/c^2$ for the $J=1,2$ chi states, respectively. The mass difference spectra and fits for these states are shown in figure 6.4.

The $J=0$ chi state has an extremely small, measured branching ratio into its radiative decay mode ($\text{BR}_{\chi_0 \rightarrow \psi \gamma} = 0.66 \pm 0.18\%$ [36]). Assuming equal production of the three chi states, we would expect to see only 9 radiative decay events from the $J=0$ chi state. Even if the recent theoretical predictions of a two percent branching ratio [39] are realized by experiment, we estimate that only 27 radiative decays of the $J=0$ chi state would be observed.

The dependence of the mass difference on the photon energy scale was also determined for the $J=1,2$ chi states. Monte Carlo photons from the reconstructed sample were multiplied by a factor, a , varying between 0.95–1.05 (corresponding to a change in the energy scale of $\pm 5\%$). The rescaled photons were then combined with the J/ψ in the same event and the mass

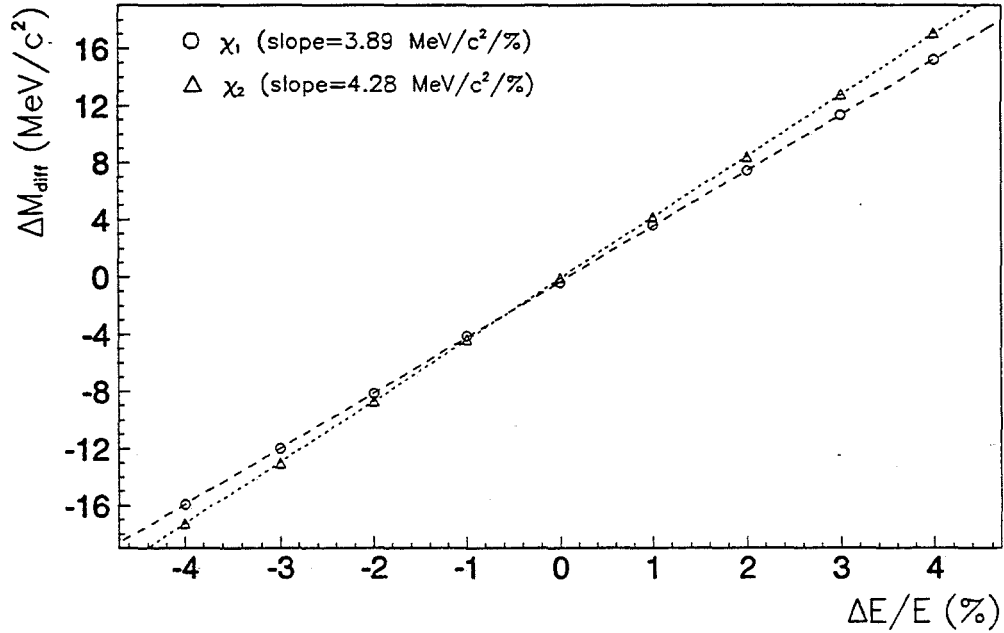


Figure 6.5: Mass shift versus fractional change in the photon energy scale.

difference was calculated. The mean of each resulting mass difference spectrum was determined by fitting to a Gaussian. Figure 6.5 shows the shift in the mean mass difference, ΔM_{diff} , as a function of the fraction change in the photon energy:

$$\frac{\Delta E}{E} = \frac{aE - E}{E} = a - 1, \quad (6.3)$$

where E is the true photon energy. This information, in conjunction with our estimate of the energy scale variation was used as a constraint when fitting for the abundances of the two chi states.

6.2 Fitting for the Chi Signals

In order to determine the relative production ratios for the two chi states and their production cross sections, the number of chis observed in each state had to be determined N_{χ_1} and N_{χ_2} . This was accomplished by performing a fit to the entire data sample, simultaneously determining parameters for different beam types. A three beam type fit determined fit parameters seperately for both charges of pion beams and the proton beam, while the two beam type fit combined the two charges of pion beam. The two pion beams could be combined due to the nearly isoscaler nature of the ${}^7\text{Li}$ target. The fit was performed using a modified version of the extended maximum likelihood method [38] outlined below.

6.2.1 Fit Procedure

Each observed J/psi-photon combination i of beam type j in the mass difference range

$$0.060 < M_{diff} < 1.125 \text{ GeV}/c^2 \quad (6.4)$$

was assigned a probability or likelihood, $\ell_{i,j}$, that it would occur in our data sample. The likelihood for each event was given by:

$$\ell_{i,j} = \frac{1}{N_f} \left\{ N_{\chi_1,j} S_{\chi_1}(m_{i,j} + \delta m) + N_{\chi_2,j} S_{\chi_2}(m_{i,j} + \delta m) + N_{B,j} B_{mispair}(m_{i,j}) + N_{b,j}^{\psi'} B_{\psi'}(m_{i,j}) \right\}, \quad (6.5)$$

where S_{χ_1} , S_{χ_2} , $B_{mispair}$ and $B_{\psi'}$ are the normalized shapes of the J=1,2 chi states and the mispaired and coherent backgrounds, respectively. Each

shape is a function of the mass difference denoted m here for simplicity. The chi resolution functions are allowed to shift their central mass difference by an amount δm which is a parameter optimized by the fit. The scale factors, $N_{\chi_{1,j}}$, $N_{\chi_{2,j}}$ and $N_{B,j}$, are the numbers of the $J=1,2$ chi states and mispaired background combinations for beam type j , respectively and are parameters which the fit optimized. The last scale factor, $N_{b,j}^{\psi'}$, is the number of coherent background combinations from psi prime decays for beam type j . This variable was fixed to the number of combinations expected to be observed for a particular beam type and was determined by scaling the total number of expected coherent background combinations for the whole data sample by the proportion of psi primes observed in that beam type relative to the total number observed (see table 5.1). The normalization for the likelihood function is calculated from the fit parameters:

$$N_f = \sum_{j=1}^{N_{beam}} (N_{\chi_{1,j}} + N_{\chi_{2,j}} + N_{B,j}). \quad (6.6)$$

The probability that an experiment of N_e observed combinations was performed with a given set of parameters is given by:

$$\mathcal{L} = \frac{e^{-\frac{\delta m^2}{2\sigma_m^2}}}{\sqrt{2\pi}\sigma_m} \left\{ \frac{N_f^{N_e} e^{-N_f}}{N_e!} \prod_{j=1}^{N_{beam}} \prod_{i=1}^{N_j} \ell_{i,j} \right\}, \quad (6.7)$$

where the products are over the N_j events of beam type j and the N_{beam} beam types. The terms of the above equation in the braces are just the extended likelihood function where the Poisson term preceding the products allows the normalization, N_f to be a fit parameter. The term in front of the

braces is a Gaussian constraining the amount δm is allowed to vary or how much the mass difference is allowed to shift for the chi peaks. The constant σ_m defines the amount of mass shift allowed and was set to $6.0 \text{ MeV}/c^2$ which corresponds to an energy scale shift of 1.5%. The relative separation between the two higher mass chi states was fixed at $45 \text{ MeV}/c^2$, the nominal mass difference separation for the two higher mass chi states.

The principle of maximum likelihood states that the parameters which maximize the total likelihood, \mathcal{L} , or equivalently, minimize the negative log of the total likelihood, are those which the data is best matches. Taking the logarithm of equation 6.7, making the assumption that $N_e \log N_f$ is a constant, and throwing away constant terms one arrives at:

$$-\log \mathcal{L} = N_f + \frac{1}{2} \left(\frac{\delta m}{\sigma_m} \right)^2 - \sum_{j=1}^{N_{beam}} \sum_{i=1}^{N_j} \log \ell_{i,j}, \quad (6.8)$$

where the sums are over the the N_j combinations of the N_{beam} different beam types. The above function was minimized with respect to the parameters $N_{\chi_1,j}$, $N_{\chi_2,j}$, $N_{B,j}$ and δm using the MINUIT function minimization package [40].

6.2.2 N_{χ_1} , N_{χ_2} Parameterization of the Chi Signal

The results of the fits for the two and three beam type fits are shown in figures 6.6 and 6.7 and table 6.2. Parameters from the two and three beam type fits for the proton beam were the same and only one is given. Correlation coefficients among the number of chis in the two higher mass states (N_{χ_1} , N_{χ_2}) and the mass shift (δm) are also given in the same table.

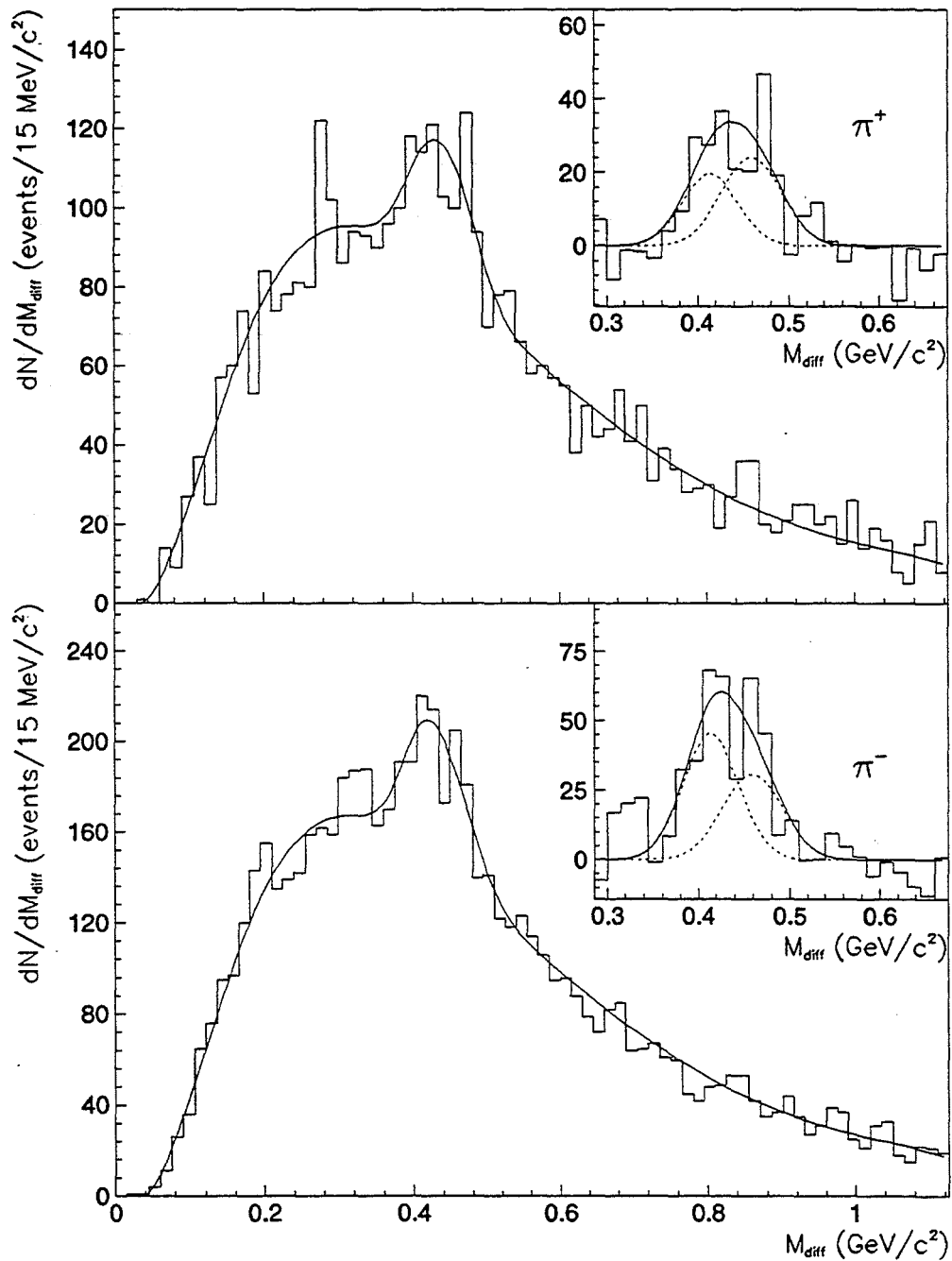


Figure 6.6: Mass difference spectra for π^+ and π^- data. The solid lines are from the fit described in the text.

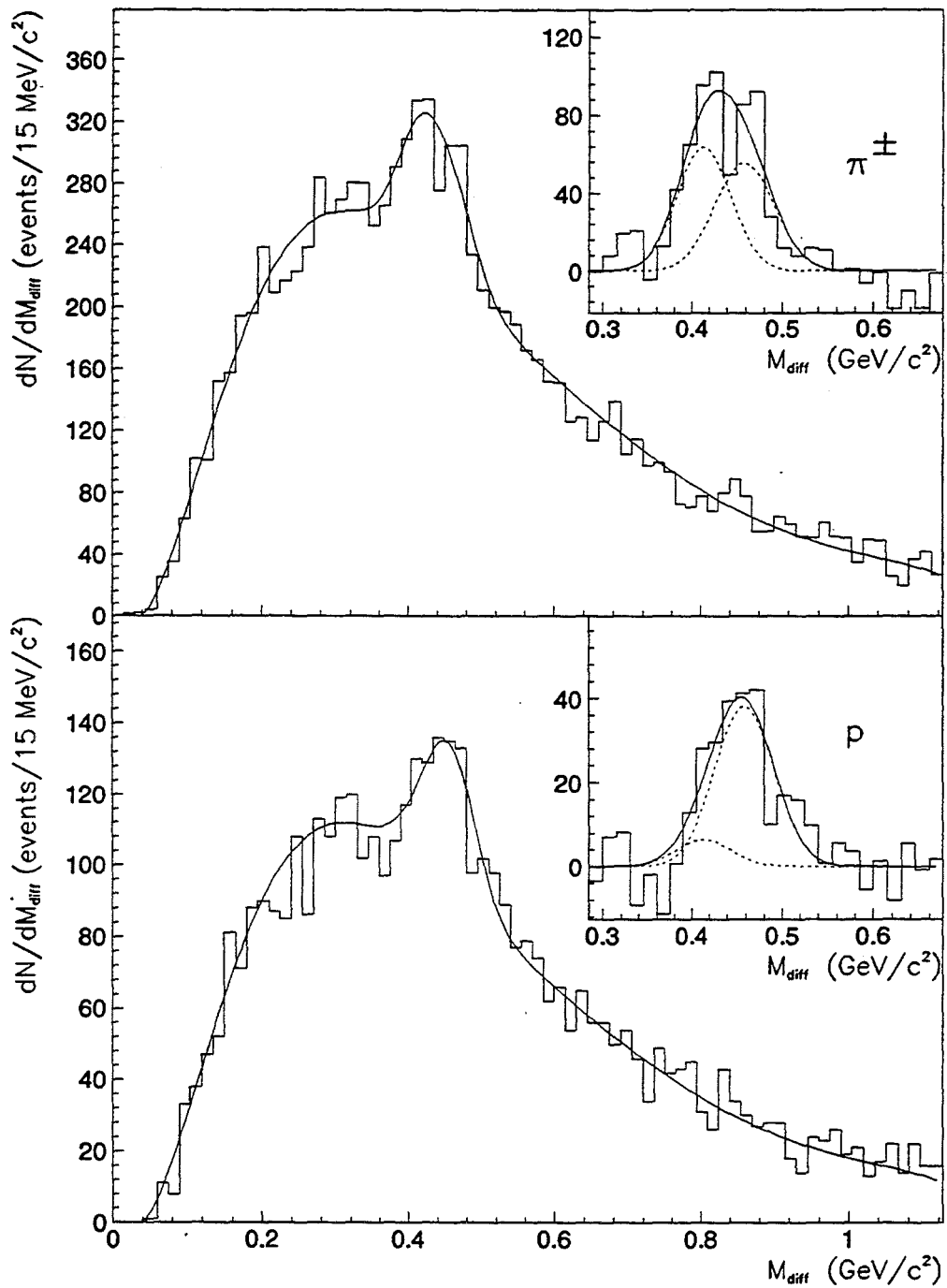


Figure 6.7: Mass difference spectra for π^\pm and proton data. The solid lines are from the fit described in the text.

Table 6.2: Chi fit results; χ_1 , χ_2 parameterization.

Beam Type	# χ_1		# χ_2		Correlation Coefficients		
					(χ_1, χ_2)	$(\chi_1, \delta M)$	$(\chi_2, \delta M)$
π^+	100	+58	132	-0.604	-0.486	0.465	
		-57					
π^-	231	+84	169	-0.701	-0.611	0.671	
		-87					
π^\pm (combined)	326	+114	307	-0.745	-0.692	0.717	
		-119					
p	36	+71	208	-0.661	-0.656	0.504	
		-70					

6.2.3 T , R_{12} Parameterization of the Chi Signal

Because the large correlation between the fitted number of the $J=1$ and $J=2$ chi states, and our desire to obtain the relative abundances of the produced chis, the variables in the fit parameterizing the chi signal were changed to:

$$T_j = N_{\chi_1,j} + N_{\chi_2,j} \quad (6.9)$$

$$R_{12,j} = \frac{N_{\chi_1,j}}{N_{\chi_2,j}}. \quad (6.10)$$

This re-parameterization of the fit variables more nearly diagonalized the error matrix. The results of the two and three beam type fits are given in table 6.3 along with the correlation coefficients among the variables T , R_{12} and δm . The value of R_{12} has been measured by other experiments and

Table 6.3: Chi fit results; T , R_{12} parameterization.

Beam Type	T	R_{12}	Correlation Coefficients		
			(T, R_{12})	$(T, \delta M)$	$(R_{12}, \delta M)$
π^+	+51	+1.11	0.052	-0.013	-0.507
	231	0.76			
π^-	-50	-0.51	-0.060	0.118	-0.676
	401	1.37			
π^\pm (combined)	+68	+2.26	-0.064	0.071	-0.743
	632	1.06			
p	-66	-0.78	0.142	-0.209	-0.640
	244	0.17			
	+56	+0.51			
	-55	-0.31			

is independent of branching ratios and other systematic errors. Figure 6.8 plots the E705 R_{12} results with those of other experiments as a function of the center of mass energy \sqrt{s} .

Ratios of the chi production cross sections are obtained by multiplying the observed ratios of the chi states, R_{12} , by the ratio of the branching fractions for radiative chi decay:

$$\frac{\sigma_{\chi_1}}{\sigma_{\chi_2}} = R_{12} \frac{\text{BR}_{\chi_2 \rightarrow \psi \gamma}}{\text{BR}_{\chi_1 \rightarrow \psi \gamma}} \quad (6.11)$$

The results in table 6.3 were used to calculate the chi production ratios for this experiment which are listed in table 6.4 by beam type.

All the experiments quoted above used nearly isoscaler targets (Be, Li), therefore, these data may be combined to get a world averages for the ob-

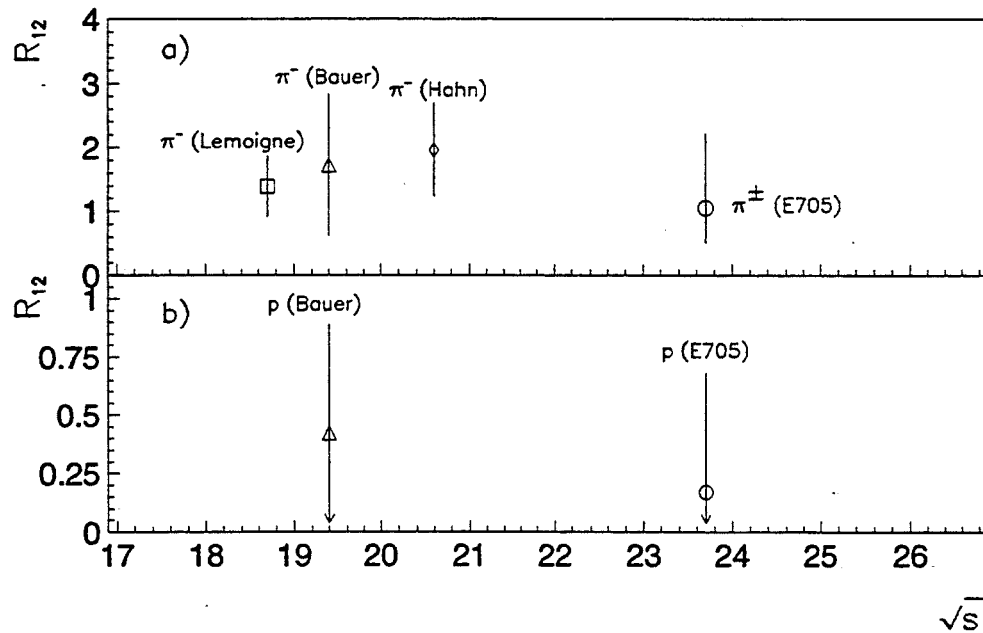


Figure 6.8: R_{12} compared with other experiments for a) pion and b) proton beams. The data from other experiments come from references (Bauer) [10], (Lemoigne) [12] and (Hahn) [13].

served chi ratio and the produced chi ratio. Using the ratio of observed chis R_{12} for our combined pion $(1.06 \pm 0.72)^*$ and proton $(0.17 \pm 0.36)^*$ the world average for the observed ratios and the production ratios for the two higher mass chi states were found to be 1.47 ± 0.33 and 0.73 ± 0.18 for pion induced reactions, respectively, and 0.26 ± 0.28 and 0.13 ± 0.14 for proton induced reactions, respectively.

*The symmetric errors quoted are those returned by MINUIT from the fit.

Table 6.4: E705 ratios of chi production cross sections by beam type.

$\sigma_{\chi_1}/\sigma_{\chi_2}$ by Beam Type			
π^+	π^-	π^\pm	proton
0.38 $^{+0.55}_{-0.26}$	0.68 $^{+1.12}_{-0.39}$	0.52 $^{+0.58}_{-0.28}$	0.08 $^{+0.25}_{-0.15}$

6.3 Chi Cross Sections

6.3.1 Total Chi Cross Sections

The total inclusive cross section for the production of the individual chi state, j , in the forward hemisphere ($x_F > 0$) is given by the formula

$$\sigma_{\chi_j} = \frac{N_{\chi_j} \sigma_{\psi(x_F > 0)}}{\text{BR}_{\chi_j \rightarrow \psi \gamma} (A \cdot \epsilon)_\gamma N_\psi}, \quad (6.12)$$

where the number of chis in each state and the number of J/psis are given in tables 6.2 and 5.1, respectively. The acceptance times reconstruction efficiency for the chi decay photon from pion and proton induced reactions is found in section 6.1.1 while the branching ratios for the radiative decay of the J=1,2 chi states are $27.3 \pm 1.6 \%$ and $13.5 \pm 1.1 \%$, respectively [36]. The J/psi total inclusive cross sections are found in table 6.4 and come from previously published results [29, 15]. The cross sections per nucleon were determined assuming the atomic weight dependence for the J/psi cross section of $A^{0.92 \pm 0.008}$. The total inclusive cross sections of the individual chi states is presented in table 6.6

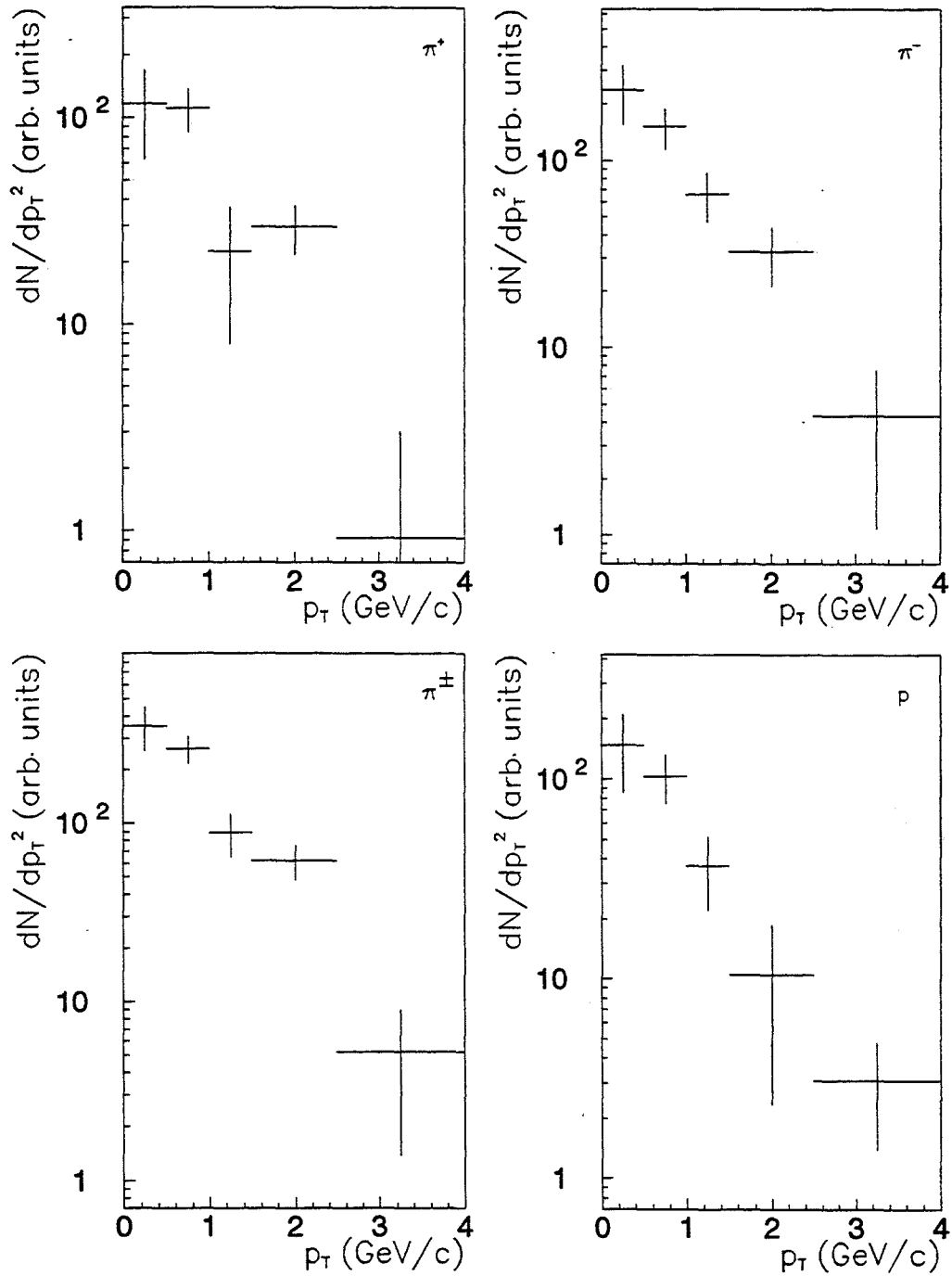


Figure 6.9: Raw chi transverse momentum distributions by beam type.

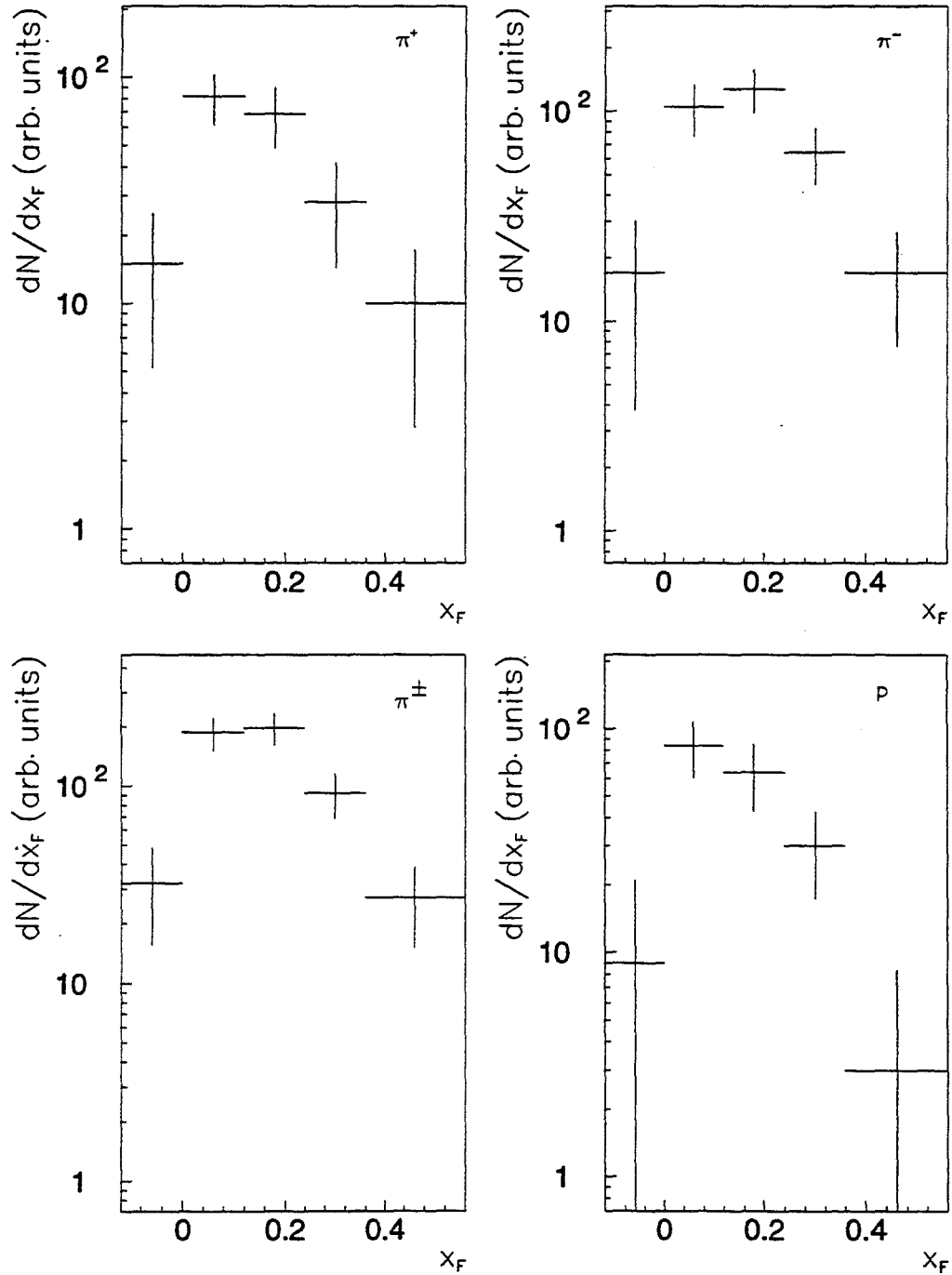


Figure 6.10: Raw chi Feynman x distributions by beam type.

Table 6.5: J/ψ total, forward, inclusive cross sections [29, 15].

Beam Type	$\sigma/\text{nucleus}$ (nb)	$\sigma/\text{nucleon}$ (nb)
π^+	$1060 \pm 90 \pm 57$	$179 \pm 15 \pm 10$
π^-	$1080 \pm 120 \pm 57$	$182 \pm 20 \pm 10$
proton	$850 \pm 90 \pm 42$	$143 \pm 15 \pm 7$

Table 6.6: χ forward, inclusive cross sections by beam type.

Cross section	π^+	π^-	π^\pm (comb.)	proton
σ_{χ_1} (nb/nucleon)	124^{+73}_{-72}	163^{+62}_{-64}	146^{+54}_{-56}	31^{+62}_{-61}
σ_{χ_2} (nb/nucleon)	329^{+150}_{-145}	189^{+117}_{-114}	277^{+116}_{-115}	364^{+124}_{-124}

6.3.2 Differential $\chi_1 + \chi_2$ Cross Sections

Differential cross sections, $d\sigma/dp_T$ and $d\sigma/dx_F$, were calculated for the combined $\chi_1 + \chi_2$ signal from each of the different beam types. The raw transverse momentum and Feynman x distributions for the χ signal were determined by subtracting the distributions found for events in the χ mass difference side bands ($0.066 < |M_{diff} - 0.44| < 0.132 \text{ GeV}/c^2$) from those produced from events in the χ signal mass difference signal region ($|M_{diff} - 0.44| < 0.066 \text{ GeV}/c^2$). The resulting transverse momentum and Feynman x distributions for the four beam types are found in figures 6.9 and 6.10, respectively.

The raw p_T and x_F distributions for each beam type were then corrected for acceptance and reconstruction efficiency of the J/ψ and the photon

Table 6.7: Fit parameters for chi p_T and x_f distributions

Beam Type	p_T fit parameters		x_F fit parameters		
	α (GeV/c) $^{-1}$	$\chi_{p_T}^2$	x_0	b	$\chi_{x_F}^2$
π^+	-1.41 ± 0.21	1.11	0.121 ± 0.079	9 ± 14	0.310
π^-	-1.39 ± 0.18	1.28	0.225 ± 0.089	7.2 ± 7.8	0.111
π^\pm	-1.39 ± 0.14	0.54	0.190 ± 0.069	7.7 ± 6.4	0.245
p	-1.47 ± 0.25	1.61	0.133 ± 0.054	18 ± 14	0.204

using the results of section 6.1.1. The corrected distributions were then fit to the empirical functions:

$$\frac{dN}{dp_T^2} = Ae^{\alpha p_T} \quad (6.13)$$

$$\frac{dN}{dx_F} = A \left(1 - (x_F - x_0)^2\right)^b. \quad (6.14)$$

where α , x_0 and b are the parameters determined by the fits; the results of which are tabulated in table 6.7. By fitting the corrected p_T and x_F distributions rather than the cross sections, we avoid errors introduced by the uncertainty in the cross section scale factor. The scale factor used to normalize the distributions were determined using the formula:

$$f = \frac{\sigma_{\chi_1+\chi_2}}{\int_0^1 \frac{dN}{dx_F} dx_F}, \quad (6.15)$$

where the cross sections $\sigma_{\chi_1+\chi_2}$ for each beam type are the sums of the individual cross sections for each chi state from table 6.6. Our total measured cross section (full acceptance) was determined by integrating the differential cross section, $d\sigma/dx_F$ over our entire acceptance ($-0.2 < x_F < 0.6$). The

Table 6.8: Angular distribution fit parameters by beam type.

Angular Distribution	Fit Parameter, a			
	π^+	π^-	π^\pm (comb.)	proton
$1 + a \cos \theta_\gamma$	1.2 ± 1.5	0.6 ± 1.4	0.9 ± 1.5	1.8 ± 2.1
$1 + a \cos \theta_{\mu^+}$	-0.92 ± 0.99	-0.60 ± 0.97	-0.78 ± 0.70	-2.30 ± 0.93

differential cross section in transverse momentum was calculated by normalizing the corrected p_T distribution to the total cross sections determined above. The resulting differential cross sections are presented in figures 6.11 and 6.12. The smooth curves on the plots are the results of the fits described above, renormalized to the correct scale.

6.3.3 Angular Distributions

Angular distributions of the chi photons and positive muon decay products were determined using the same sidband subtraction technique discussed in the previous section. The raw angular distributions are presented in figures 6.13 and 6.14. Corrections for acceptance and reconstruction efficiency of the photon and J/psi were applied using the results of section 6.1.1. The resulting distributions were fit to the functional form:

$$\frac{dN}{d \cos \theta} = (1 + a \cos^2 \theta) \quad (6.16)$$

Corrected angular distributions are shown in figures 6.15 and 6.16 with the results of the fits given in table 6.8.

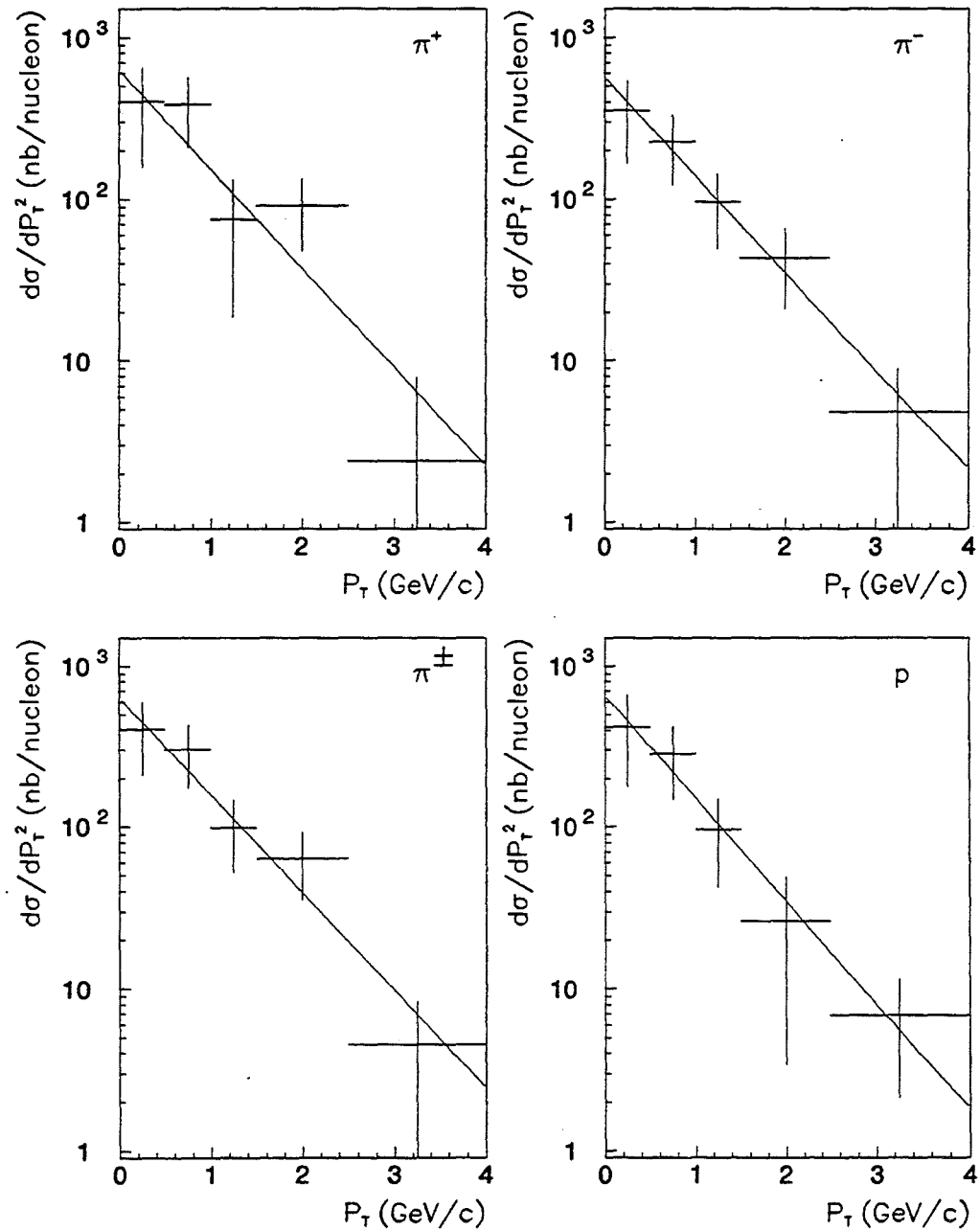


Figure 6.11: Combined chi differential cross section $d\sigma/dp_T$ by beam type.

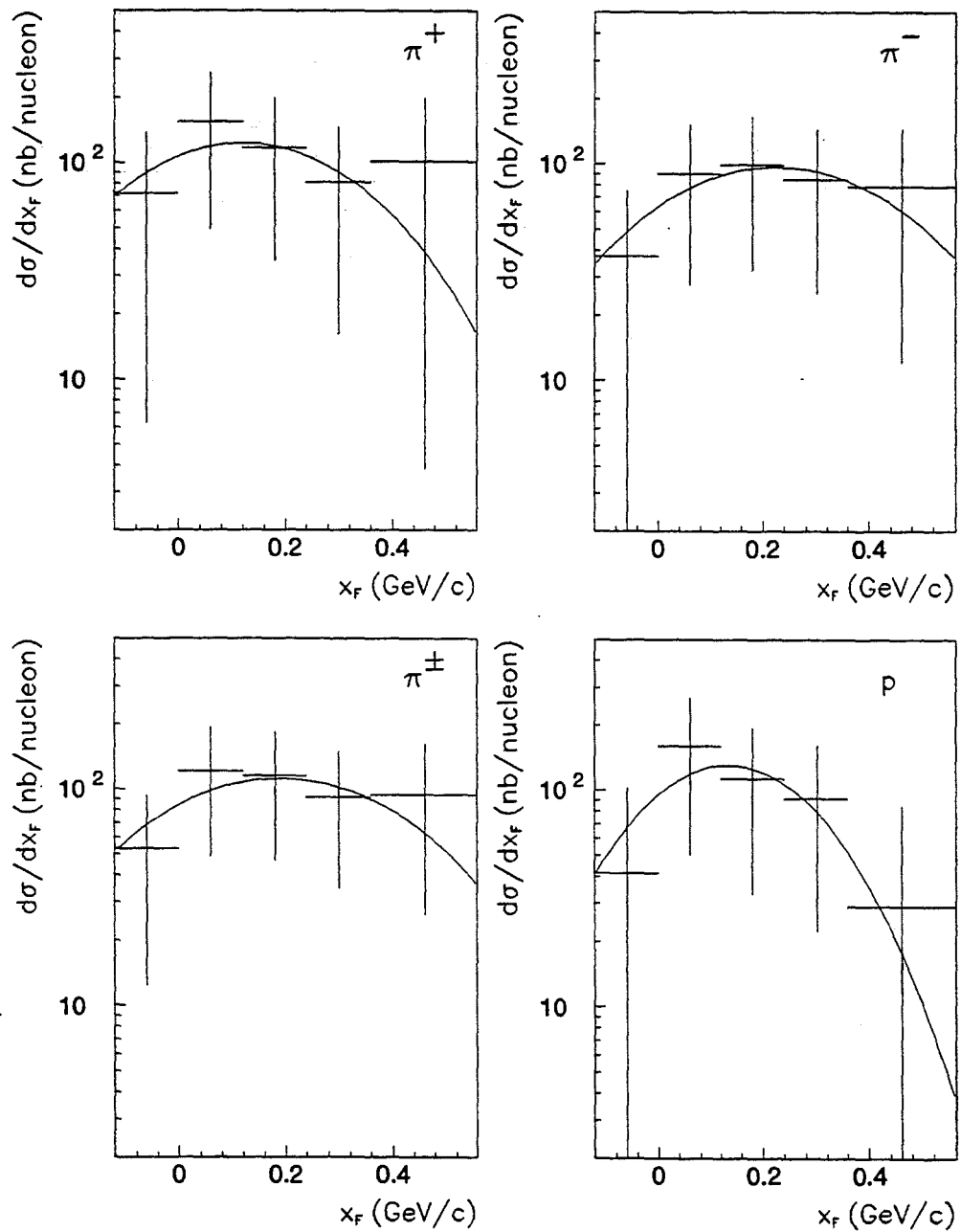


Figure 6.12: Combined chi differential cross section $d\sigma/dx_f$ by beam type.

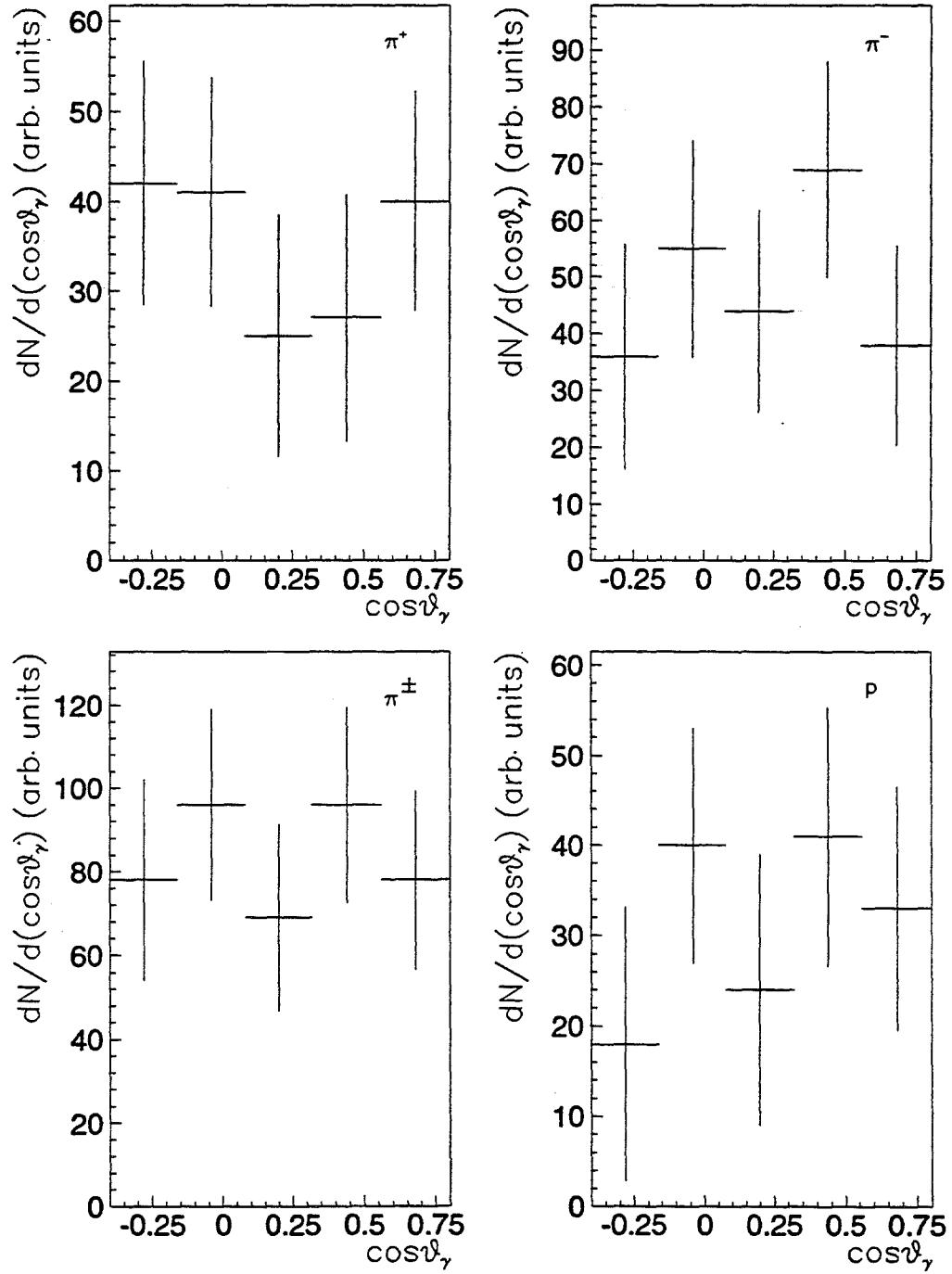


Figure 6.13: Raw chi photon angular distributions by beam type.

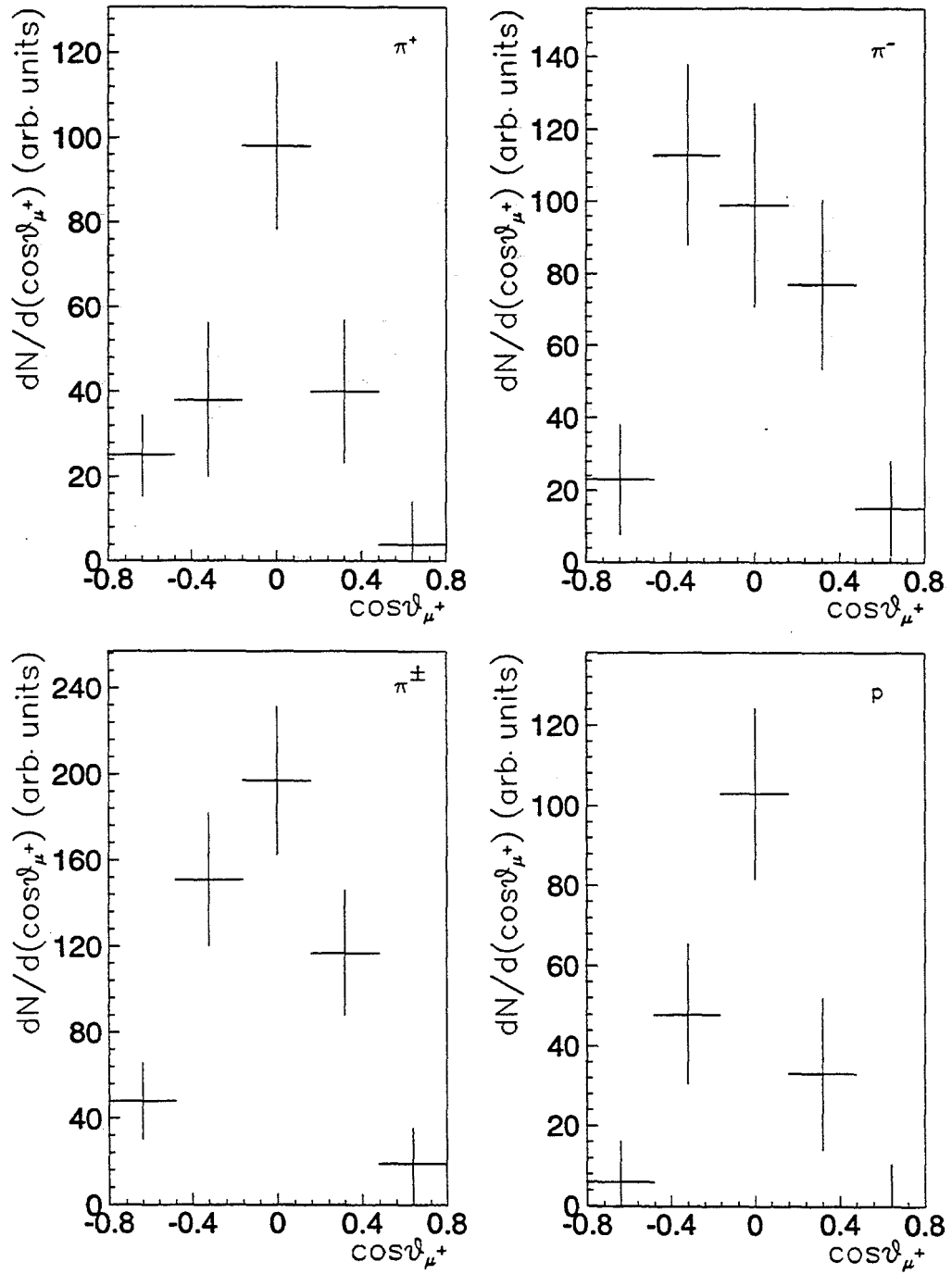


Figure 6.14: Raw chi positive muon angular distributions by beam type.

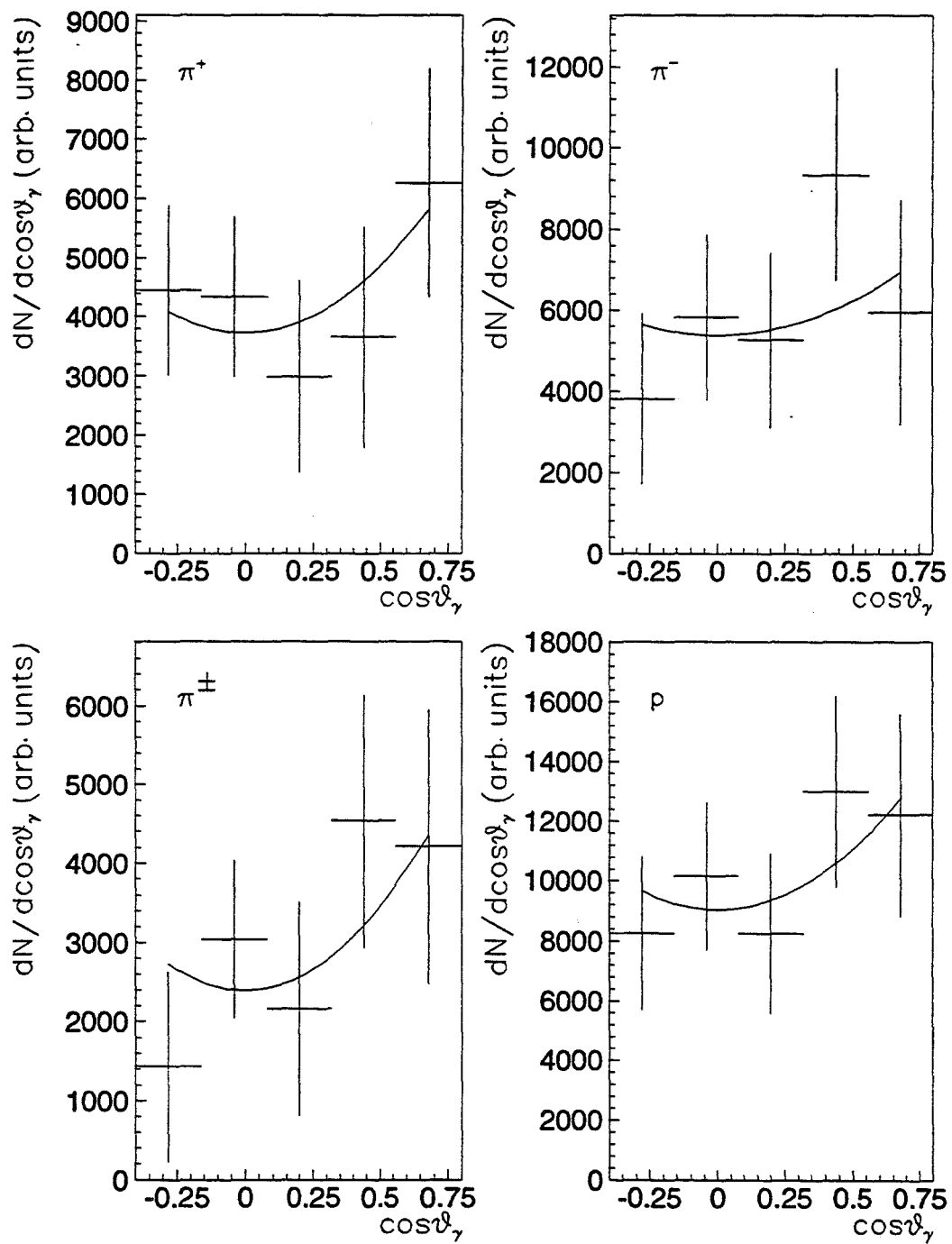


Figure 6.15: Corrected angular distributions for chi photons by beam type.

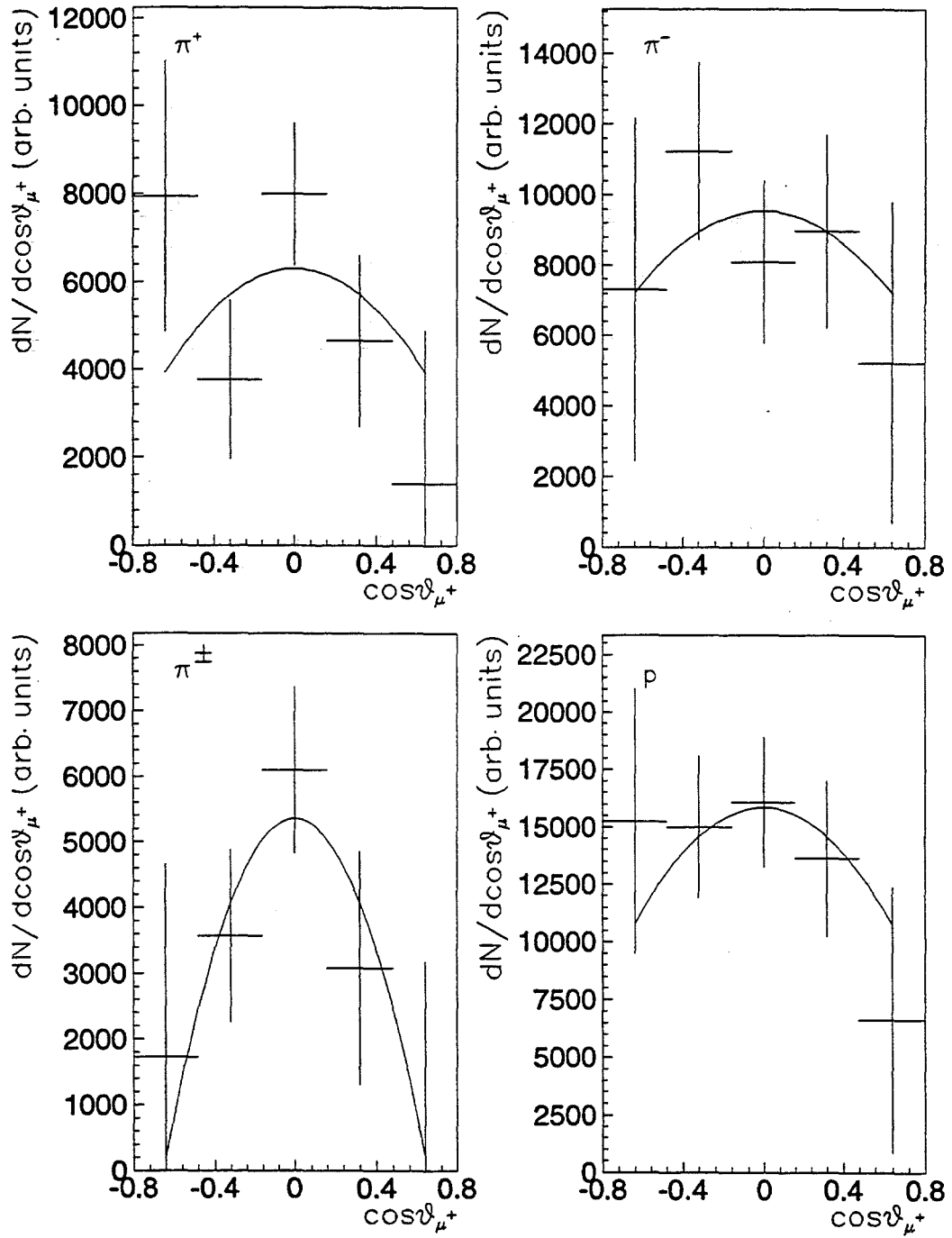


Figure 6.16: Corrected angular distributions for μ^+ from χ decay by beam type.

6.4 Summary and Conclusions

E705 chi production cross section ratios were determined for pion and proton beams on a lithium target to be $0.52^{+0.52}_{-0.28}$ and $0.08^{+0.25}_{-0.15}$, respectively. These ratios were compared with other experiments using beryllium targets and found to be consistent within the measurement uncertainties. Because of the nearly isoscalar nature of the targets the world average ratio of the chi production cross section ratios were also determined and give the values 0.73 ± 0.18 for pion induced reactions and 0.13 ± 0.14 for proton induced reactions. These values are consistent with the color evaporation model for chi production in pion-nucleon reactions and the two gluon fusion model for proton-nucleon reactions.

The separate $J=1,2$ chi production cross sections were determined to be 146^{+54}_{-56} nb/nucleon and 277^{+116}_{-115} nb/nucleon for pion induced reactions and 31^{+62}_{-61} nb/nucleon and 364^{+124}_{-124} nb/nucleon for proton induced reactions.

Differential cross sections in transverse momentum and Feynman x were determined for the combined $\chi_1 + \chi_2$ system. The p_T dependence of the differential cross sections were found to be similar for both our pion and proton data. The Feynman x dependence of the differential cross section for pions was found to peak forward and to fall off more slowly at large x_F than that for protons. This qualitative behavior agrees with observations from J/psi experiments [41] and is in accordance with gluon production mechanisms for the proton data.

Appendix A

Shower COMMON Block

```
*****  
**** SHOWER COMMON DOCUMENTATION ****  
*****
```

The arrays beginning with the letters KL and CL contain information that should change little during the analysis of an event, or, in the case of dynamic information, the best values known at the particular stage of the analysis. These arrays have the following definitions:

KLNUMB Number of clusters in this event.

The following information is accessed by cluster number. Clusters are ordered for diminishing peak block energy.

KLNBLS(ICL) Number of main array blocks in cluster ICL. Normally 9 or 11 blocks, where 11 blocks will have one virtual block (ICHAN>600) and two small blocks.

KLFIRST(ICL) Pointer into the M.A. block arrays for the first (peak) block in a cluster.

KLLAST(ICL) Pointer into the M.A. block arrays for the last block in a cluster.

KLSTAT(ICL) Main array cluster status.
 -2: Cluster eliminated, all block
 clblke()=0
 -1: Dimension of variables indexed by
 ICB, below, is too small, this
 cluster is incomplete.
 0: Everything OK. Isolated cluster.
 1: Everything OK. This cluster contains
 blocks shared with other clusters

KLFLAG1(ICL) Packed main array cluster flags:
 ILGC, IACE, IBCE, ICTRAK

KLFLAG2(ICL) Packed main array cluster flags:
 ISKFIT, IZFLG, NHS, IXYH

ILGLG matching energy found (0 - 1)
 IACE A matching energy found (0 - 1)
 IBCE B matching energy found (0 - 1)
 ICTRAK Matching charged track (0,1,3)
 0=no charged track present.
 1=matching charged track
 (deflected in Rosie).
 3=calibration track
 (straight ahead).

ISKPFIT (0 - 1) 0 forces a new fit to
 E and maybe X,Y on next call to
 SHARE. SHARE resets the flag to 1.

IZFLG packed index used to pick from Z
 shower tables in GLLXY/GLLE.
 Lower 4 bits=X, upper 4 bits=Y;
 each runs from 1 to 4 with the
 following meanings:
 1 for late(deep) showers,
 4 for early(shallow) showers

NHS number of matching hodoscope showers
 (0 - 9)

IXYH (0 - '68'X) nonzero indicates
 position is from hodoscope High order
 4-bits give X hodoscope plane
 (3,4,5,6) Low order 4-bits give Y
 hodoscope plane (1,2,7,8) GTH planes
 are 1-4)

These two arrayw are packed according to the prescription:

KLFLAG1()=(ILGC*256) +IACE)*256 +IBCE)*256 +ICTRAK

KLFLAG2()=((((ISKFIT*256) +IZFLG)*256 +NHS)*256 +IXYH

KLTYPE(ICL) Cluster type as set by various routines
 0=photon, 1=photon in pi mass combination,
 2=photon in eta mass combination,...
 11=electron, 12=muon, 13=unknown hadron,
 14=neutral hadron, 15=charged hadron,...
 100=split shower (see following pointers)

KLOFFSP(ICL) Index to first secondary cluster. If not
 zero this cluster has been replaced by
 two or more derived clusters.

KLPARNT(ICL) If this cluster is derived, this index points
 back up the chain. Zero for the last
 cluster in a chain.

KLEORDR(IORD) After a call to EORDER, KLEORDR(1) contains
 the cluster number of the most energetic
 main array cluster, (2) the next most, etc.
 KLFIND(ICL) Byte packed cluster finder information.
 This array is filled by a call to HDCLST and
 contains the following information.
 Byte 0 Peak and Over Threshold information.
 0 = No P.O.T. asserted.
 1 = P.O.T. asserted.
 Byte 1 Pt information:
 1 = Pt1
 3 = Pt2
 7 = Pt3
 15 = Pt4
 Byte 2 The position of the block that gave
 the hardware peak, standard CL block
 ordering (1-11).
 Byte 3 Presently unused.
 CLMAENG(ICL) Energy in the cluster's main array blocks
 CLMAERR(ICL) Fractional uncertainty in this energy.
 Actually this is EFRACT returned from GLE
 CLACHE(ICL) Estimate for energy deposit ahead of main
 array in active converter or hodoscope ACH.
 CLACHER(ICL) Fractional uncertainty in ACH energy
 CLACENG(ICL) Energy in the first active converter plane
 CLBCENG(ICL) Energy in the second active converter plane
 CLACERR(ICL) Fractional uncertainty in the Aenergy.
 CLBCERR(ICL) Fractional uncertainty in the Benergy.
 CLHOENG(ICL) Energy in the hodoscope (old and/or new)
 CLHOERR(ICL) Fractional uncertainty in this energy
 CLHOEX(ICL) Deconvoluted x hodo signal (E or lc for
 CLHOEY(ICL) Deconvoluted y hodo signal (LGoR GTH)
 CLETOT(ICL) Total shower (cluster) energy.
 CLETERR(ICL) Fractional uncertainty in the above energy.
 CLX(ICL) Estimate for the position of cluster
 CLY(ICL) initially the center of peak block
 CLZ(ICL) Best guess on peak Z of shower development
 0 is upstream face of converter plate
 CLXERR(ICL) X-uncertainty in this position
 CLYERR(ICL) Y-uncertainty
 CLTANX(ICL) DX/DZ for incident particle (photon or tk)
 CLTANY(ICL) DY/DZ for incident particle (photon or tk)
 CLTIME(ICL) determined time for a cluster.

.....
 This block list information is accessed by using the pointers,
 KLFIRST(ICL) and KLLAST(ICL):

KLCHAN(ICB) Channel numbers of the main array blocks
 in this cluster
 KLPOINT(ICB) Pointer into the main array block sharing
 array. KLPOINT(ICB)=0 when a block is not
 shared.
 KLCLUST(ICB) Index back to associated cluster (ICL)
 KLBSTAT(ICB) Block status. -N: Bad block
 0: Everything OK.
 +N: Various OK flags
 CLRELX(ICB) Position of block center relative to best
 CLRELY(ICB) estimate of cluster location.
 CLBLKE(ICB) Main array block energy assigned to this
 cluster.
 CLBEERR(ICB) Sharing contribution to squared
 fractional error in ma block energy.

.....
 The following list is accessed in the same manner as the above
 block but is for the active converter.

KLACN(ICL) Number of active converter blocks in
 cluster ICL.
 KLACF(ICL) Pointer into the active converter block
 arrays for the first block in this
 cluster.
 KLACL(ICL) Pointer into the active converter block
 arrays for the last block in this
 cluster.
 KLACST(ICL) Active converter flag.
 0: Everything OK.
 Isolated A.C. cluster.
 1: Everything OK. This
 A.C. cluster contains
 blocks shared with other
 clusters.

.....
 The information in this section is accessed by using the
 pointers KLACF, and KLACL.

KLACCHN(IACB) Channel numbers for the A.C. blocks in
 this cluster.
 KLACBST(IACB) Status of an individual A.C. block.
 -N: Bad block.
 0: Everything OK.
 +N: Various OK flags.

.....
 The following "energy sharing" array contains lists of block
 index numbers (ICB) that connect a single physical block to
 its various logical block occurrences in multiple clusters. The

array is divided into 10 word sections such that each physical block can be pointed back to 9 showers. Unused words in each section are zeroed. KLPOINT thus is incremented by ten between physical blocks.

KLSHAR(ISH) The KLPOINT index for a block points to the section in this array where the list of indices for that block occurs. The first number,
 KLSHAR(KLPOINT(ICB)),
 is the number of clusters sharing this block. The following numbers are the indices to the multiple occurrences of this block in the block array. So, to get the cluster indices for all the clusters to which a shared block contributes energy, one has:

```
example DO 1 I=KLPOINT()+1,KLPOINT()+KLSHAR(KLPOINT())
example ICL=KLCLUST(I)
example 1 CONTINUE
```

.....
 The arrays below, beginning with the letters KS, and CS contain information from a particular stage of the analysis.

KSSTAT(ICL) Bit packed status flag indicating whether or not information exists for a particular portion of the analysis. The bits have the following meanings:
 1: Empty (not to be used).
 2: Glass information.
 3: Hodoscope information.
 4: Tracking information.
 Bit number corresponds to the level number described below.

KSINDEX(ICL) The level index indicating which level the "best" information has come (see documentation below).

The following arrays are doubly indexed with the first index defined as above. The second index, LVL, indicates the level of the analysis for the particular information. LVL has the following meanings:

- 1: The best information available based on some criterion (chisquared/DOF information etc.).
- 2: Glass information.
- 3: Hodoscope information.
- 4: Tracking information.

Most of these arrays are equivalenced to the KL or CL arrays

defined above. For the following arrays see the appropriate KLxxxx or CLxxxx documentation above.

CSMAENG(ICL,LVL)	CSMAERR(ICL,LVL)
CSACHE(ICL,LVL)	CSACHER(ICL,LVL)
CSACENG(ICL,LVL)	CSBCENG(ICL,LVL)
CSABERR(ICL,LVL)	CSHOENG(ICL,LVL)
CSHOERR(ICL,LVL)	CSX(ICL,LVL)
CSETOT(ICL,LVL)	CSETERR(ICL,LVL)
CSY(ICL,LVL)	CSZ(ICL,LVL)
CSXERR(ICL,LVL)	CSYERR(ICL,LVL)
CSZERR(ICL,LVL)	CSCHISQ(ICL,LVL)

The array(s) below are not defined above.

CSCHISQ(ICL,LVL) The chisquared/DOF for this cluster, for this level of analysis.

Appendix B

Deconvolution Method

Both position and energy information was required to be extracted from the LGC and GTH. However, because of the statistical nature of electromagnetic showers, fluctuations in the statistics of each channel's sampling of an individual shower potentially introduced extra peaks into an energy versus position spectrum for these devices. To lessen the effect of these fluctuations a deconvolution method was used in conjunction with digital filtering techniques to extract both positions and energies from the hodoscopes spectra.

Consider a data signal spectrum that has the form of a sum of a known shape ($P(x)$) with different amplitudes (α_n) and locations within the spectrum (x_n):

$$F(x) = \sum_n \alpha_n P(x - x_n). \quad (\text{B.1})$$

If $\mathcal{F}(k)$ is the Fourier transform of $F(x)$ then one obtains

$$\begin{aligned} \mathcal{F}(k) &= \sum_n \alpha_n \int_{-\infty}^{\infty} P(x - x_n) e^{-ikx} dx \\ &= \sum_n \alpha_n e^{-ikx_n} \mathcal{P}(k), \end{aligned} \quad (\text{B.2})$$

where $\mathcal{P}(k)$ is the Fourier transform of the shape $P(x)$ and the complex phase comes from the application of the translation theorem for Fourier transforms.

Dividing equation B.2 by $\mathcal{P}(k)$, one gets:

$$\mathcal{A}(k) = \sum_i \alpha_n e^{-jkx_n}. \quad (\text{B.3})$$

Taking the inverse Fourier transform yields the spectrum:

$$\begin{aligned} \mathcal{A}(x) &= \frac{1}{2\pi} \sum_n \alpha_n \int_{-\infty}^{\infty} e^{ik(x-x_n)} dk \\ &= \sum_n \alpha_n \delta(x - x_n). \end{aligned} \quad (\text{B.4})$$

The deconvoluted spectrum, $\mathcal{A}(x)$, is now a series of delta functions in position where their respective amplitudes are the same as in the original spectrum.

Because of the noisy nature of the signal spectra in the LGC and particularly in the GTH views, a Gaussian filter was applied to the frequency spectrum $\mathcal{A}(k)$.

$$\mathcal{A}(k) = e^{-\frac{k^2}{2\sigma^2}} \sum_n \alpha_n e^{-ikx_n}. \quad (\text{B.5})$$

The advantage of using a Gaussian filter is that it keeps the high frequency components of the raw spectrum thus allowing but de-emphasizing nearby peaks. The effect of applying this filter with different width parameter, σ , can be seen in figure B.1. The sigmas used in the analysis were 0.5 and 0.8 cm^{-1} for the LGC x and y views and 4.0, 2.5, 3.0 cm^{-1} for the GTH x single, double and y views.

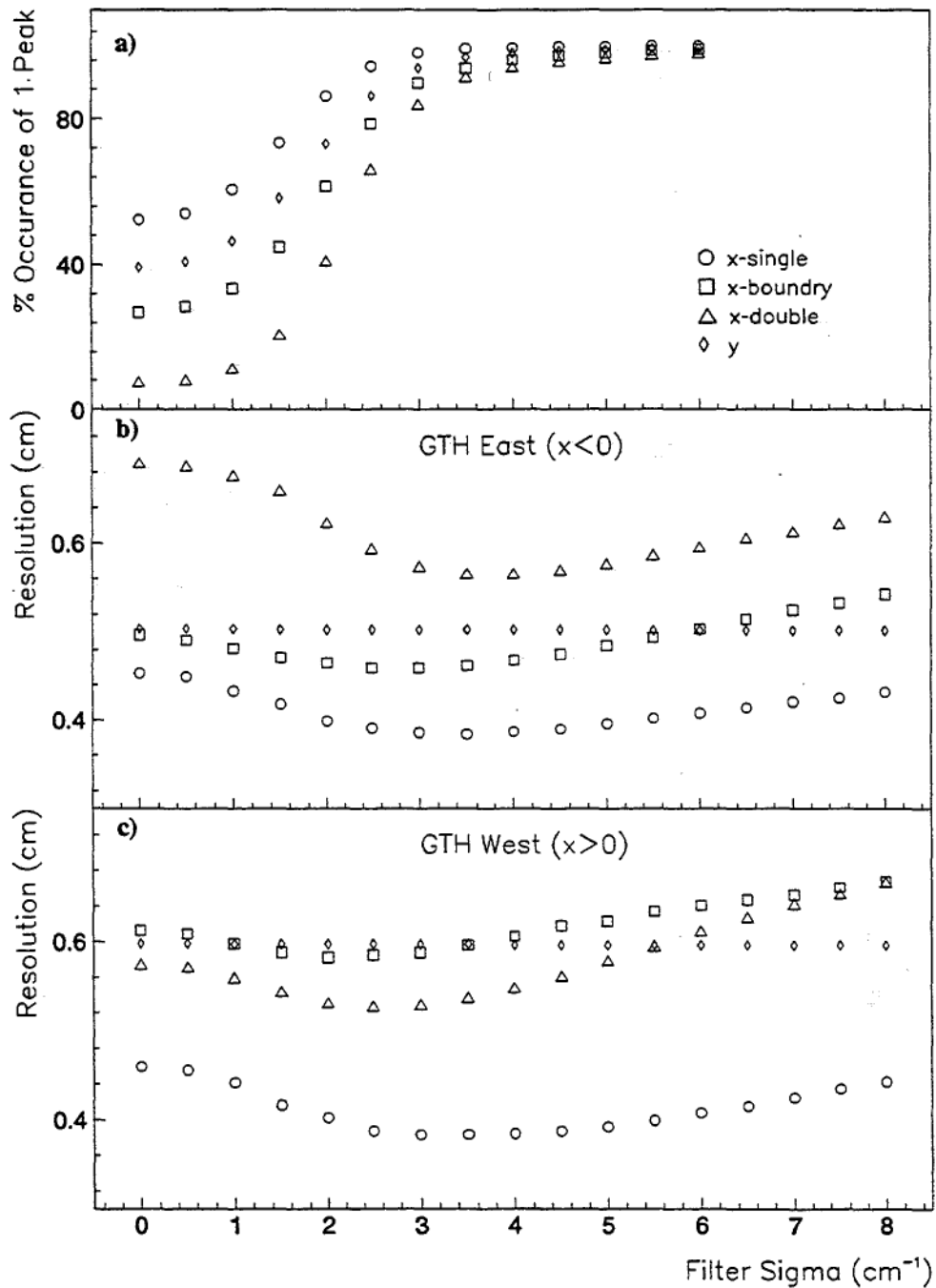


Figure B.1: Frequency filter effects for 30 GeV/c calibration electrons in the GTH; a) probability of reconstructing a single peak, b) resolution for the GTH-East planes and c) resolution for the GTH-West plane as a function of the Gaussian filter sigma.

Appendix C

Mass versus Mass Difference Uncertainties

In many high energy physics experiments one wishes to observe narrow resonance states that come from a cascade decay sequence where the detector resolutions determine the width of an observed mass peak. A prototype decay sequence may be:

$$\begin{aligned} a &\rightarrow b + c \\ &\hookrightarrow d + e, \end{aligned}$$

where c , d and e are observed particles with well established masses. For simplicity, only two body decays are considered. The best way to observe the resonance in a mass spectrum is to make it as narrow as possible. With this in mind one compares the mass uncertainties associated with the mass calculation with those associated with the mass difference calculation, $M_{diff} = M_a - M_b$. Recall the formula for the invariant mass for the two body decay in the laboratory frame.

$$M_a = \left\{ M_b^2 + M_c^2 + 2(E_b E_c - |\vec{P}_b| |\vec{P}_c| \cos \alpha) \right\}^{\frac{1}{2}} \quad (\text{C.1})$$

where M_b , M_c , E_b , E_c and $|\vec{P}_b|$, $|\vec{P}_c|$ are the masses, measured energies, and the measured momentum magnitude for particles b and c , respectively, with

$\cos \alpha$ the angle between \vec{P}_b and \vec{P}_c . In this analysis M_b is a derived quantity based on direct measurements of the b decay products and the uncertainty in the masses M_c , M_d , and M_e are negligible compared to the other the uncertainties discussed. For the purposes of this discussion, it is sufficient to consider just the b energy and momentum measurements* and the momentum measurement of c due to the relations:

$$M_b^2 = E_b^2 - |\vec{P}_b|^2, \quad (\text{C.2})$$

$$E_c^2 = M_c^2 + |\vec{P}_c|^2. \quad (\text{C.3})$$

From error propagation, assuming that all errors are independent, one gets

$$\delta M = \left\{ \left(\frac{\partial M}{\partial E_b} \delta E_b \right)^2 + \left(\frac{\partial M}{\partial |\vec{P}_b|} \delta |\vec{P}_b| \right)^2 + \left(\frac{\partial M}{\partial |\vec{P}_c|} \delta |\vec{P}_c| \right)^2 + \left(\frac{\partial M}{\partial (\cos \alpha)} \delta (\cos \alpha) \right)^2 \right\}^{\frac{1}{2}}, \quad (\text{C.4})$$

where M may stand for either M_a or M_{diff} . One knows from equations C.1, C.2 and C.3 that terms involving $|\vec{P}_c|$ and $\cos \alpha$ are the same whether either

 *In the decay scheme outlined, measurements are made of the decay products momenta. Therefore, one replaces the occurrences of E_b and $|\vec{P}_b|$ with:

$$\begin{aligned} \vec{P}_b &= \vec{P}_d + \vec{P}_e \\ E_b &= \left(M_d^2 + |\vec{P}_d|^2 \right)^{\frac{1}{2}} + \left(M_e^2 + |\vec{P}_e|^2 \right)^{\frac{1}{2}} \end{aligned}$$

which leads to the uncertainty relations:

$$\begin{aligned} (\delta |\vec{P}_b|)^2 &= \sum_{i=1}^3 (P_{d,i} + P_{e,i}) (\delta P_{d,i}^2 + \delta P_{e,i}^2) \\ \delta E_b^2 &= \frac{1}{E_d^2} \sum_{i=1}^3 (P_{d,i} \cdot \delta P_{d,i})^2 + \frac{1}{E_e^2} \sum_{i=1}^3 (P_{e,i} \cdot \delta P_{e,i})^2. \end{aligned}$$

In the equation above, E_d and E_e are given by relations similar to equation C.3.

M_a or M_{diff} replaces M in equation C.3, namely

$$\frac{\partial M}{\partial |\vec{P}_c|} = \frac{E_c}{M_a} \quad (C.5)$$

$$\frac{\partial M}{\partial \cos \alpha} = \frac{-1}{M_a} |\vec{P}_c| |\vec{P}_b|. \quad (C.6)$$

However, this is not true for the other terms which involve the measurement of b . For the mass calculation, M_a , these terms are

$$\frac{\partial M_a}{\partial E_b} = \frac{1}{M_a} (E_b + E_c) \quad (C.7)$$

$$\frac{\partial M_a}{\partial |\vec{P}_b|} = \frac{-1}{M_a} (|\vec{P}_b| + |\vec{P}_c| \cos \alpha), \quad (C.8)$$

whereas, for the mass difference one gets

$$\frac{\partial M_{diff}}{\partial E_b} = \frac{1}{M_a} \left[E_b \left(1 - \frac{M_a}{M_b} \right) + E_c \right] \quad (C.9)$$

$$\frac{\partial M_{diff}}{\partial |\vec{P}_b|} = \frac{-1}{M_a} \left[|\vec{P}_b| \left(1 - \frac{M_a}{M_b} \right) + |\vec{P}_c| \cos \alpha \right] \quad (C.10)$$

In equations C.9 and C.10 there is an extra factor multiplying the term involving the b particle measurement, namely $1 - \frac{M_a}{M_b}$. In the case where the decay particle, b , is a substantial fraction of the parent particle's mass, the expected uncertainty in the mass difference calculation is reduced compared with the mass calculation.

For the case of the radiative χ decays, the term $1 - \frac{M_{\psi\gamma}}{M_\psi}$ takes on the values -0.10, -0.13, -0.15 for the three χ states (χ_0, χ_1, χ_2), respectively.

References

- [1] Francis Halzen and Allan D. Martin, *Quarks and Leptons: An introductory Course in Modern Particle Physics*, New York, John Wiley and Sons, (1984).
- [2] Donald H. Perkins, *Introduction to High Energy Physics*, Menlo Park, California, Addison-Wesley, (1987).
- [3] L. Antoniazzi, *et al.*, "Production of J/ψ via ψ' and χ Decay in 300 GeV/c Proton- and π^\pm -Nucleon Interactions", *Physical Review Letters*, **70** (1993) 383.
- [4] R. Barbieri, R. Gatto, R. Kögerler, "Calculation of the Annihilation Rate of P wave Quark-Antiquark Bound States", *Physics Letters*, **60B** (1976) 183.
- [5] B. L. Ioffe "Mechanism of Charmonium Production in Hadronic Collisions", *Physical Review Letters*, **39** (1977) 1589.
- [6] J. H. Kuhn, J. Kaplan, E. B. O Safiani, "Electromagnetic Annihilation of $e^+ e^-$ into Quarkonium States of Even Charge Conjugation", *Nuclear Physics*, **B157** (1979) 125.
J. H. Kuhn, "Hadronic Production of P-Wave Charmonium States", *Physics Letters*, **89B** (1980) 385.
- [7] C. E. Carlson, R. Suaya "Comment on P-state Dominance in the Hadronic Production of Narrow Resonances," *Physical Review* **D15** (1977) 1416.
- [8] J. H. Cobb, *et al.*, "Study of Photons Produced Simultaneously with the J/ψ Particles at the CERN Intersecting Storage Rings," *Physics Letters* **72B** (1978) 497.
C. Kourkoumelis, *et al.*, "Study of χ Production at the CERN Intersecting Storage Rings," *Physics Letters* **81B** (1979) 405.
- [9] T. B. W. Kirk, *et al.*, "Production of Photons Associated with the ψ by 217-GeV/c π^- Mesons," *Physical Review Letters* **42** (1979) 619.

- [10] D. A. Bauer, *et al.*, "Differences between Proton and π^- -Induced Production of Charmonium χ States," *Physical Review Letters* **54** (1985) 754.
- [11] Y. Lemoigne, "Hadro-production d'états χ du Charmonium Aupres du SPS," Ph.D. Thesis, Centre d'Etudes Nucléaires de Saclay, Institut de Reserche Fondamentale, Département de Physique des Particules Élémentaires, June, 1988.
- [12] Y. Lemoigne, *et al.*, "Measurement of Hadronic Production of the $\chi_1^{++}(3507)$ and the $\chi_2^{++}(3553)$ Through Their Radiative Decay to J/ψ ," *Physics Letters* **113B** (1982) 509.
- [13] S. R. Hahn, *et al.*, "Hadronic Production of Charmonium in 225-GeV/c π^- Be Interactions," *Physical Review* **D30** (1984) 671.
- [14] F. Binon, *et al.*, " χ Particle Production in π^- p Collisions at 38 GeV/c," *Nuclear Physics* **B239** (1984) 311.
- [15] L. Antoniazzi, *et al.*, "Measurement of J/ψ and ψ' production in 300-GeV/c proton, antiproton, π^\pm interactions with nuclei," *Physical Review* **D46** (1992) 4828.
- [16] S. Conetti *et al.*, "Performance of 0.75 mm Pitch MWPCs Operating at High Rate", *IEEE Trans. on Nucl. Science*, **NS-36** (1989) 112.
- [17] L. Spiegel, *et al.*, "Performance of a Lead Radiator, Gas Tube Calorimeter", *IEEE Trans. on Nucl. Science*, **NS-36** (1989) 86.
- [18] S.W. Delchamps, *et al.*, "Precision Charge Amplification and digitization System for a Scintillating and Lead Glass Array", *IEEE Trans. on Nucl. Science*, **NS-36** (1989) 680.
- [19] B. Cox, *et al.*, "A Measurement of the Response of an SCG1-C Scintillation Glass Array to 4-14 GeV/c Pions", *Nucl. Instr. and Meth.*, **A238** (1985) 321.
- [20] D.E. Wagoner, *et al.*, "A Measurement of the Energy Resolution and Related Properties of an SCG1-C Scintillation Glass Shower Counter Array for 1-25 GeV Positrons", *Nucl. Instr. and Meth.*, **A238** (1985) 315.
- [21] L.R. Fortney, "An LED Source for Photomultiplier Gain Tracking". *Calorimeter Calibration Workshop*, 26-30 April 1983. Fermi National Accelerator Laboratory, Batavia, IL 1983.

- [22] T. Turkington, "Precise Measurement of Photons from the Interactions of 300 GeV/c Hadrons on a Lithium Target", Ph.D. Thesis, Duke University, 1989.
- [23] C.M. Jenkins, et al. , "Results from the E705 Electromagnetic Shower Position Detector", *IEEE Trans. on Nucl. Science*, NS-36 (1989) 117.
- [24] G. Zioulas, et al. , "An Online Trigger Processor for Large Transverse Energy Events", *IEEE Trans. on Nucl. Science*, NS-36 (1989) 117.
- [25] H. Areti, et al. , "A Fast Processor for Dilepton Triggers", *Nucl. Instr. and Meth.*, 212 (1983) 135.
- [26] M. Arenton. Electronic mail to author. 17 March 1992.
- [27] S. Conetti, et al. , "A Smart Crate Controller for Fast CAMAC Data Acquisition", *IEEE Trans. on Nucl. Science*, NS-32 (1985) 1326
- [28] M. Rosati "A Measurement of Proton and Pion Induced P-wave Charmonium Hadroproduction", Ph.D. Thesis, McGill University, 1992.
- [29] T. Lecompte "Production of J/ψ , ψ' and $\psi_2(3837)$ in 300 GeV Hadronic Interactions", Ph.D. Thesis, Northwestern University, 1992.
- [30] A. Simard "A Measurement of the Hadronic Production of J/ψ 's", MS Thesis, McGill University, 1989.
- [31] M. Arenton. Electronic mail to author. 14 February 1992.
- [32] Y. Tan "Study of Hadronic Production of Charmonium States in Open Geometry", PhD Thesis, Northwestern University, 1992.
- [33] Q. Shen, "High p_T π^0 and η Production by 300 GeV/c π^\pm and p Beams on a ${}^7\text{Li}$ Target", Ph.D. Thesis, Duke University, 1992.
- [34] Lloyd R. Fortney, *Principles of Electronics, Analog and Digital*. New York: Harcourt, Brace, Jovanovich, (1987).
- [35] T. Nash, et al., Fermilab-Conf-88/97 (1988).
T. Nash, et al., Fermilab-Conf-89/58 (1989).
- [36] Particle Data Group, "Review of Particle Properties." *Physical Review* 45D (1992).
- [37] W. T. Eadie, D. Drijard, F.E. James, M. Roos and B. Sadoulet, *Statistical Methods in Experimental Physics*. New York: North-Holland, (1988).
- [38] F. T. Solmitz, "Ann. Rev. of Nucl. Science." 14, 375 (1964).

- [39] Geoffrey T. Bodwin, Eric Braaten, G. Peter Lepage, "Rigorous QCD Predictions for Decays of P-Wave Quarkonia." *Physical Review D* **46** (1992) 1914.
- [40] F. James, M. Roos, *MINUIT Users Manual*, CERN Computer Centre Program, D506 (1989).
- [41] L. Lyons, "Massive Pair Production in Hadronic Interactions and the Quark Model," *Prog. Part. Nuclear Physics* (1981).

Biography

Richard James Tesarek [REDACTED]
[REDACTED]
[REDACTED]
[REDACTED]
[REDACTED]
[REDACTED]
[REDACTED]

[REDACTED] He attained his bachelor of arts from the University of Colorado in 1984 majoring in Physics and Mathematics with minors in Russian and History.

The Fall of 1985 saw Mr. Tesarek undergo a tremendous culture shock when he movee east to Durham, North Carolina where he entered the graduate school at Duke University. He worked as a teaching assistant at Duke for the 1985–86 school year and was subsequently awarded a research assistantship the summer of 1986. He was awarded a Masters of Arts from Duke in 1988 and completed his at Doctor of Philosophy at Duke in 1993.